Analysis of Ion and Neutral Behavior inside a Miniature Ion Thruster and Neutralizer with Respect to Inlet Configuration Utilizing Numerical Simulation

アリ, ユセフィアン

Analysis of Ion and Neutral Behavior inside a Miniature Ion Thruster and Neutralizer with Respect to Inlet Configuration Utilizing Numerical Simulation

Ali Yousefian

August 2020

Abstract

Our work focuses on the simulation of plasma particles within a miniature ion thruster and neutralizer specifically focusing on the ion and neutral behavior. Since the neutral density can easily be influenced and altered with simple changes made to the gas inlet configuration, we developed the hypothesis that altering the gas inlet configuration within a neutralizer and ion thruster would lead to significant changes to the natural density distribution and consequently possible changes to the ionization pattern, ion density and neutral recycle rate. With that in mind we aimed to develop an all-inclusive 3D FDTD-PIC simulation of plasma inside the discharge chamber including a Poisson solver where all particles (ions, electrons and neutrals) are treated as active particles. Our current work cannot simulate the plasma sheath due to incredibly fine mesh required which the limitations imposed by the current computational setups does not permit. However it offers a unique look into the behavior of ions and neutrals within the discharge and the neutral recycling phenomenon chamber which is often not well studied. With that limitation in mind we set to analyze the ion-neutral behavior for two candidate antennas (L shaped and Disk shaped) as well as four candidate inlet configurators. The simulation indicated the role the gas inlet plays in altering the ion and neutral behavior locally inside the discharge chamber by showing small but significant changes in the ion-neutral behavior and neural recycle rate. Furthermore, both horizontal inlets showed the potential for improvements in the ion density within the discharge chamber which needs to be further examined for both antenna shapes.

Our simulation showcases the potential of horizontal inlet configuration as an alternative inlet method however more research and experimental data is required. With that in mind further work will be underway in our research group to examine this possibility in the near future.

Contents

List of Figures

List of Tables

1

Introduction

Small satellites are an essential trend in space technology due to their lower production cost and better versatility. Table 1.1 indicates the satellite classification due to their mass and size. These small satellites have the advantage of versatility and in that regard they have been used for a variety of different missions such as small scale scientific missions, earth observation and remote sensing and education and training to name a few [1]. These satellites are limited by their mission duration due to a lack of on board propulsion system and as their popularity grows, so does the need for micro propulsion systems. Developing a propulsion system for small satellites is challenging due to their inherently small size and mass budget. This rules out chemical propulsion systems due to the volume of propellant needed to achieve mission objectives. The recent developments in electric propulsion has enabled to challenge chemical propulsion systems. This makes electric propulsion a feasible option due to its high specific impulse and long operation life time [2-4].

Table 1.1. Satellite Classification [1]

Class		Mass (Kg)	Cost (US $ Million)
Large		> 1000	> 181.72
Medium		500 – 1000	64.90 – 181.72
Small	Mini	100 – 500	12.98 – 38.94
	Micro	10 – 100	3.89 – 7.79
	Nano	1 – 10	0.39 – 1.95
	Pico	< 1	< 0.39

An ion thruster is an electric propulsion system which works by ionizing the neutral particles inside the discharge chamber through high energy collisions with electrons and accelerating the resultant positive ions outside the engine by using electrostatic fields which results in thrust (Figure 1.1 [5]). Therefore the inner workings of an ion thruster system can be categorized in three regions (Figure 1.2 [6]). In the ionization region, neutral particles are fed through the gas inlet into the discharge chamber where they can collide with microwave excited electrons and create ions. For a higher thrust efficiency, higher collision cross section and lower ionization energy is preferred. This is why Xenon is a popular option since it satisfies these criteria. Since the power consumed in the ionization phase does not contribute to the thrust force directly, we aim to keep the power consumption in this stage as low as possible to increase thrust efficiency.

In the acceleration region, these ions are accelerated outside of the engine utilizing an electrostatic field generated by the voltage difference between two grids which results in thrust. This thrust force can be calculated by:

$$F = J_b\sqrt{\frac{2m_iV_b}{q}} \qquad \text{eq. 1.1}$$

Where the mass of the ions is represented as m_i, the ion beam current flux is J_b and finally the voltage between the ion thrusters grids is represented by V_b. Consequently, the ion beam current flux is influenced by grid design as well as plasma properties inside the thruster. Therefore the ion beam current flux is calculated by:

$$J_i = qe^{-\frac{1}{2}}n_0\sqrt{\frac{kT_e}{m_i}} \qquad \text{eq. 1.2}$$

The plasma number density is represented by n_0 , the electron temperature is T_e, the Boltzmann constant is k and finally the ion beam current flux is J_i. On the other hand, the maximum current flux can be achieved as a result of the electric field generated by the two grids:

$$J_{max} = \frac{4}{9}\varepsilon_0\sqrt{\frac{2q}{m_i}}\ \frac{V^{\frac{3}{2}}}{L^2} \qquad \text{eq. 1.3}$$

The distance between the electrodes is indicated by L , and ε_0 is the vacuum permittivity. Therefore the grids will offer optimum ion beam current on a consistent basis. One major factor that limits this system is the constant sputtering of ions to the grids which limits the lifetime of the ion thruster.

Finally the ions neutralizer attached next to the ion thruster (away from the ion beam to avoid failure) generates electron in the same rate as the ions in order to prevent electric charge build up within the space craft. This is achieved through the voltage difference between the ion beam and the neutralizer called contact voltage. Since the thrust force is not dependent on the neutralizer, we hope to minimize fuel and power consumption.

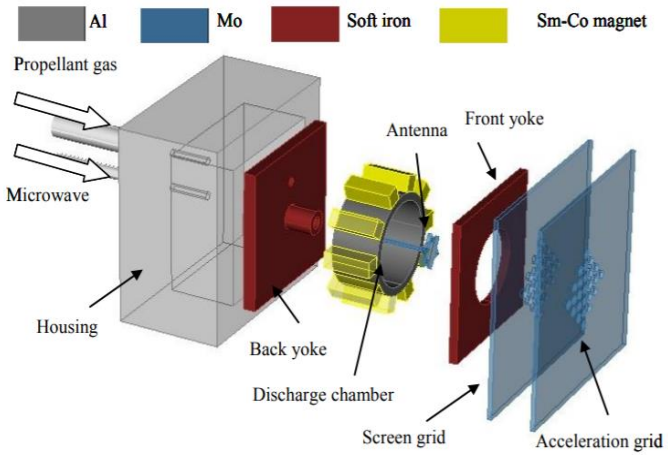

Figure. 1.1: An ion thruster developed in Yamamoto lab in Kyushu University

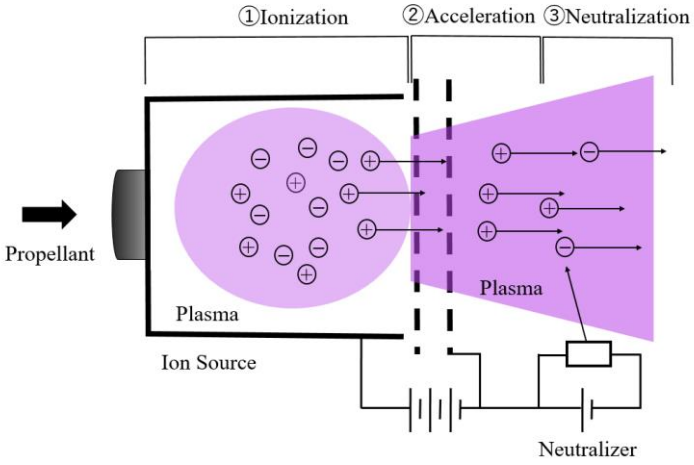

Figure. 1.2: Inner workings of an ion thruster system

Since electric propulsion systems operate at high exhaust velocities, they consume significantly less fuel that the conventional chemical rockets enabling them to save more weight and conduct long distance missions at a lower cost [7]. Although an ion thruster creates a very small quantity of thrust force, it achieves a very high specific impulse which makes it an ideal choice for outer space exploration. One such notable missions was the Hayabusa mission by JAXA with the purpose of collecting a sample from the asteroid Itokawa and returning such sample to earth (Figure 1.3). Hayabusa was groundbreaking for the fact that it was the first spacecraft to have a microwave discharge ion thruster utilizing electron cyclotron resonance (ECR) [8-9].

1.1 Research Purpose

Our current research involves the development of comprehensive numerical simulations for Miniature Ion Thrusters. Recently the interest in development of small sized spacecraft such as microsatellites has rapidly grown as more companies and universities invest in satellite technology. Since small satellites are developed faster as well as cheaper and due to their flexibility, they are a promising field in the near future and therefore they are the focus of many research groups [10-11]. A microsatellite is categorized as a light weight spacecraft (less than 50 Kg) which due to the relatively low cost and short development time, it is an increasingly popular option since they can be launched piggybacked on already existing payloads.

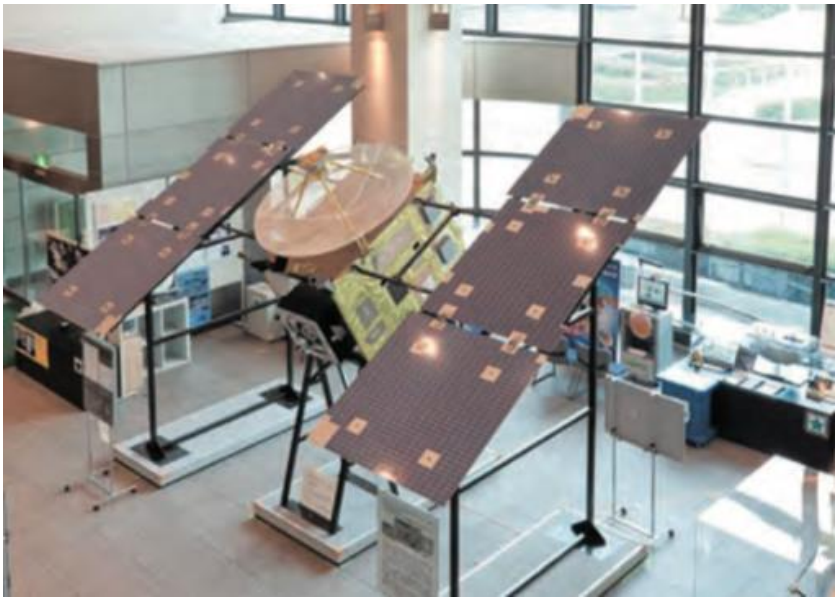

Figure 1.3: Four Ion thrusters on Hayabusa in JAXA Sagamihara Campus

These satellites are already widely used for different applications such as communication and earth observation. An ion thruster can achieve a unique thrust efficiency of 70% along with a specific impulse within the range of 3000-8000 s.As a result, miniature ion engines are an excellent option as a propulsion source for small satellites [12]. The satellites mission aspects is expected to greatly improve with the implementation of a miniature electric propulsion system. Meaning that more challenging missions such as mars exploration as well as self-disposal can be achieved [13]. These devices offer aspects such as attitude control, orbit transfer as well as station keeping. This makes miniature propulsion systems for microsatellites a common practice in the near future [14]. Figure 1.4 indicates one such miniature ion thruster developed in our research group. Unfortunately however, the performance of these small thrusters has been less than ideal in contrast to their conventional sized models mainly due to their higher ion production cost often attributed to their poor plasma microwave coupling. They also suffer from higher rate of ion and electron loss to the walls. Miniature thrusters have a lower trust efficiency of at most 50% in comparison to the average 70% of normal ion engines. Moreover miniature thrusters have a higher ion production cost of 400eV on average in contrast to 100eV for normal thrusters [15]. Other factors that impact thrust performance include the configuration of antenna and magnetic field as well as the thruster structure [13]. Because of the limited size of the micro thrusters, measurement of plasma characteristics inside the discharge chamber poses a challenge and therefore numerical simulations are an effective tool for understanding the inner workings of a miniature microwave ion thruster [16]. Without simulation the only way to optimize the utility of a miniature thruster is by trial and error which is costly and ineffective. As a result by developing a code that incorporates both the Particle In Cell (PIC) method as well as the Finite Difference Time Domain (FDTD) ,would offer the best of both worlds since the PIC code works best at treating the collisions

and particle distribution while the FDTD code can deal with the electromagnetic wave propagation through the plasma [17]. Since electron density distribution plays a critical role in engine's thrust outcome, the research in this area is mainly focused on improving microwave plasma coupling and electron density distribution [17-24].

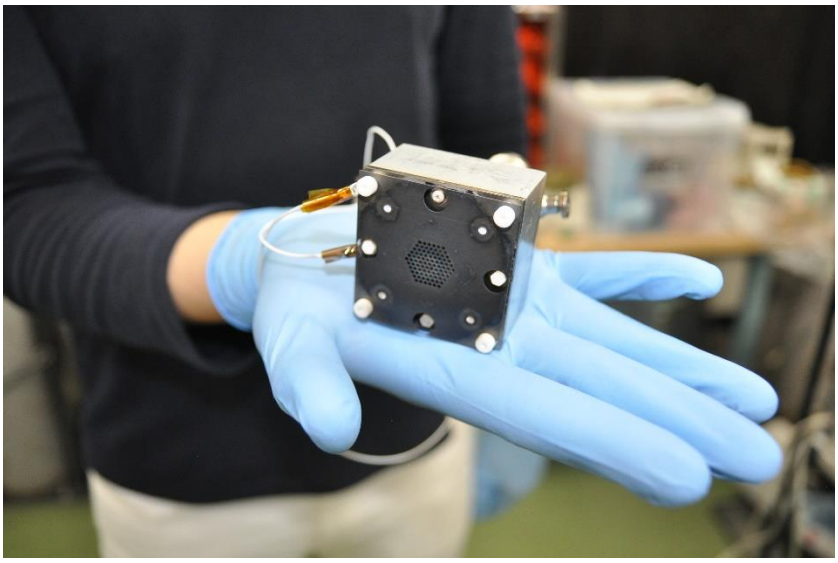

Figure 1.4: Miniature Ion Thruster Developed in Yamamoto Lab. Kyushu University

Therefor the impact of neutral density on ion generation and ion loss to the walls (neutral recycle effect) is not well studied. Although the changes in the neutral density caused by ion loss to the walls are small, they are significant and offer an opportunity for optimization. Therefore, improving the ion production and loss to the walls would lead to an improvement in miniature ion thruster and neutralizer`s performance. While previous works have studied the impact of ion loss on engine's performance [25-28], the effect of neutral density on thruster's performance has not been well established. This is mainly due to the fact that electron density distribution plays a stronger role in determining the engine's performance. However, since neutral density distribution is often an overlooked aspect in simulations, we aimed to investigate the impact engine configuration has on neutral density distribution and consequently ion loss to the walls and engine performance as a whole. Our current work will focus on investigating the specific impact of gas inlet configuration on neutral density within the ion thruster and neutralizer as well as analyzing the resultant impact on neutral recycle rate to the walls and engine performance by utilizing simulation techniques.

In the following sections we will describe the simulation techniques used as well the background and motivation for each simulation followed by the simulation results and their significance.

2

Simulation of Neutral Particles in a Neutralizer with Respect to Inlet Configuration

In this section, we will investigate the impact gas inlet has on neutral density distribution as an initial step in proving our hypothesis that the gas inlet has the potential to impact not only the neutral density distribution, but also the ionization rate and ion-neutral behavior as well. We have developed an original 3D PIC code to simulate the behavior of neutrals inside a neutralizer that enables us to analyze their density distribution throughout the engine [29]. In our simulation, the behavior of the neutral particles such as their interaction with the engine walls and collisions is simulated and the PIC method is utilized for the density calculation. By analyzing the inlet position and configuration we can determine the neutral density distribution throughout the engine and examine its effectiveness. Research in the simulation of neutrals inside electric propulsion systems have been very limited. Neutrals are often treated as background particles with their interactions being ignored even in the previous works done in our research group [30-31]. Other works in this area include Mahalingam and Menart [32] whose work considers a uniform neutral gas density while it focuses on ions and electrons as active particles. As a result, their work has focused on investigating electron behavior with respect to magnetic field changes [33] as well as simulating the electric field inside an ion thrusters discharge chamber [34]. On the other hand Stueber [35-36] utilized a three dimensional particle based model for mapping neutrals which will utilize a three dimensional fluid electron code alongside it. Boeuf and Garrigues [37] conducted a one dimensional study focusing on hall thrusters in which they utilized the kinetic Vlasov equation to simulate ions while neutrals were simulated with a constant velocity and the continuity equation. This model however ignored the wall impact and particle interactions with it. On the other hand, other works focusing on neutral behavior includes Birdsall [38] who focuses on Collison behavior of neutrals utilizing a PIC code while Boyd [39] simulated neutral xenon flow in three different electric propulsion systems. To our knowledge there is no work focusing on the impact of gas inlet on neutral density distribution within electric propulsion systems. The gas inlet has the potential to alter the neutral density distribution within the system and offer an opportunity for improvement. Moreover different antenna shapes yields different ionization regions. This means a distinct inlet configuration is needed for specific antenna shapes. Generally, for an L shaped antenna we hope for a higher density of neutrals around the L part of the antenna while for the star or disk shaped

antenna, a uniform distribution around the antenna is preferred. With that in mind we developed a PIC simulation neutral particles inside a neutralizer with respect to changing inlet configurations. While this code utilizes the PIC method, it only simulates the behavior of neutrals alone. The following chapters will discuss the behavior of ions and electrons utilizing the PIC method as well.

2.1 Particle In Cell Method

PIC method divides the special regions in the simulation to grid points where simulation properties of the cell are stored. One of these properties include particle densities which utilizing this special division allows for the calculation of collision probability with respect to the local density information. This will enable a comprehensive simulation of particles inside a wide range of systems. PIC method is widely used in plasma simulation for due to its ability to adapt to parallelization methods [29-39] and its capability to simulate key aspects from simulation of ion-neutral behaviors in plasma reactors [40-43], binary collision models [44-46], space plasma simulation [47] and etc.

2.1.1 Simulation Properties

In this simulation, neutrals are inputted in the gas inlet using their maxvellian velocity distribution. this velocity distribution is calculated by

$$V_{mp} = \sqrt{2R_m T} \qquad \text{eq. 2.1}$$

Where V_{mp} is their most probable speed , R_m is the gas constant and T is the ambient temperature of 297 K. based on these parameters, the particles achieve a most probable speed of approximately 194 m/s . in the simulation setting however, the maxvellian velocity distribution is applied as follows:

$$C = V_{mp}\sqrt{-\log(r)} \qquad \text{eq. 2.2}$$

Where r is a randomly generated number between 0 and 1 .

Utilizing two randomly generated angles of θ and φ between 0 to 360, Each particle velocity is defined as follows:

$$v_x = C.cos\theta.cos\varphi \qquad \text{eq. 2.3}$$

$$v_y = C.sin\theta.cos\varphi \qquad \text{eq. 2.4}$$

$$v_z = C.sin\varphi \qquad \text{eq. 2.5}$$

These are the equation of motion for the neutral particles within the system. The simulation region is divided into computational regions with the size of:

$$V_{cell} = \Delta x \times \Delta y \times \Delta z \qquad \text{eq. 2.6}$$

Finally, since the computational cost of simulating every real particle is astronomical, large groups of real particles are represented by one simulation particle. This simulation particle is called a super particle and it is assumed to be a stand it for the real number of particles it replaces in the simulation code. As a result, if the super particle number for a PIC simulation is set to 1.5×10^9 , this means that each simulation particle represents 1.5 billion real particles and the calculation cost would be realistic.

In order to achieve a comparative study of neutral particle distribution with respect to different inlet position, we have considered 4 different Inlet layouts to simulate which are as follows:

- **Bottom inlet:** currently used inlet position located right below the L shape of the antenna in the shape of a 2 mm square with a depth of 10 mm
- **16 small inlets:** consists of 16 small inlets distributed evenly at the bottom of the discharge chamber each in the shape of a 0.5 mm square with 10 mm depth
- **4 horizontal inlets:** consists of 4 horizontal inlets at antenna height each in the shape of a 1 mm square with 10 mm depth
- **1 horizontal inlet:** consists of 1 horizontal inlet facing the L shape of the antenna in the shape of a 2 mm square with 10 mm depth

Table 2.1. PIC simulation properties for all 4 inlet positions

Simulation real time (ms)	40
Simulation grid sizes (mm)	0.5
Time step (s)	5×10^{-8}
Super Particle Number	0.5×10^{9}
Mass Flow Rate ($mg.s^{-1}$)	4.9×10^{-2}

The rest of the simulation properties are identical for all the inlet cases as indicated in table 2.1. As it can be seen in table 2.1, in order to achieve a more accurate and realistic simulation we have considered a very low super particle number which will greatly influence the calculation time. To deal with that we adapted a hybrid OpenMP-MPI parallelization method for all the simulation cases. The simulation runs for a real time of 40 ms which is enough for the system to reach a steady state in which the flux of incoming particles form the inlet is similar to the flux of particles leaving the engine.

2.1.2 Simulation of Particle Collisions

In order to calculate the collision probability of a neutral particle within a defined system, first we need to define a variable called the mean free path. Considering a particles movement, the average distance a particle progresses until a Collison occurs is defined by the mean free path:

$$\ell = (\sigma n)^{-1} \quad \text{eq. 2.7}$$

Where σ is the collision cross section and n is the particle density. With this in mind, the collision frequency can be calculated as the ratio of a particles velocity over its mean free path:

$$\upsilon = \frac{v}{\ell} = \sigma n v \quad \text{eq. 2.8}$$

Finally the probability of collision for this particle is calculated by :

$$\mathrm{p_{collision}} = 1 - e^{(-\upsilon \Delta t)} = 1 - e^{(-\sigma n v \Delta t)} \quad \text{eq. 2.9}$$

In the simulation setting, a collision occurs when the r (a random number generated between 0 and 1) is smaller than the collision probability.

Neutral-Neutral collision as well as Ion-Neutral collisions (in the following sections) follow a similar method as elastic collision. The particles initial velocity is given following maxwellian distribution and its energy is calculated from its velocity. The collision cross section for these particle types however is calculated from the simple formula below:

$$\sigma_{neutral} = 2\pi d_{xe}^2 \quad \text{eq. 2.10}$$

Where d_{xe} is the diameter of the Xenon atom. This cross section is obtained by considering a sphere where two xenon particles collide achieving a cross section which looks like a circle with the radius of d_{xe} . in our simulation, the particles will receive a new random velocity and direction in a similar fashion as described in section 2.1.1.

2.1.3 Wall Reflections

When a neutral particle is coming in contact with the simulation walls, it is scattered away in a random manner from the wall by receiving a new velocity as described in section 2.1.1 .

2.1.4 PIC Mesh Interpolation

Since the simulation space in PIC method is divided into meshes, the electromagnetic field values as well as particle and current densities are saved at the grid points as a representative of the entire grid. Therefore it is crucial to transfer the charges of each particle to the lattice points as well as calculate the electromagnetic fields for each mesh. Furthermore the impact of the calculated electromagnetic fields on each particles within the cell should also be interpolated. For the purposed mentioned, PIC method is utilized. Figure 2.1 indicates a hypothetical particle in a grid labeled with its lattice points such as (i,j,k). The particle divides the cell into 8 regions labeled as $V_1 - V_8$. In order to interpolate the impact of field values at lattice points on the particle, the weight of each grid point with respect to its distance to the particle (A_n) is calculated as follows:

$$A_n = \frac{V_n}{V} \quad (n = 1 \sim 8) \qquad \text{eq. 2.11}$$

Therefor the impact of the electric field as an example on this particle is interpolated with:

$$E_{particle} = A_1.E_{(i,j,k)} + A_2.E_{(i+1,j,k)} + A_3.E_{(i+1,j,k+1)} + A_4.E_{(i,j,k+1)} + A_5.E_{(i,j+1,k)} + A_6.E_{(i+1,j+1,k)} + A_7.E_{(i+1,j+1,k+1)} + A_8.E_{(i,j+1,k+1)}$$

eq. 2.12

The density inside each cell is also calculated utilizing the PIC method and its interpolation is as follows. Considering the particle in Figure 2.1, the charge current density for the cell assuming a single super particle is calculated as follows:

$$\rho = \frac{sp}{V_{cell}} \qquad \text{eq. 2.13}$$

$$\rho_{(i,j,k)} = \frac{V_1}{V^2} \frac{sp}{V_{cell}} \qquad \text{eq. 2.14}$$

2.2 Simulation Geometry

For a comparative study we chose one of the miniature neutralizers Developed in Yamamoto research group in Kyushu University (depicted in Figure 2.2) as the sample engine and adjusted the simulation to it. The inner geometry of the simulation regions in depicted in Figure 2.3.

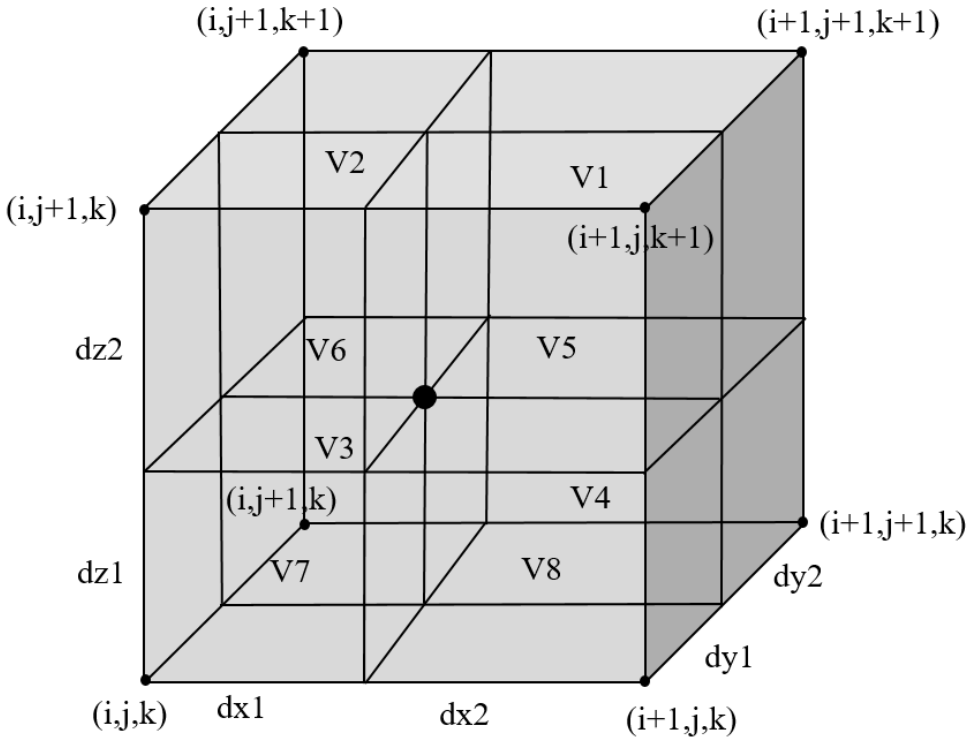

Figure 2.1: Construction of a cell in PIC method

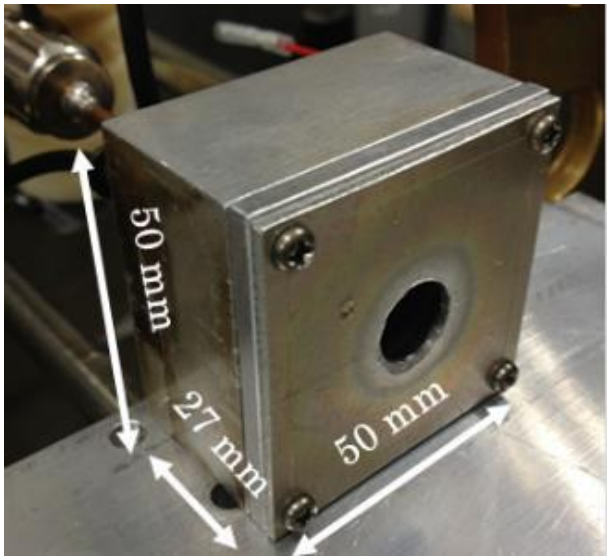

Figure. 2.2: A Neutralizer developed sf in Yamamoto lab in Kyushu University

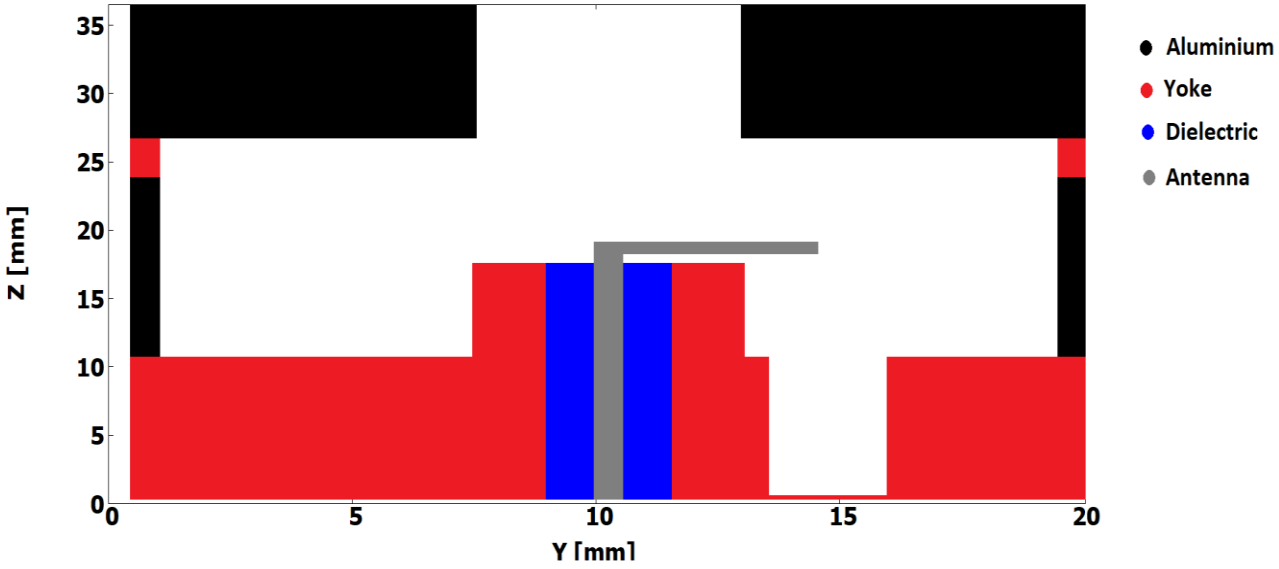

Figure. 2.3: Y-Z cross section of the neutralizer thruster taken at X = 10 mm (middle of the simulation geometry) for the conventional bottom inlet

2.3 Validation

In order to validate the results of the simulations, we have calculated the average density of neutrals in the discharge chamber and compared it with the theoretical density expected using the vacuum conductance theory as follows [48]:

$$\boldsymbol{Q = C\,(P_1 - P_0)} \qquad \text{eq. 2.15}$$

Where P_0 is the gas pressure at the orifice exit and P_1 is the gas pressure at discharge chamber. Q and C are the conductivity and the conductance constant respectively calculated from:

$$\boldsymbol{Q = \dot{m} \times 1.68875 \times 10^{-3}\, Pa.m^3.s^{-1}} \qquad \text{eq. 2.16}$$

$$\boldsymbol{C = C_1.k_2} \qquad \text{eq. 2.17}$$

Where $C_1 = \sqrt{\frac{RT}{2\pi M}} A$, $\dot{m}$ is the gas inlet mass flow rate , A is the area of the orifice and k_2 is a constant dependent on the ratio of the orifice length to its diameter. In our simulation this ratio is set to 2 since the diameter of the orifice is 5 mm and the length of simulated orifice area is 10 mm which leads to $k_2 = 0.359$. And finally the average particle density is calculated by the equation of the perfect gas:

$$\boldsymbol{n_1 = \frac{P_1 avg}{RT}} \qquad \text{eq. 2.18}$$

Therefore the calculated average density for the neutral particles in our engine is 5.325×10^{20} m^{-3}. The average particle density of all the simulation cases where within the acceptable range of the theoretical value and therefore the validity of the simulation is confirmed. Finally the flowchart of this simulation is indicated in Figure 2.4.

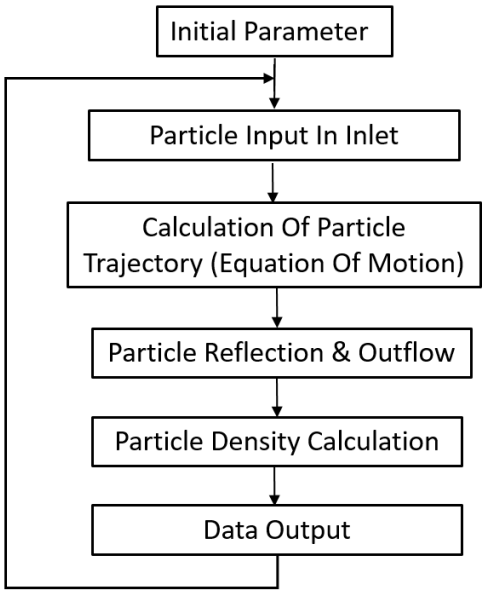

Figure. 2.4: Flowchart of the Neutral only PIC code

2.4 Simulation Results

The simulation results of all the inlet positions are illustrated in Figures 2.5 through 2.8 where the top frame is a vertical cross section of the engine drawn from the middle of the engines X axis and the bottom figure is a horizontal cross section at the antenna's top L shape. As mentioned earlier, the desired density around the antenna relies on the antenna shape. For an L shaped antenna we would hope for a higher density of neutrals around the L part of the antenna while for other symmetric antenna shapes such as star shape or disk shape, we prefer a more uniform distribution. Figure 2.5 indicates the density distribution for the one inlet located at the bottom of the antenna. It can be seen that there is a higher concentration of neutrals around the L part of the antenna where the opposite side lacks this higher density. This inlet configuration is suitable for the L shaped antenna however it would not be the best option for other symmetric antenna shapes. Figure 2.6 illustrated the density distribution when 16 small inlets are places at the bottom of the engine. As expected, this configuration leads to a uniform distribution of neutrals throughout the engine. Since this uniform distribution is desired for the disk shaped antenna or other symmetrical antenna shapes, we would not recommend this inlet configuration for the L shaped antenna. Figure 2.7 indicates the density distribution for the four horizontal inlets symmetrically placed around the engine facing the antenna. It is evident from the figures that density distribution is quite similar to the 16 bottom inlets in which we see a more uniform distribution around both sides of the antenna. This also means that this design is not optimal for an L shaped antenna however it would be an attractive option for symmetrical antenna shapes. Furthermore Figure 2.8 shows the density distribution for a single horizontal inlet facing the L part of the antenna. As expected this does lead to a higher density concentration around the L part of the antenna since opposite side of the antenna clearly lacks the same concentration. This means a horizontal inlet directly placed facing the L part of the antenna should be a better option.

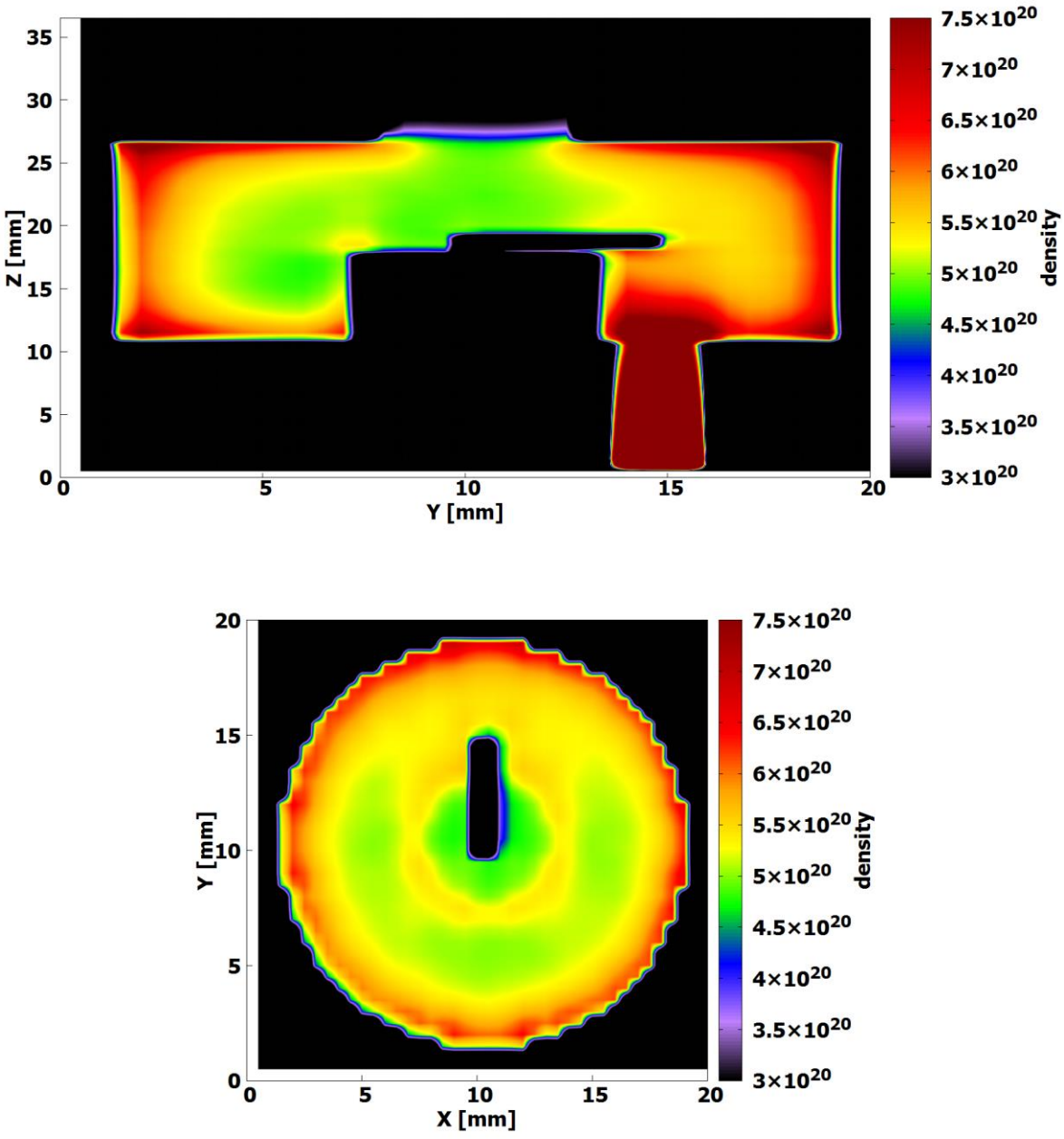

Figure. 2.5: Density Distribution of Neutrals for the Bottom Inlet

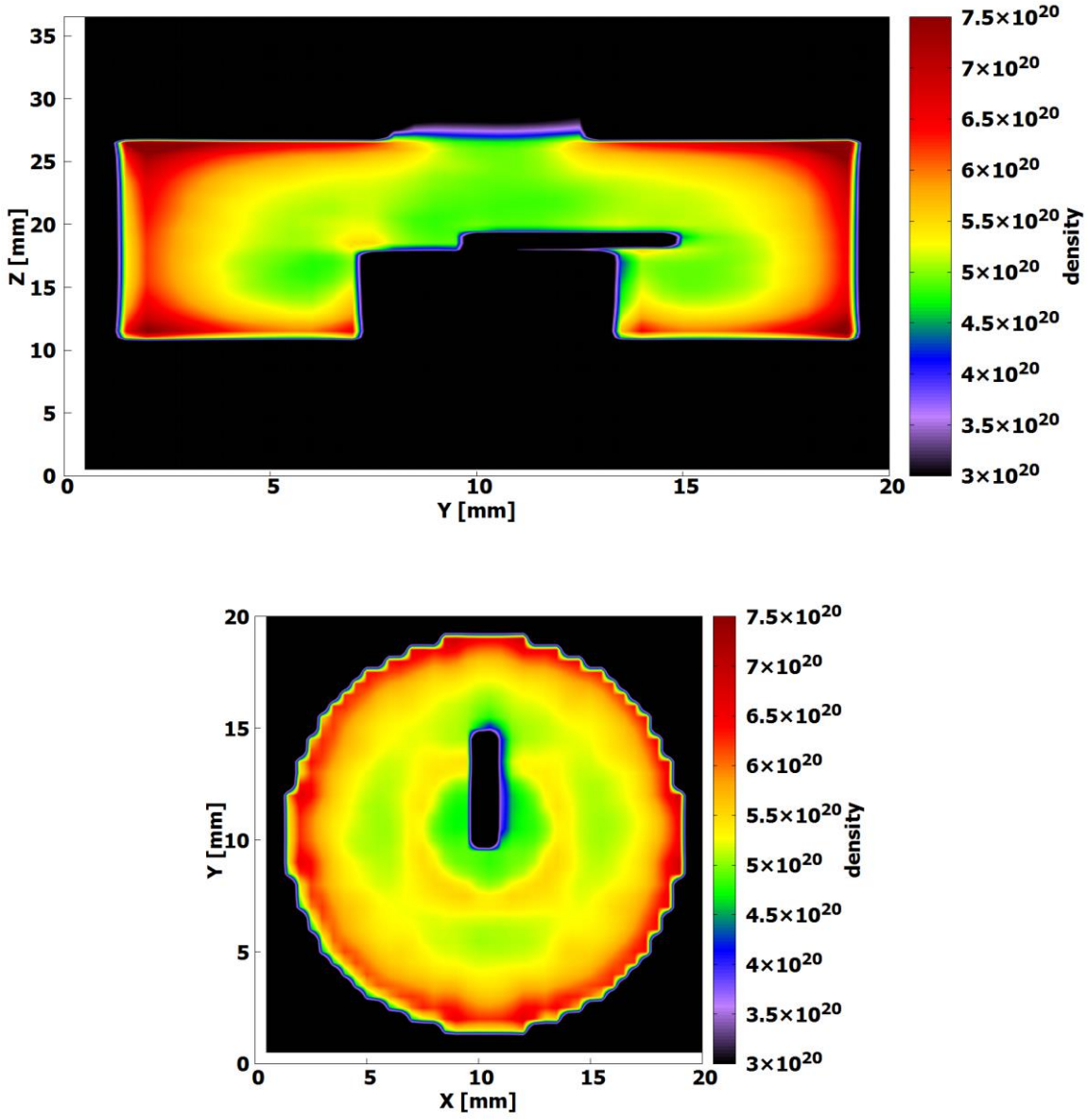

Figure. 2.6: Density Distribution of Neutrals for the 16 Bottom Inlets

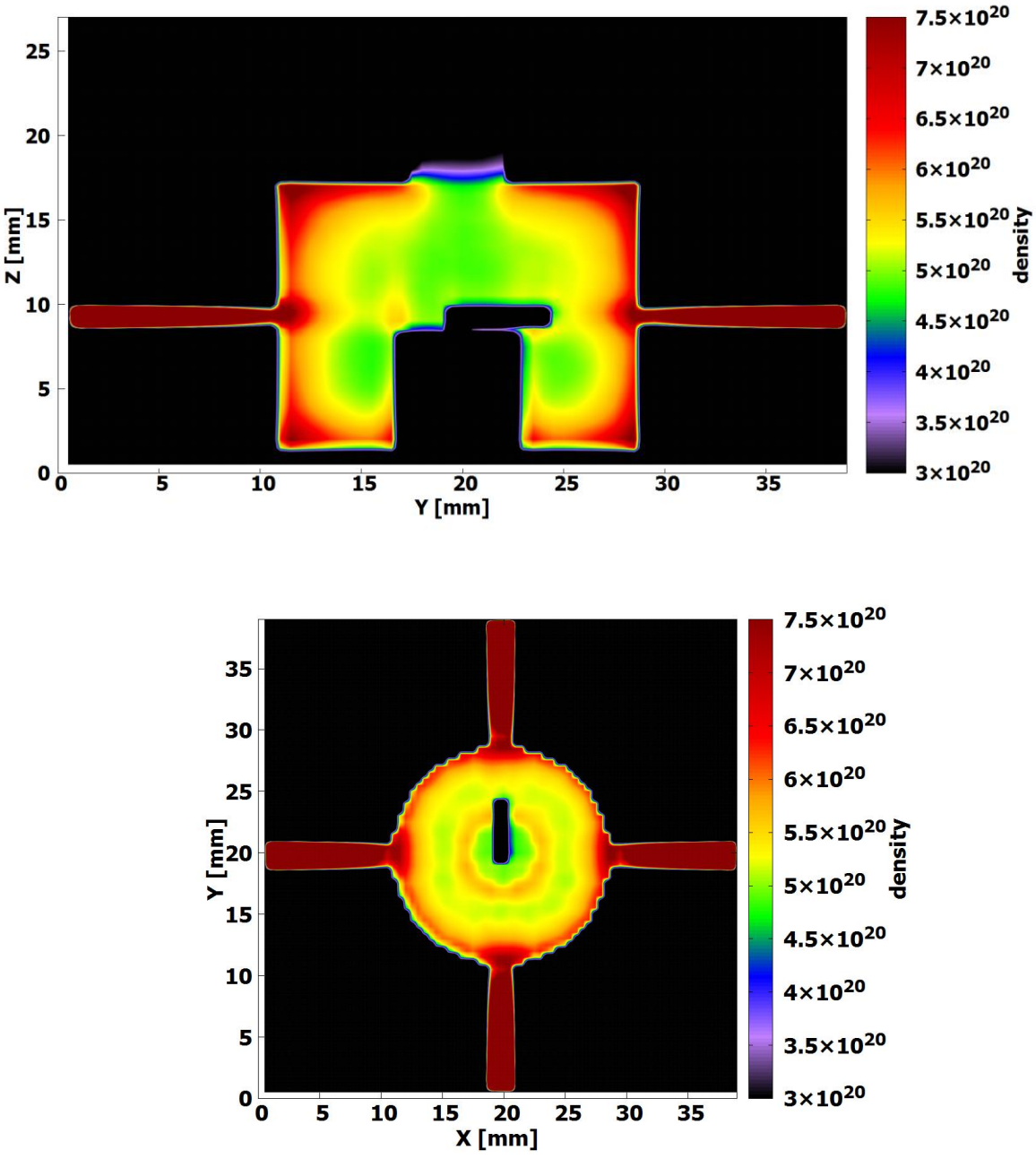

Figure. 2.7: Density Distribution of Neutrals for the 4 Horizontal Inlets

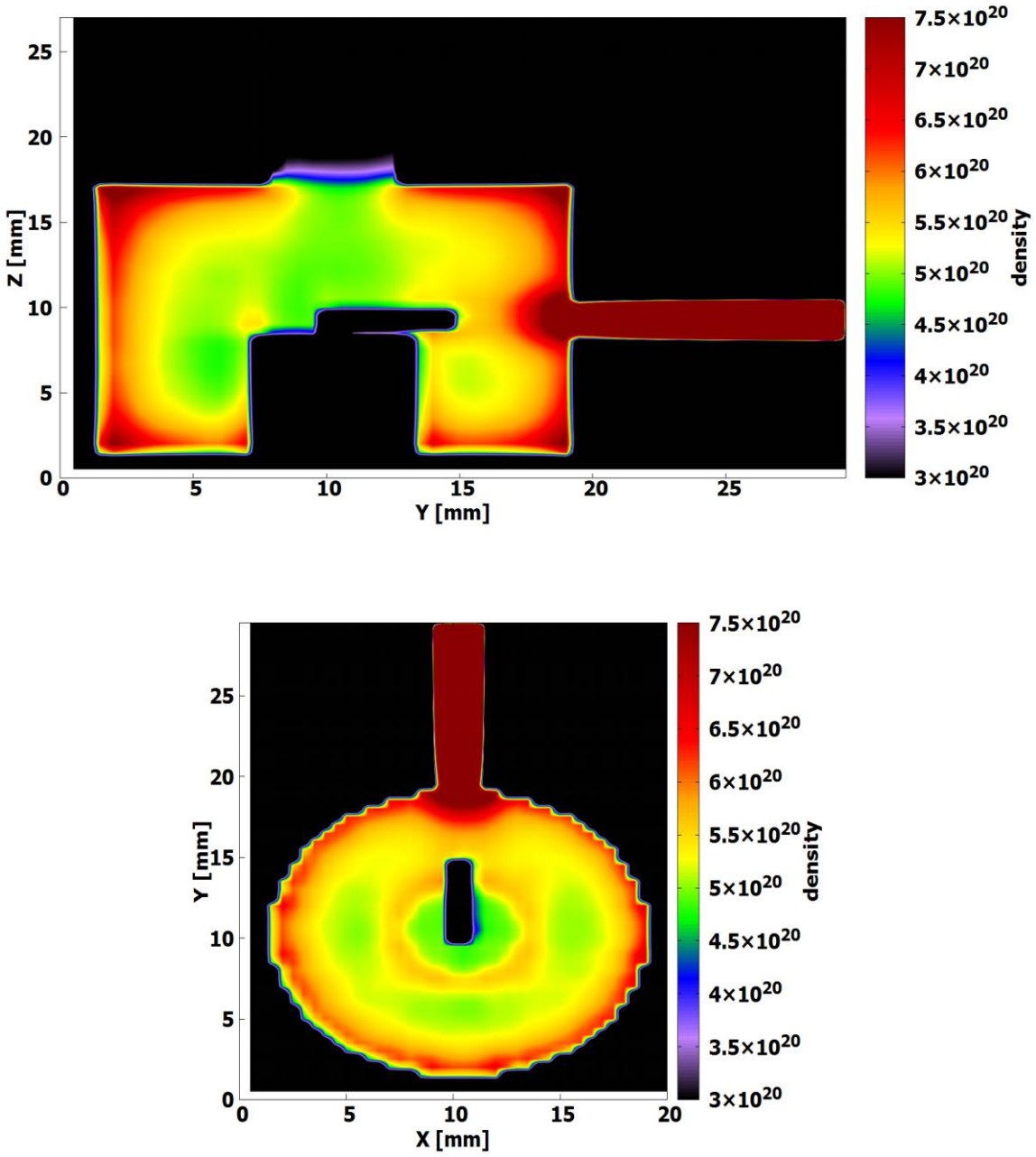

Figure. 2.8: Density Distribution of Neutrals for the One Horizontal Inlet

3

Simulation of Neutral Recycle rate and Ion density within a Neutralizer with respect to gas inlet configuration

In the previous section we have shown that the neutral density can be influenced through changes in the gas inlet. Since the ionization of neutrals is directly impacted by the neutral density, we hypothesized that ionization pattern and ion loss would follow the neutral distribution as well. In our current work we aim to focus on the neutral recycling phenomena. In electric propulsion systems, ion colliding with the conducting wall surfaces would gain an electron and are reflected back as a neutral. Depending on the purpose of the propulsion layout, this outcome might be beneficial or a detriment. While in the case of a neutralizer this would be welcomed, for an ion thruster the neutral recycling phenomena represents a loss of energy since these neutralized atoms must be ionized again and accelerated out of the system. We opt to minimize this performance loss. Regardless of the device being used, this phenomena is not well studied and the impacts of propulsion system design on its pattern are not well understood. There are limited works in this area that include neutral recycle and their simulations. A two dimensional simulation was developed by Komurasaki and Arakawa [49] in which a fluid model was utilized for electrons while ions were represented with a flux tube model for a hall thruster. This simulation also considered an ion wall interaction. Furthermore, Fife et al [50] developed a simulation where electrons where represented with a one dimensional fluid model while ions utilized a PIC code to simulate plasma wall interactions for a hall thruster. In the following works Boeuf et al [51-54] expanded on that simulation to analyze the impact of magnetic field on thruster performance. While these works and the ones discussed earlier [32-37] do focus on plasma wall interactions to varying degrees, their limit lies in the fact that neutrals were either not included or treated as background particles. Moreover, a comprehensive study of the impact of neutral recycling phenomena on performance as well as neutral density has not been done. Hence the motivation for our work. We developed a three-dimensional (3D) PIC simulation of ions and neutrals with the purpose of analyzing the changes in neutral density with respect to the recycling impact [55]. In this simulation, xenon neutrals and ions are treated as active particles while focusing on their behaviors through elastic collisions and wall interactions.

3.1 Simulation Geometry

We use the same neutralizer as the previous section seen in Figure 2.3. The internal design and calculation regions are shown in Figure 3.1. In order to investigate the impact of neutral density, four inlet configurations were considered for this study. Aside from the conventionally used single bottom inlet located right below the antenna, we simulated an additional 4 smaller uniformly dispersed bottom inlets. Two similar inlet configurations are also considered in a similar fashion with the inlets positioned horizontally at antenna height instead.

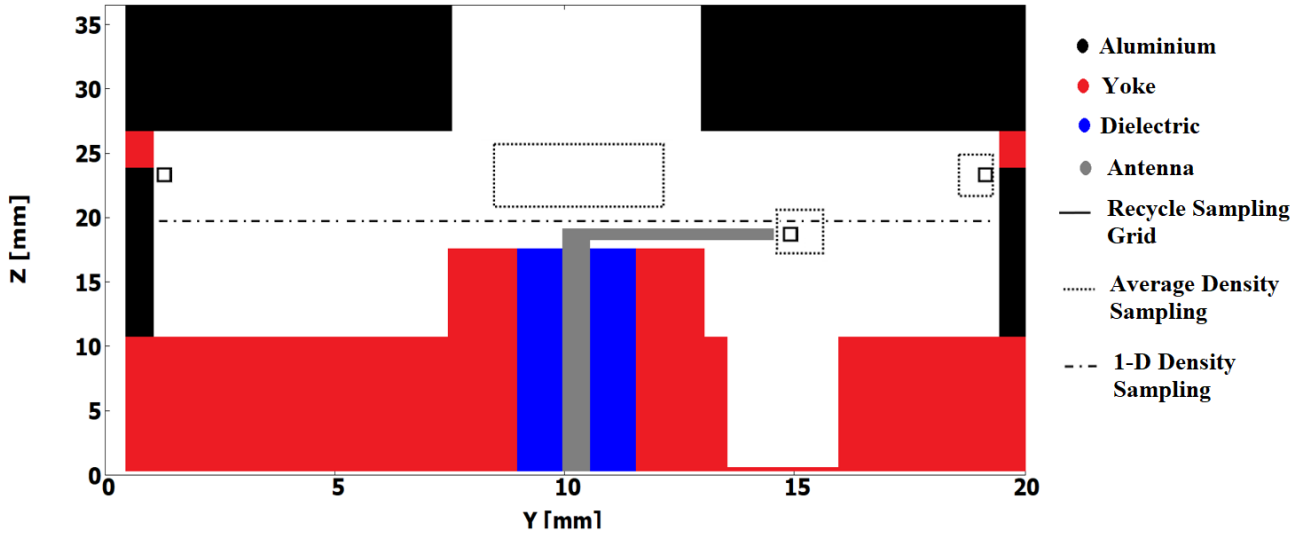

Figure. 3.1: Y-Z cross section of the neutralizer thruster taken at X = 10 mm (middle of the simulation geometry) for the conventional bottom inlet with allocated calculation regions

3.2 Simulation Properties

To investigate the impact of neutrals on ionization pattern and ion wall interactions independently, we do not consider the electromagnetic field impact on simulation particles. Although these assumptions will limit the accuracy of the simulation, it will provide an opportunity to study the direct impact of neutral density on ion behavior independent of electron motion. In the next section we will amend these assumptions by coupling the current code with a Finite Difference Time Domain (FDTD) simulation where a realistic electron motion with respect to electromagnetic field fluctuations is considered. The simulation properties are indicated in Table 3.1. Neutralizer walls are assumed to have a closed boundary condition where it diffusely reflects neutrals and recycles ions back to a neutral sate by behaving as a cathode. The orifice exit however has an open boundary for neutrals to leave the simulation while ions get reflected back due to assumed high potential. Electrons were assumed to have an initial uniform distribution and temperature throughout the discharge chamber with an average density of 5×10^{17} m^{-3} and a temperature of 6 eV [24]. Ionization begins after the neutrals have reached a steady state and

ionization rate is then calculated based on the electron temperature and xenon neutral density. However, as the simulation progresses, electrons are assumed to follow ion particles and therefore the ionization rate is reevaluated based on ion and neutral density at every time step. The ion and neutral particle interactions such as collisions and reflections utilizes a similar method as elaborated in section 2.1. Moreover, the ions and neutrals in this simulation also follow similar equations of motion (equations 2.1 through 2.5) as discussed in previous section. Furthermore, to study the specific impact the neutral recycling plays in the neutralizer, we compared the neutral and ion density throughout the neutralizer with two simulations for the single bottom inlet. One where the neutral recycling is ignored and the ions are simply reflected from the walls, and the other where the recycling impact is simulated. Comparing the changes in particle density in neutralizer`s specific segments would showcase the impact recycling has on performance. The flowchart of this simulation is shown in Figure 3.2.

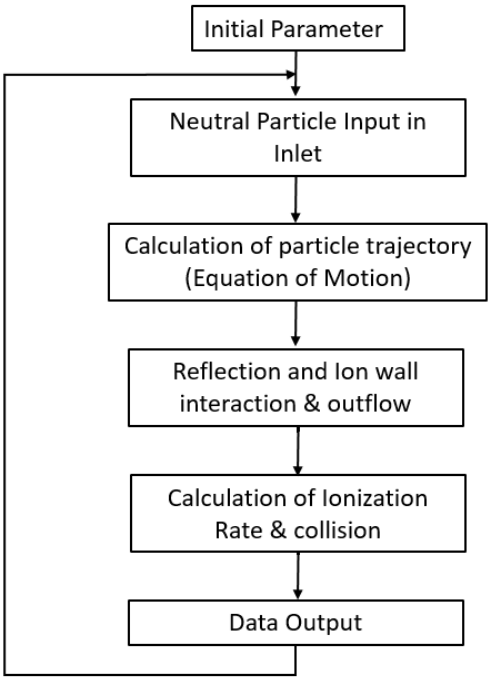

Figure. 3.2: Flowchart of the Ion-Neutral PIC code

Table. 3.1: PIC simulation properties for all 4 inlet positions

Grid Size (m)	5.0×10^{-4}
Time Step (s)	5.0×10^{-8}
Ion Super Particle Number	5.0×10^{8}
Neutral Super Particle Number	1.5×10^{9}
Neutral Mass Flow rate (mg/s)	4.9×10^{-2}

3.3 Simulation Results

3.3.1 Neutral recycle impact on particle density in bottom inlet

To better understand the specific impact of neutral recycle phenomena within the neutralizer, we consider the neutral density changes in the neutralizer for the bottom inlet case with a comparative analysis between the two aforementioned simulation methods. One with the recycling impact ignored and the other with the recycling simulated. Comparing the changes in particle density between these two simulations will clarify how recycling impacts neutral density in specific regions. Figure 3.3 indicates the result of this comparative analysis in one dimension taken along the Y axis. This data is extracted where the X axis is at the center of the neutralizer and the Z axis is right above the antenna (as seen in Figure. 3.1. The solid line indicates the neutral density at steady state without considering ionization which is used as a baseline for comparison. It can be seen that ionization without recycling results in a uniform ~3% drop in neutral density throughout the neutralizer as expected. However, by considering the recycling impact, the density at discharge chamber increases by ~2% coming slightly short of baseline while there is a small but significant increase in the neutral density near the antenna (close to 1% from baseline). This clearly indicates the major role antenna plays in the neutral recycle and density inside the neutralizer. The increase in the overall density after the antenna is due to the positioning of the gas inlet which feeds a constant stream of neutral particles throughout the simulation. In order to further analyze the neutral recycling impact, we also took neutral density samples from key regions of the neutralizer from the two simulation methods. These key regions are: near the tip of the antenna, discharge chamber and vicinity of the surrounding walls above and facing the inlet (Upper inlet wall) as depicted in Figure. 3.1.

Table 3.2 lists the average neutral densities taken at these key regions inside the neutralizer. Comparing the neutral densities without ionization (baseline) to the density including the recycling impact ignored leads to a drop in neutral density in a similar fashion in all areas as seen in

Figure 3.3. However, the true impact of recycling is seen by comparing the baseline density with that of ionization and recycling impact simulated. The changes in the discharge chamber are insignificant meaning that recycling of neutrals keeps their particle density in the discharge chamber unchanged for the most part. The density changes around the tip of the antenna on the other hand are significant and of interest. Although the increase in the neutral density around the antenna due to recycling (an increase of around 1%) is small, it is significant and more prominent that the changes near the inlet wall which shows an insignificant increase (around 0.5%). This further indicates the crucial impact neutral recycling has on neutral density distribution in different regions of the neutralizer. The critical role the antenna plays in neutral recycling is expected given the central positioning of the antenna leading to a higher probability of ion collision.

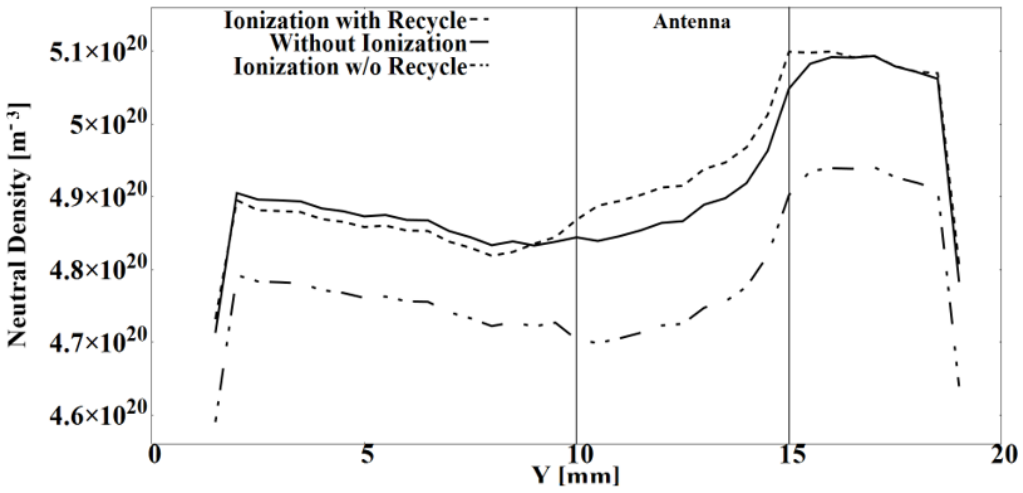

Figure. 3.3: Neutral density along the Y axis on the X-Z plane (X = 10 mm , Z = 17 mm).

Table. 3.2: Neutral density samples in the neutralizer (m^{-3}).

Calculation region	Neutral density before ionization	Neutral density with recycle	Neutral density without recycle
Discharge chamber	4.83×10^{20}	4.80×10^{20}	4.68×10^{20}
Tip of the antenna	5.13×10^{20}	5.18×10^{20}	4.98×10^{20}
Upper inlet wall	5.05×10^{20}	5.08×10^{20}	4.90×10^{20}

3.3.2 Inlet configuration impact on particle density and recycle rate

In order to study the gas inlet`s impact on neutral density, distribution of neutral particles at steady state considering ionization and recycling was collected. The outcome of this simulation of neutral particles for each inlet case is outlaid in Figures. 3.4-3.7. The results are taken at the y-z plane from the center of the neutralizer (X = 10 mm) and the x-y plane at antenna height (Z = 17 mm) were they best represent the entire neutralizer (as shown in Figure 3.1). Figure 3.4 shows the neutral density in the conventional inlet configuration. It can be seen that the neutral density is shifted slightly towards the inlet in that region which is also evident in Figure. 3.3. On the other hand, the four bottom inlets configuration in Figure. 3.5 does show a more uniform neutral distribution throughout the discharge chamber. Figures 3.6 and 3.7 show the neutral distribution for the horizontal inlets where both configurations have led to a significantly higher density of neutrals near the upper walls in contrast to the bottom inlets (an average increase of 5% comparing the two single inlets). While the single horizontal inlet has a disproportionate density distribution towards the inlet, the four smaller horizontal inlets offer a more uniform distribution within the discharge chamber. To further analyze the impact inlet configuration has on particle densities and recycling rate, the average neutral and ion densities in the discharge chamber for each inlet case is listed in Table 3.3. Also indicated in this table, is the average neutral recycling rate taken at the antenna and the surrounding walls above (upper walls). It is evident from the average particle densities that the average ion density in the discharge chamber remains similar despite the changes in the overall neutral density caused by different inlet layouts. While there are small significant changes in the neutral densities between horizontal and bottom inlets, these differences do not offer practical importance since ion densities remain similar. The neutral recycling rate however shows clear significant changes in different regions of the neutralizer for each case.

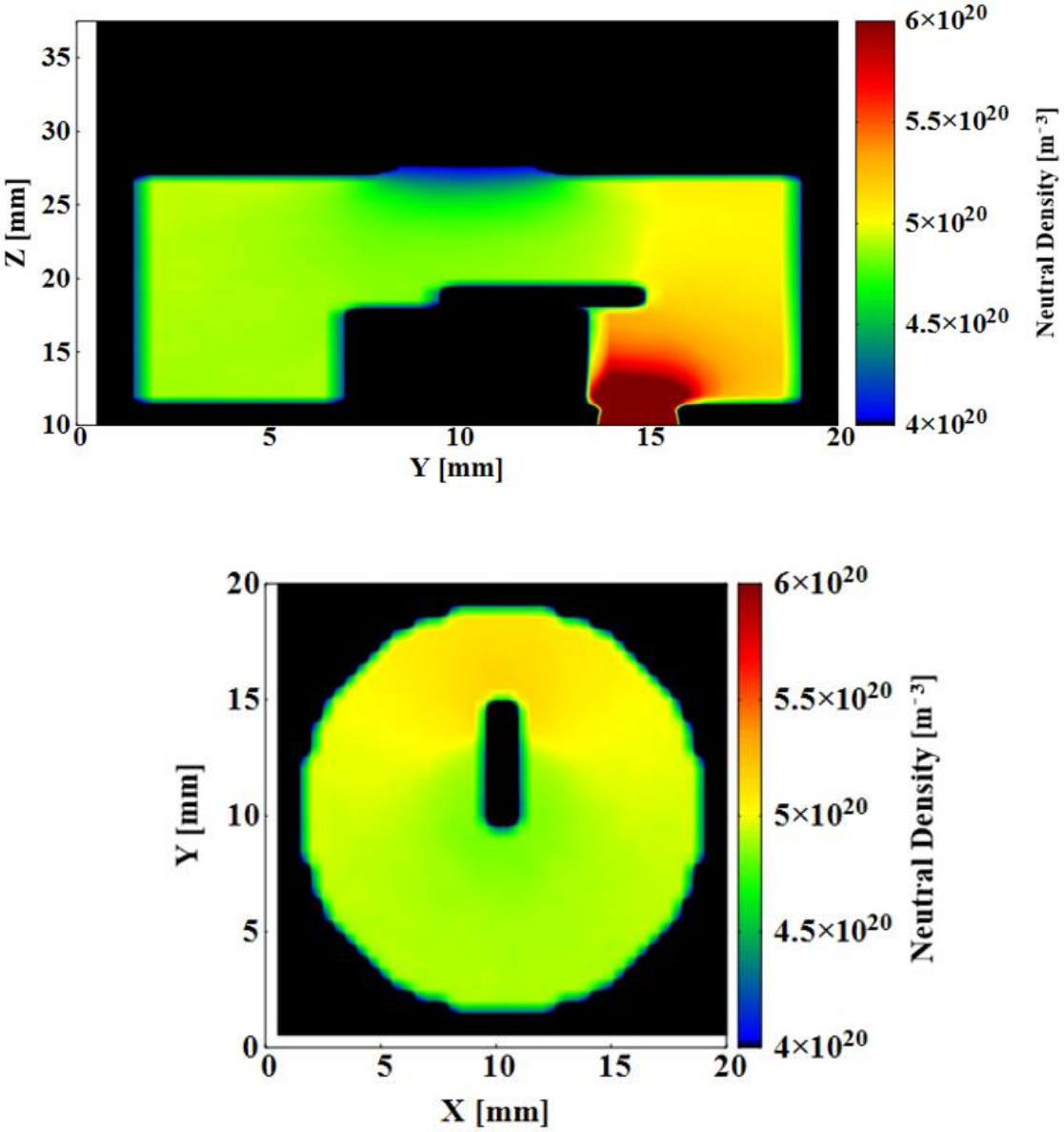

Figure. 3.4: Neutral density pattern for the bottom inlet configuration: (top) Y-Z plane and (bottom) X-Y plane.

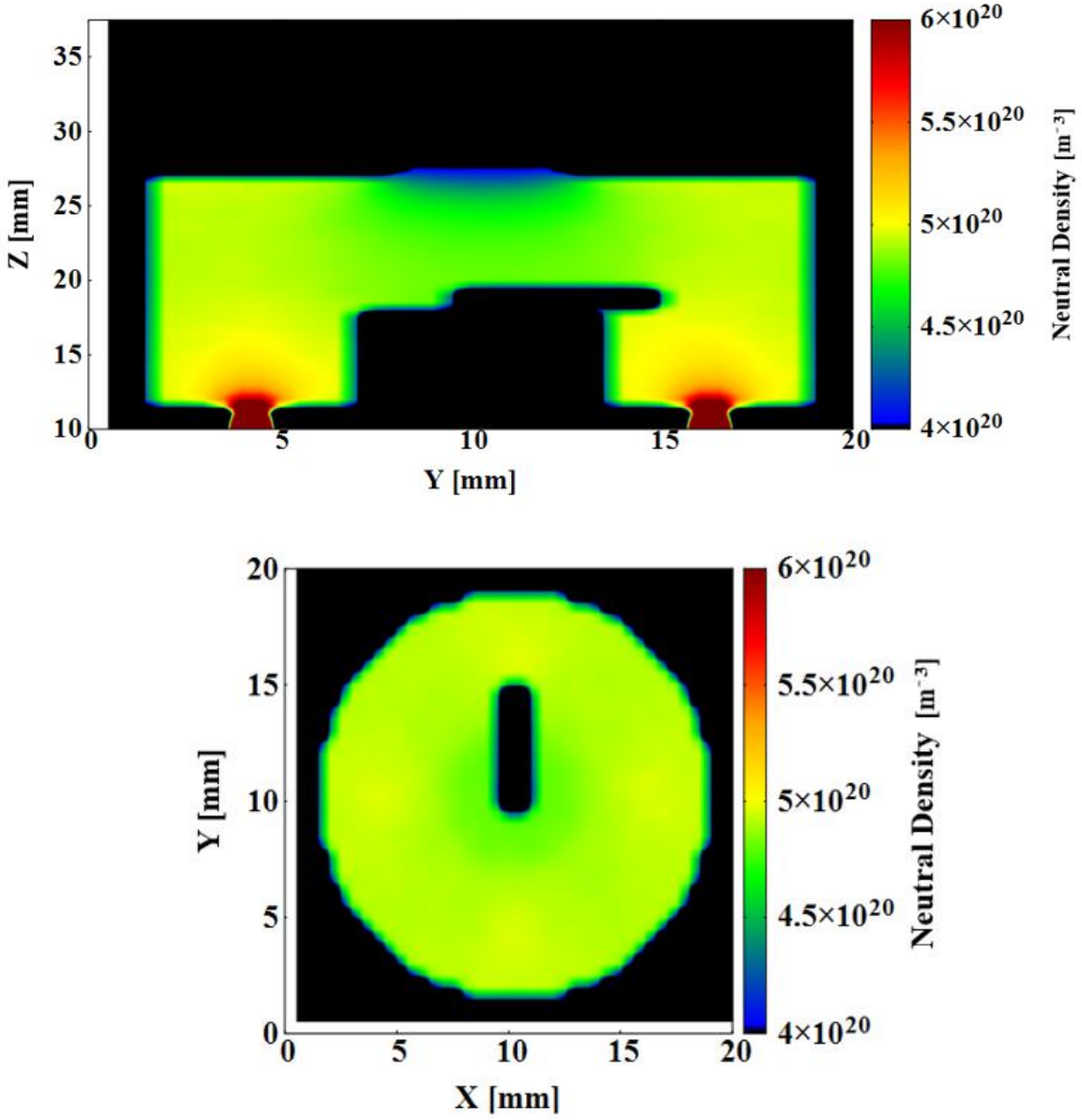

Figure. 3.5: Neutral density pattern for the four bottom inlets configuration: (top) Y-Z plane and (bottom) X-Y plane.

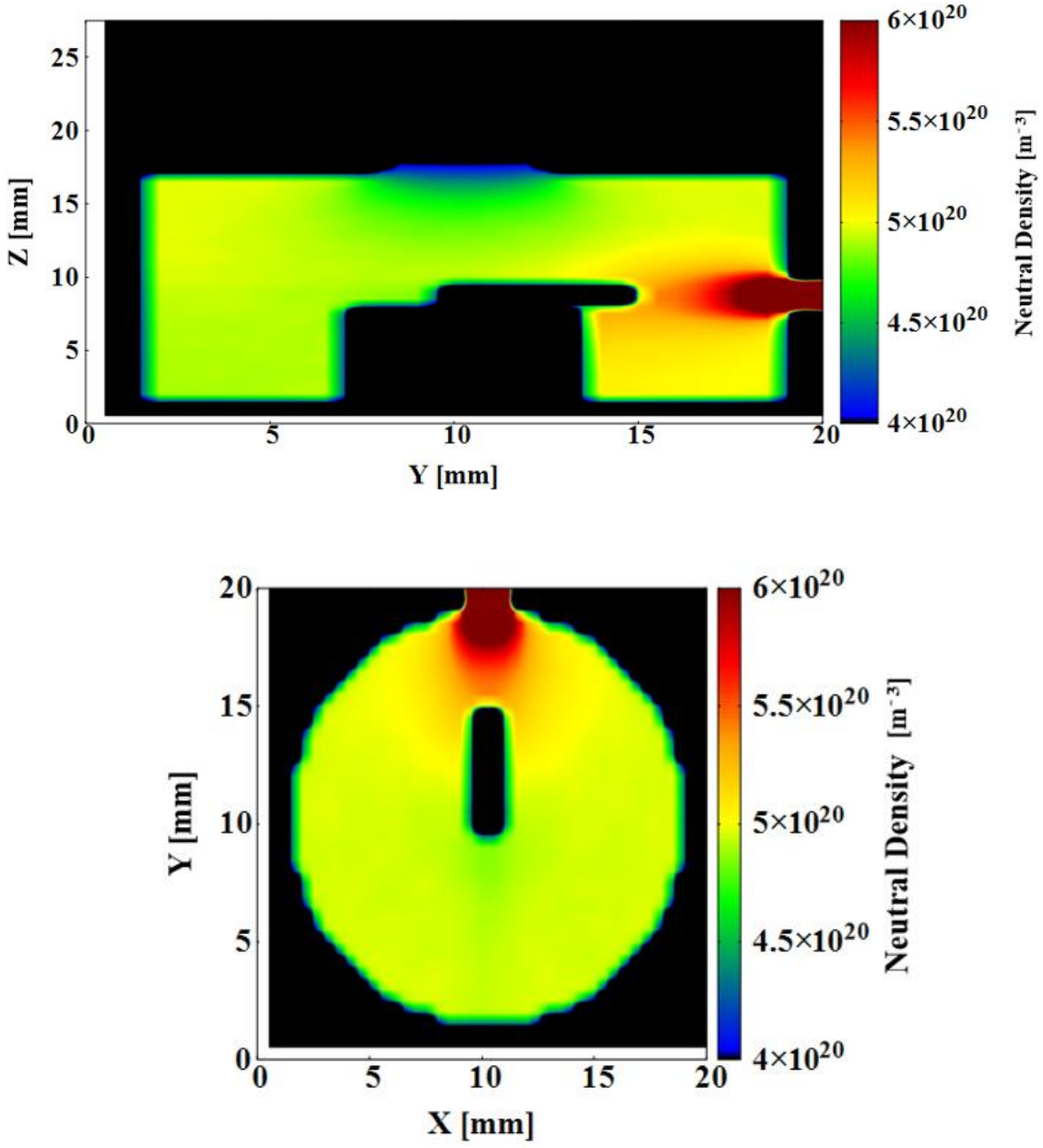

Figure. 3.6: Neutral density pattern for the single horizontal inlet configuration: (top) Y-Z plane and (bottom) X-Y plane.

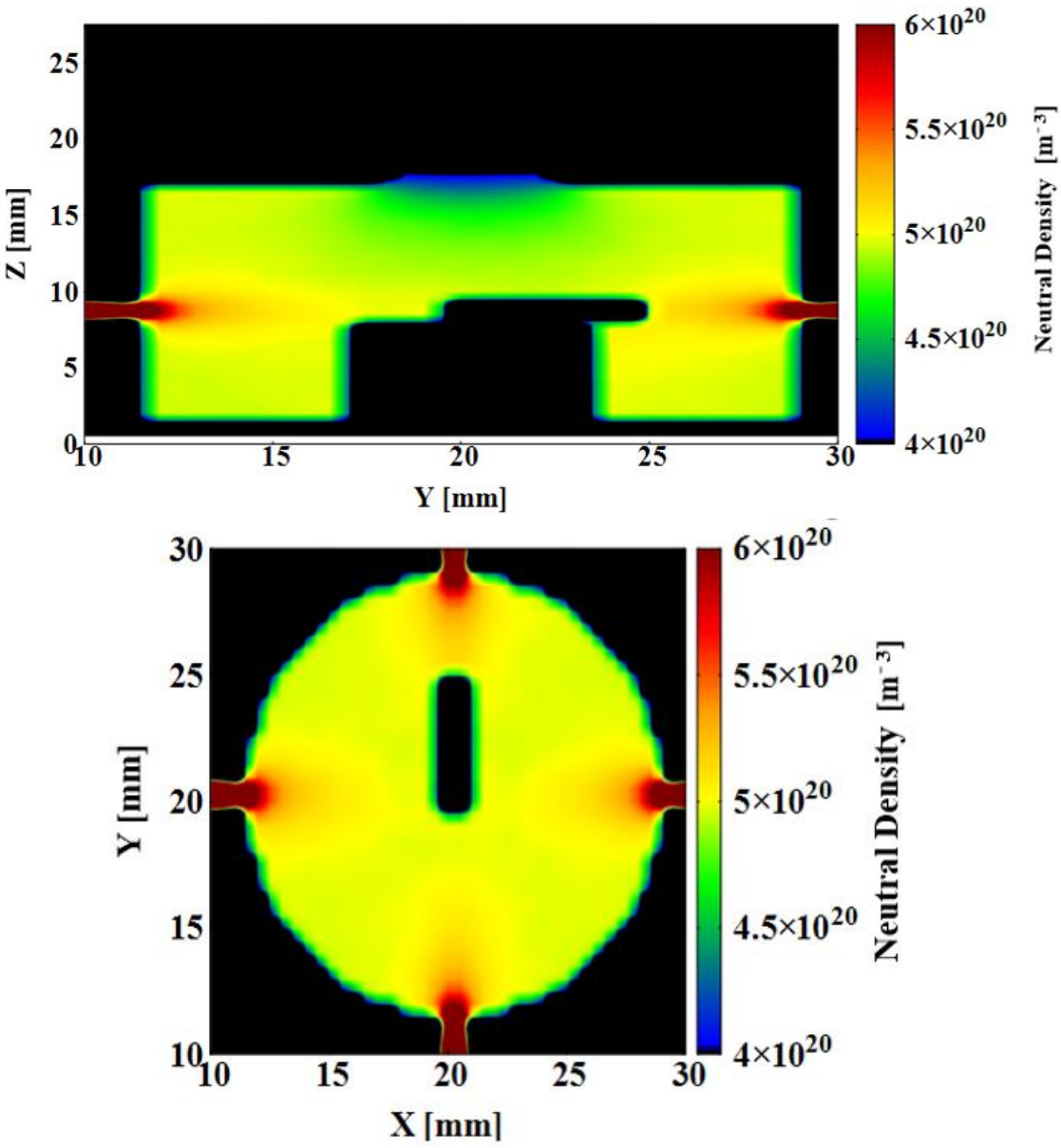

Figure. 3.7: Neutral density pattern for the four horizontal inlets configuration: (top) Y-Z plane and (bottom) X-Y plane.

Table. 3.3: Average density (m^{-3}) and recycle rate ($m^{-3}.s^{-1}$)

Inlet Layout	Neutral density in discharge chamber	Ion density in discharge chamber	Neutral recycle rate in antenna	Neutral recycle rate in upper walls
Bottom inlet	4.80×10^{20}	3.83×10^{18}	1.23×10^{22}	8.12×10^{21}
Four bottom inlets	4.79×10^{20}	3.81×10^{18}	1.21×10^{22}	8.05×10^{21}
Horizontal inlet	4.85×10^{20}	3.84×10^{18}	1.26×10^{22}	9.12×10^{21}
Four horizontal inlets	4.84×10^{20}	3.83×10^{18}	1.25×10^{22}	9.04×10^{21}

As seen in section 3.2.1, the antenna reintroduces remarkably higher number of neutrals than the walls on average and this is further evident in Table 3.3. All inlet cases considered, the antenna on average recycles 45% more neutrals per simulation cell than the upper walls. The antenna plays a key role in neutral recycling and this increase in neutral density occurs for all inlet configurations and is not dependent on neutral input configuration. This finding provides an opportunity for future research into the optimization of neutral recycling rate by altering the antenna configuration. Another notable finding is the difference in neutral recycle rate in upper walls between the horizontal inlets versus the bottom inlets. On average the horizontal inlets lose 12.3% more ions to the upper walls of the neutralizer than bottom inlet configurations. Upper walls are the major source of recycling due to their larger surface area in contrast to the antenna. This means that although the antenna has a significantly higher average recycling rate per unit area, the upper walls will introduce more neutrals back to the neutralizer overall. Therefore, horizontal inlet configurations do not offer any changes to the neutralizer's performance since despite significantly losing more ions to the upper walls, they do not appear to effect the ion density in the discharge chamber. This is due to the fact that inlet configurations mainly alter the neutral density near the walls and the resultant increase in ion density is countered by the increased rate of ion loss. As result the average ion density remains indistinguishable between inlets. This would leave us with the two bottom inlet configurations. However as seen in the X-Y planes in Figure. 3.4 and Figure. 3.5, these two inlets offer different neutral density distributions within the neutralizer. This can be seen with the variance of neutral densities taken at these X-Y planes. The conventional bottom inlet has a density variance of 9.80×10^{19} and the four bottom inlet configuration offers a lower variance of 9.02×10^{19} indicating the uniformity of neutral density distribution around the antenna in the four bottom inlet configuration in contrast to the conventional bottom inlet. This means that for a non-symmetrical antenna like the L shaped device used for this study, the single bottom inlet would be preferred while the four bottom inlets would be expected to benefit a more symmetrically shaped antenna. Our following work will focus on investigating this prospect. It is clear that the inlet configuration plays a role in ionization rate and neutral recycle rate due to its impact on average neutral density throughout the discharge chamber. This result is also evident in Figure. 3.4

where the inlet configuration clearly alters the distribution of neutrals within the discharge chamber as well as neutral recycle pattern shown in Table 3.3.

While previous works have studied the impact of ion loss on engine's performance, the effect of neutral density independent of other factors has not been well established. This is mainly due to the fact that electron density distribution plays a stronger role in determining the engine's performance. Although that may be the case, we have shown that by considering the recycling impact, the density distribution of neutrals would differ and offer an opportunity for optimization. This simulation can be validated with a comparison of its results with that of our own experimental data [24] as well as a previously designed three dimensional hybrid PIC simulation of a similar neutralizer [56-57] where the particle density results are within an acceptable range to our simulation results. This simulation however has several limitations. As mentioned earlier, initial electron temperature is assumed uniform throughout the discharge chamber and electromagnetic field impact is ignored. This is justified based on the fact that a strong electric field exists near wall and orifice as a sheath which plateaus the plasma potential within the neutralizers discharge chamber. This means that most ions within the discharge chamber only experience a small electric field to begin with. This assumption will allow us to investigate the independent impact of neutral particles. In the next section we will discuss a simulation where the electromagnetic field impact as well as the impact of inlet configuration on density distribution is analyzed.

4

3D FDTD-PIC Simulation of an Ion Thruster with respect to inlet configuration

We hypothesized that the neutral density distribution has the potential to influence the plasma properties inside the miniature ion thruster. Neutral density distribution is directly impacted by the inlet configuration where the changes in the inlet positioning can lead to unique distribution patterns as seen previous sections. However the simulation in the previous section had limits. Firstly, it did not consider the electromagnetic field propagation within the discharge chamber. Furthermore it treated electrons as background particles and it ignored the ambient magnetic field generated by the permanent magnets within the neutralizer. In this section we plan to address those shortcomings by developing a 3D FDTD-PIC simulation of a miniature ion thruster where all the particles (ions, electrons and neutrals) are treated as active particles as well including a Poisson solver in the code as a correction mechanism. Plasma flow simulation often follows two main techniques which are fluid models in contrast to kinetic ones. Depending on the plasma properties, flow conditions and the device in question as well as the acceptable accuracy of the simulation, either of these methods is utilized In the fluid method, the plasma may be considered as a fluid when the distance of the significant parameters such as charge separation distance or collision distance are small considering the thruster dimensions. Often these constraints are satisfied while simulating high density plasmas resisto-jets and arc jets. On the other hand, when parameters such as the collision and plasma distances are at a comparable or larger scale than the thruster dimensions, kinetic model is used. This applies to many of the electric propulsion systems including the miniature ion thruster we aim to simulate.

As mentioned in previous segments, the previous works in this field are not comprehensive in terms of neutral ion behavior with respect to engine configuration. While the work of Birdsall [38] was pioneering in neutral particle collision simulation, much like Boyd [39] they did not explore the possibility of system configuration on neutral density distribution. Other works often ignore the neutral atoms altogether by assuming a uniform neutral density as background.

Mahalingam and Menart [32-34] for example considered neutrals as inactive background particles. Although their work lead to a better understanding of electric field distribution within an ion thruster, it is limited due to the lack of neutral particle simulation and ion loss to the walls. Some of the previous works conducted in our research group [31] also falls to this limit where the simulation leads to unusual particle behavior in select regions due to lack of ion wall interaction inclusion. Although, some previous works in this field did simulate the ion loss phenomena within the propulsion system, impact of neutral particles on ion loss phenomena is often ignored which will lead to a degree of inaccuracy in their simulations as well. Komurasaki and Arakawa [49] for instance included ion wall interaction in their hybrid simulation (electrons utilizing a fluid model) which lead to an improved simulation of magnetic field inside the hall thruster. This model however did not consider the impact of neutrals on ion and electron density distribution as well as engine design changes that could improve it.

As mentioned, previous works often ignore the impact of neutral behavior the by treating them as background particles or ignoring them all together [30-37, 49-52]. Moreover no work has been done to our knowledge on the impact of gas inlet on neutral density and ion loss as a comparative study. This leave room for possible improvement in the performance of miniature ion thruster hence the motivation for our current work.

4.1 Simulation Method

The PIC part of this simulation will treat the collisions and wall interactions of these particles with each other while the FDTD segment along with the Poisson solver will treat the impact of the electromagnetic forces on electron particles and its propagation. In this simulation, electrons motion within the system is treated separately form the other particles due to the nature of simulation. Electrons are impacted by the ambient magnetic field as well as the fluctuations in the electromagnetic field caused by the microwave propagation. Ions on the other hand, are assumed to not be influenced by the microwave propagation due to their slower motion as a result of their significantly heavier mass. This means that ions movement is solely impacted by the ambient magnetic field. While ions are not impacted by the electromagnetic fluctuations, electron movement leads to an electrostatic field creation within the simulation. This field can impact ions behavior and should be considered. Our current work however does not include this electrostatic force impact as the simulation code developed is in its preliminary stage. Our future work will amend this aspect and continue the development of a more comprehensive simulation of a miniature ion thrusters. Finally in order to fully analyze the impact of gas inlet changes on the plasma properties inside the discharge chamber, this simulation was applied to a miniature ion thruster (depicted in Figure 1.4) considering the several inlet configurations as well as two candidate antenna shapes (L shaped and disk shaped) in order to analyze the impact of inlet configuration for different antenna configurations.

4.1.1 PIC Method

As mentioned earlier in section 2.1, the PIC method stores important information with regards to its special boundaries within each grid. These information include electromagnetic fields as well as current and particle densities. These stored information can then be used to extrapolate the impact of those electromagnetic fields on the electron particles within the cell and apply the equation of motion for each individual particles respectively.

the equation of motion for each electron particle is:

$$m\frac{dv}{dt} = q\ (E + v \times B) \qquad \text{eq. 4.1}$$

Where m is the particle mass, q is the charge, and E and B are the electric and magnetic fields respectively. For ions on the other hand, equation 4.1 is applied as well, however only the ambient magnetic field values are included in the equation. Finally neutrals in the simulation follow similar equations of motion as discussed in section 2.1.1.

These mesh sized are chosen with respect to the plasma Debye length defined bellow:

$$\lambda_D = \sqrt{\frac{\varepsilon_0 K_b T_e}{n_e e^2}} \qquad \text{eq. 4.2}$$

Where ε_0 is the permitivitty in vacuume, K_b is the Boltzmann constant, T_e is the electron temperature, n_e is the electron density and e is charge of an electron. The mesh sizes within a simulation cannot exceed the Debye length limit in each dimension and therefore each mesh size mush follow this constraint:

$$\Delta \leq \lambda_D \qquad \text{eq. 4.3}$$

Simulation time step will also be constrained by the plasma frequency defined as:

$$\omega_{pe} = \sqrt{\frac{n_e e^2}{\varepsilon_0 m_e}} \qquad \text{eq. 4.4}$$

Where m_e is the electron mass. Similarly, simulation time step must be

$$\Delta t \ \leq \ \omega_{pe}^{-1} \qquad \text{eq. 4.5}$$

Additionally, charged particles cyclotron motion should also be considered since ion thrusters and neutralizers utilize permanent magnets. A particles cyclotron frequency is defined by:

$$\omega_c = \frac{eB}{m_e} \qquad \text{eq. 4.6}$$

Finally, simulation time step must also follow the Courant condition as follows

$$\Delta t \leq \frac{1}{v\sqrt{\frac{1}{\frac{1}{\Delta x^2}+\frac{1}{\Delta y^2}+\frac{1}{\Delta z^2}}}} \qquad \text{eq. 4.7}$$

Where v in this case will be the speed of light in vacuum.

Numerical Heating

In addition to the constraints introduced above, a PIC simulation should consider a phenomena called numerical heating as well. Numerical heating, (also known as unphysical heating [58-59]) refers to the potential inaccuracies that could arise within a PIC code leading to an incorrect fluctuation of field values caused purely as a result of simulation parameters rather than the physical factors. Considering the relatively cold plasma generated in an ion thruster, the main potential numerical heating factor that could arise is called scattering heating.

PIC method divides the space into discrete mesh where the field values representing that distinct space are stored. Furthermore, large groups of physical particles are summarized into unique simulation particles (super particles) to lower calculation cost. This means that the realistic continuous fields and densities are represented by discrete super particles. Since the number of super particles within the system are significantly smaller than the physical plasma, a single super particle migration from one simulation cell to the next will represent a large movement of physical particles. This would lead to random fluctuations in the system which would create localized electric fields acting on simulation particles. Since this phenomena is purely caused by the simulation factors (not by the physical parameters), a PIC code should aim to minimize this effect and correct it. This can be done through adopting a smaller mesh size and super particle number when possible. Considering the relatively low density plasma occurring in the miniature ion thruster as well as the extra fine mesh and the smaller super particle number which will be used for the simulation in this section, we do not expect numerical heating to have significant impact on the simulation result. As mentioned earlier, current work does not account for the electrostatic field present in the system as well. Our future work will amend this shortcoming and will analyze the possible impact of numerical heating on the static electric field.

4.1.2 Particle Collisions

As mentioned in section 2.1.2 the Collison probability is calculated from equation 2.9. However since there are different particles types in this simulation, the probability for each collision type should be elaborated. There are three types of collisions that occur between an electron and a neural particle. These are elastic, excitation and ionization. The simulation needs to distinguish between these types as well as be able to determine the probability for each. This is done through comparison of collision cross section σ based on the electrons energy. σ is a function of the particles energy and plotting this cross section with respect to the energy of the particle would lead to Figure 4.1.

$$\sigma \ = \ \sigma(E) \qquad \text{eq. 4.8}$$

This figure shows that for each energy level, there are unique collision type cross section which can be used to calculate the probability of each collision type with repast the energy level. This probability can be distinguished using the random number. As seen in the equations bellow, if the random number fall between the ratio of collision type cross section and the overall cross section that will specify the type of the collision.

$$\sigma_{total} \ = \sigma_{elastic} + \ \sigma_{excitation} + \ \sigma_{ionization} \qquad \text{eq. 4.9}$$

Therefore, if the random number falls bellow this ratio,

$$0 \ \leq r \ \leq \frac{\sigma_{elastic}}{\sigma_{total}} \qquad \text{eq. 4.10}$$

Then an elastic collision occurs. Similarly, if the random number falls between these ratios,

$$\frac{\sigma_{elastic}}{\sigma_{total}} \ \leq r \ \leq \frac{\sigma_{elastic} + \sigma_{excitation}}{\sigma_{total}} \qquad \text{eq. 4.11}$$

Then an excitation collision occurs. And finally and ionization collision probably is

$$\frac{\sigma_{elastic}+\sigma_{excitation}}{\sigma_{total}} \ \leq r \ \leq \frac{\sigma_{elastic} + \sigma_{excitation}+ \sigma_{ionization}}{\sigma_{total}} \qquad \text{eq. 4.12}$$

The alterations that occur for each particles energy level and velocity after the collision should be individually calculated as well. The method is described below [58-59]:

Elastic Collision:

Considering a particle pair with an incident velocity of (v_1, v_2), the resultant velocity of $(\acute{v}_1, \acute{v}_2)$ after the collision is:

$$\acute{v}_1 \ = \frac{1}{2} \ (v_1 + \ v_2 - \acute{u}) \qquad \text{eq. 4.13}$$

$$\acute{v}_2 = \frac{1}{2}(v_1 + v_2 + \acute{u}) \quad \text{eq. 4.14}$$

Where $\acute{u} = \acute{v}_2 - \acute{v}_1$ is the relative speed. Since this collision occurs between an electron and a neutral, the velocities are identified as $\acute{v}_e$ and $\acute{v}_n$. In this collision since electrons speed is considerably higher than the neutrals, we can ignore the neutral velocity and define the relative speed as $\acute{u} = \acute{v}_n - \acute{v}_e \cong -\acute{v}_e$. Consequently, if the mass of the neutral is M and mass of the electron is m following the law of conservation of energy we get:

$$\acute{v}_e = \frac{m+Mcos\varkappa}{m+M} v_e + \frac{M\,sin\varkappa}{m+M} h \quad \text{eq. 4.15}$$

Here h is defined as:

$$h_x = v_{er}cos\varphi \quad \text{eq. 4.16}$$

$$h_y = \frac{v_{ex}v_{ey}cos\varphi - v_e v_{ez}sin\varphi}{v_{er}} \quad \text{eq. 4.17}$$

$$h_z = \frac{v_{ex}v_{ez}cos\varphi - v_e v_{ey}sin\varphi}{v_{er}} \quad \text{eq. 4.18}$$

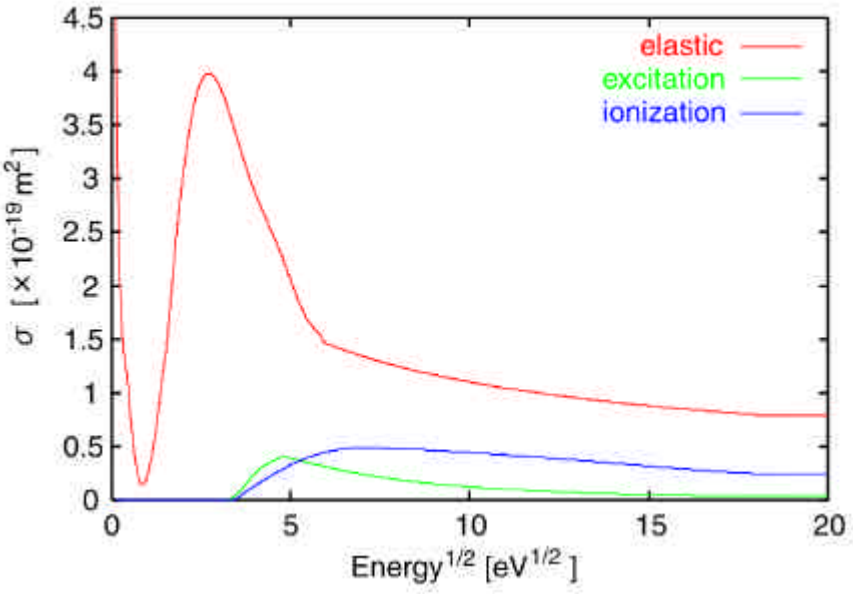

Figure 4.1: Electron Collision Cross Sections for Xe atom [61]

and

$$v_{er} = \sqrt{v_{ey}^2 + v_{ez}^2} \quad \text{eq. 4.19}$$

$$v_e = \sqrt{v_{ex}^2 + v_{ey}^2 + v_{ez}^2} \quad \text{eq. 4.20}$$

Here $\varkappa$ is the scattering angle and φ is a randomly assigned angle. Now considering the possible changes in the electron energy, for an elastic type collision it is generally assumed that the electron does not lose of gain energy and that its incident and scattered energy are identical.

$$E_{incident,e} = E_{scattered,e} \quad \text{eq. 4.21}$$

The scattering angle is a function of the incident energy (in eV) and it is calculated by:

$$cos\varkappa = 1 + \frac{2(1-(1+E_{incident,e})^r)}{E_{incident,e}} \quad \text{eq. 4.22}$$

And finally the randomly assigned angle φ is generated by using a random number r

$$\varphi = 2\pi r \quad \text{eq. 4.23}$$

Figure 4.2 indicates this trajectory assignment.

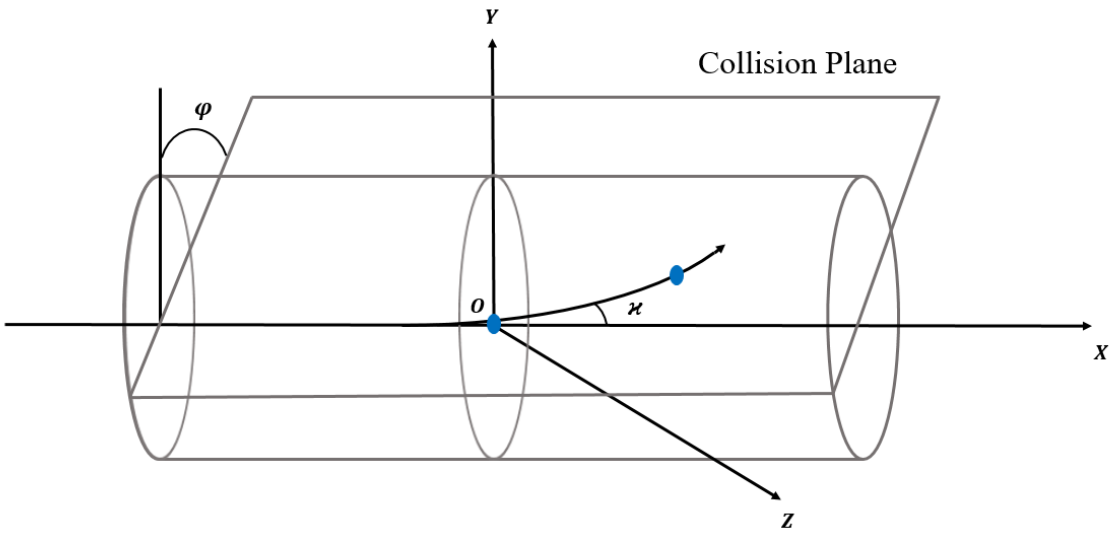

Figure 4.2: Particle Trajectory after Collision

Excitation Collision:

An excitation collision is where an electron with the incident energy of $E_{incident,e}$, spends energy ($E_{excitation,e}$) to excites the neutral atom from the ground state. Therefore its energy balance is:

$$E_{scattered,e} = E_{incident,e} - E_{excitation,e} \quad \text{eq. 4.24}$$

And its velocity after excitation is:

$$\tilde{v} = v_e\sqrt{1 - \frac{E_{excitation,e}}{E_{incident,e}}} \quad \text{eq. 4.25}$$

Here it can be considered that the excitation collision is a combination of an elastic and excitation collision where after the electron loses its energy it will have an elastic collision with its new velocity $\tilde{v}$ with the neutral atom. In our simulation, the $E_{excitation,e}$ for the Xenon atom was set at an average of 8.34 eV [61] based on Figure 4.1 .

Ionization Collision:

In an ionization collision, the incident election with the energy of $E_{incident,e}$ collides with the neutral and through losing the ionization energy of $E_{ionization}$ generates a new electron with the energy of $E_{created,e}$ and as always is scattered with its final energy of $E_{scattered,e}$. therefore the energy balance formula in this scenario is:

$$E_{scattered,e} + E_{created,e} = E_{incident,e} + E_{ionization} \quad \text{eq. 4.26}$$

The energy of scattered electrons after ionization is obtained by [42]:

$$E_{scattered,e} = Btan(\, r\, tan^{-1}(\frac{E_{incident,e} - E_{ionization}}{2B})) \quad \text{eq. 4.27}$$

Where B is a gas specific value for which Xenon has a value of 8.7 eV. Therefore the energy loss due to ionization for an incident electron is:

$$\Delta E = E_{incident,e} - E_{scattered,e} \quad \text{eq. 4.28}$$

With this in mind in a similar manner to the excitation collision and based on equation 2.33, the electron velocity after ionization is:

$$\tilde{v} = v_e\sqrt{1 - \frac{\Delta E}{E_{incident,e}}} \quad \text{eq. 4.29}$$

The scattering angle is calculated from equation 4.23 where the incident energy in that equation is obtained from equation 4.28. Finally the ionization energy for a Xenon atom is assumed at 12.13eV.

As for the generated electron, its energy is given by:

$$E_{created,e} = \Delta E - E_{ionization} \quad \text{eq. 4.30}$$

Finally the velocity of the generated electron is obtained using the velocity of the incident electron v_e in equation 4.16 by assuming that an elastic collision has happened where the outcome is the generated electron. The scattered angle can also be calculated using equation 4.23 by using the generated electron energy instead.

Null Collision:

Since every electron within the system must go through the collision probably calculation method elaborated above, this will greatly add to the calculation cost. The null collision method [56] helps to alleviate this cost by adding a fictitious cross section to each energy cross section represented in Figure 4.1. this fictitious cross section is called σ_{fake}

$$\sigma_{fake} < \sigma_{total} \quad \text{eq. 4.31}$$

This way an electron neutral collision will be amended to:

$$\sigma_{total} = \sigma_{elastic} + \sigma_{excitation} + \sigma_{ionization} + \sigma_{fake} \quad \text{eq. 4.32}$$

And therefore,

$$\sigma_{total}.v = \frac{\upsilon}{\mathrm{n_{gas}}} = constant \quad \text{eq. 4.33}$$

By introducing the fictitious cross section, the collision frequency and probability becomes a constant and is no longer dependent on energy. This means that the simulation can immediately judge if a particle will result to a Collison or not allowing the code to skip the unnecessary calculations. Meaning when the condition in equation below occurs, there is no collision and code can skip this particle.

$$\frac{\sigma_{elastic} + \sigma_{excitation} + \sigma_{ionizatoin}}{\sigma_{total}} \leq r \leq 1 \quad \text{eq. 4.34}$$

Figure 4.3 shows the collision frequency normalized by particle density of Xenon gas. The $\frac{\upsilon}{\mathrm{n_{gas}}}$ used here is set at 2.0×10^{-12} $\frac{m^3}{s}$.

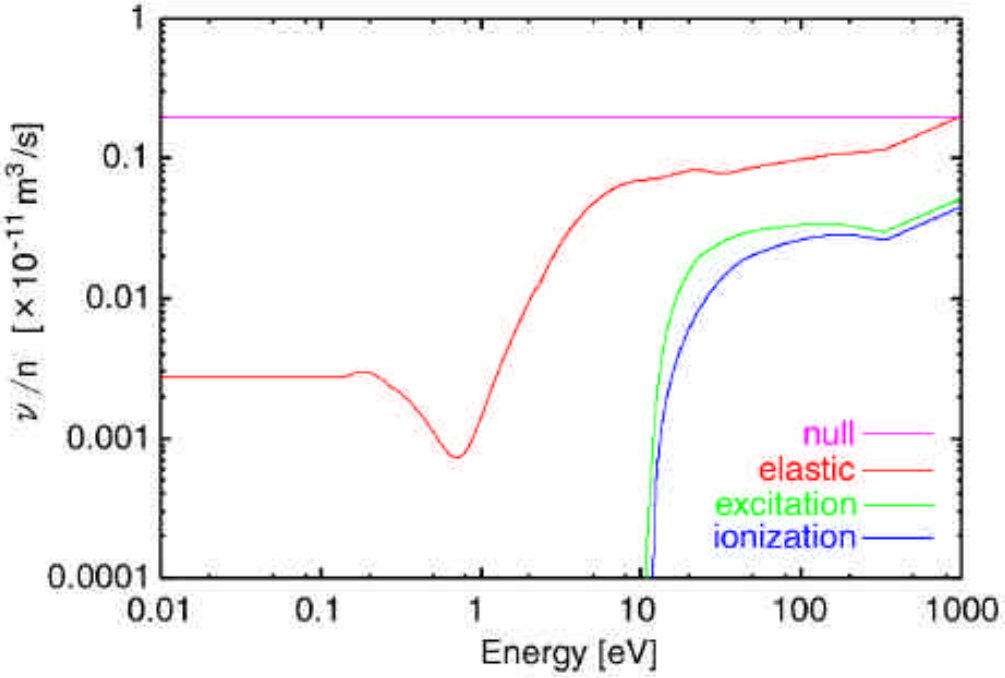

Figure 4.3: Electron-Xenon collision frequency normalized by xenon density [61]

Neutral Collision:

One unique aspect of our current work is the inclusion of neutral particles as active particles in our simulation. This means in our code, neutrals are not treated as background particles but rather are simulated as active particles with the collisions and interactions taken into account. Neutral-Neutral collision as well as Ion-Neutral collisions follow a similar method as elaborated in section 2.1.2.

4.1.3 FDTD Method

FDTD (Finite Difference Time Domain) simulation method is extensively used in plasma simulation as a way to calculate the fluctuations of electric and magnetic field values with respect to space and time. Therefore, this method is utilized to simulate propagation of electromagnetic waves and charged particles. The microwave input method used in the previous works involves a simplistic coaxial cable with a partial microwave input [17,62-66]. In this section we will analyze a more comprehensive microwave simulation in an actual coaxial cable geometry with a comprehensive microwave input method in a 3D model. This input method being briefly introduced in this textbook [67] was also inspired by [23,68] in which a two dimensional cable was simulated.

Field Calculation

Figure 4.4 indicates a FDTD grid with the field grid points labeled. Since none of the field points fits on the grid, developing a 3D FDTD simulation becomes complicated due to its calculation and indexing. Adjusting the original Maxwell equations to the simulation model in Figure 4.4 is a challenging task. Considering the basic scalar Maxwell equations in three dimensions [69]:

$$\frac{\partial B_x}{\partial t} = \frac{\partial E_y}{\partial z} - \frac{\partial E_z}{\partial y} \quad \text{eq. 4.35}$$

$$\frac{\partial B_y}{\partial t} = \frac{\partial E_z}{\partial x} - \frac{\partial E_x}{\partial z} \quad \text{eq. 4.36}$$

$$\frac{\partial B_z}{\partial t} = \frac{\partial E_x}{\partial y} - \frac{\partial E_y}{\partial x} \quad \text{eq. 4.37}$$

$$\varepsilon \frac{\partial E_x}{\partial t} = \frac{1}{\mu}\left(\frac{\partial B_z}{\partial y} - \frac{\partial B_y}{\partial z}\right) - j_x \quad \text{eq. 4.38}$$

$$\varepsilon \frac{\partial E_y}{\partial t} = \frac{1}{\mu}\left(\frac{\partial B_x}{\partial z} - \frac{\partial B_z}{\partial x}\right) - j_y \quad \text{eq. 4.39}$$

$$\varepsilon \frac{\partial E_z}{\partial t} = \frac{1}{\mu}\left(\frac{\partial B_y}{\partial x} - \frac{\partial B_x}{\partial y}\right) - j_z \quad \text{eq. 4.40}$$

By transforming these equations to the grid point system in Figure 4.4, Maxwell's equations can be utilized in the simulation. Therefore the equations about can be transformed to:

$$\frac{B^{n+\frac{1}{2}}_{x\left(i,j+\frac{1}{2},k+\frac{1}{2}\right)} - B^{n-\frac{1}{2}}_{x\left(i,j+\frac{1}{2},k+\frac{1}{2}\right)}}{\Delta t} = \frac{E^n_{y\left(i,j+\frac{1}{2},k+1\right)} - E^n_{y\left(i,j+\frac{1}{2},k\right)}}{\Delta z} - - \frac{E^n_{z\left(i,j+1,k+\frac{1}{2}\right)} - E^n_{z\left(i,j,k+\frac{1}{2}\right)}}{\Delta y} \quad \text{eq. 4.41}$$

$$\frac{B^{n+\frac{1}{2}}_{y\left(i+\frac{1}{2},j,k+\frac{1}{2}\right)} - B^{n-\frac{1}{2}}_{y\left(i+\frac{1}{2},j,k+\frac{1}{2}\right)}}{\Delta t} = \frac{E^n_{z\left(i+1,j,k+\frac{1}{2}\right)} - E^n_{z\left(i,j,k+\frac{1}{2}\right)}}{\Delta x} - \frac{E^n_{x\left(i+\frac{1}{2},j,k\right)} - E^n_{x\left(i+\frac{1}{2},j,k+1\right)}}{\Delta z}$$

eq. 2.54

$$\frac{B_{z\left(i+\frac{1}{2},j+\frac{1}{2},k\right)}^{n+\frac{1}{2}} - B_{z\left(i+\frac{1}{2},j+\frac{1}{2},k\right)}^{n-\frac{1}{2}}}{\Delta t} = \frac{E_{x\left(i+\frac{1}{2},j+1,k\right)}^{n} - E_{x\left(i+\frac{1}{2},j,k\right)}^{n}}{\Delta y} - \frac{E_{y\left(i,j+\frac{1}{2},k\right)}^{n} - E_{y\left(i+1,j+\frac{1}{2},k\right)}^{n}}{\Delta x} \quad \text{eq. 4.42}$$

$$\varepsilon_0 \frac{E_{y\left(i,j+\frac{1}{2},k\right)}^{n} - E_{y\left(i,j+\frac{1}{2},k\right)}^{n-1}}{\Delta t} = \frac{1}{\mu_0}\left(\frac{B_{x\left(i,j+\frac{1}{2},k+\frac{1}{2}\right)}^{n-\frac{1}{2}} - B_{x\left(i,j+\frac{1}{2},k-\frac{1}{2}\right)}^{n-\frac{1}{2}}}{\Delta z} - \frac{B_{z\left(i-\frac{1}{2},j+\frac{1}{2},k\right)}^{n-\frac{1}{2}} - B_{z\left(i+\frac{1}{2},j+\frac{1}{2},k\right)}^{n-\frac{1}{2}}}{\Delta x}\right) - j_{y\,(i,j+\frac{1}{2},k)} \quad \text{eq. 4.43}$$

$$\varepsilon_0 \frac{E_{x\left(i+\frac{1}{2},j,k\right)}^{n} - E_{x\left(i+\frac{1}{2},j,k\right)}^{n-1}}{\Delta t} = \frac{1}{\mu_0}\left(\frac{B_{z\left(i+\frac{1}{2},j+\frac{1}{2},k\right)}^{n-\frac{1}{2}} - B_{z\left(i+\frac{1}{2},j-\frac{1}{2},k\right)}^{n-\frac{1}{2}}}{\Delta y} - \frac{B_{y\left(i+\frac{1}{2},j,k+\frac{1}{2}\right)}^{n-\frac{1}{2}} - B_{y\left(i+\frac{1}{2},j,k-\frac{1}{2}\right)}^{n-\frac{1}{2}}}{\Delta z}\right) - j_{x\,(i+\frac{1}{2},j,k)} \quad \text{eq. 4.44}$$

$$\varepsilon_0 \frac{E_{z\left(i,j,k+\frac{1}{2}\right)}^{n} - E_{z\left(i,j,k+\frac{1}{2}\right)}^{n-1}}{\Delta t} = \frac{1}{\mu_0}\left(\frac{B_{y\left(i+\frac{1}{2},j,k+\frac{1}{2}\right)}^{n-\frac{1}{2}} - B_{y\left(i-\frac{1}{2},j,k+\frac{1}{2}\right)}^{n-\frac{1}{2}}}{\Delta x} - \frac{B_{x\left(i,j-\frac{1}{2},k+\frac{1}{2}\right)}^{n-\frac{1}{2}} - B_{x\left(i,j+\frac{1}{2},k-\frac{1}{2}\right)}^{n-\frac{1}{2}}}{\Delta y}\right) - j_{z\,(i,j,k+\frac{1}{2})} \quad \text{eq. 4.45}$$

Finally based on the speed of light in vacuum region and the time step of the simulation, the Courant-Friedrichs-Lewy condition is satisfied. A time step of $dt = 2 \times 10^{-14}$s and a grid size of $dx = dy = dz = 10^{-4}m$ and are adopted for this 3D model. Figure 4.5 shows the schematic of the coaxial cable used in our simulation with its boundary conditions highlighted and Figure 4.6 shows the cross section of the coaxial cable.

Boundary Conditions

Perfect Electric Conductor (PEC):

When the boundary at the surface of the simulation is a perfect conductor (metal, carbon etc.), the electric field parallel to that boundary is zero and therefore the electromagnetic waves are reflected off of this surface. Since the walls of the engine and neutralizer are made of conductor material, often the simulation surfaces follow the PEC boundary condition (Figure 4.5).

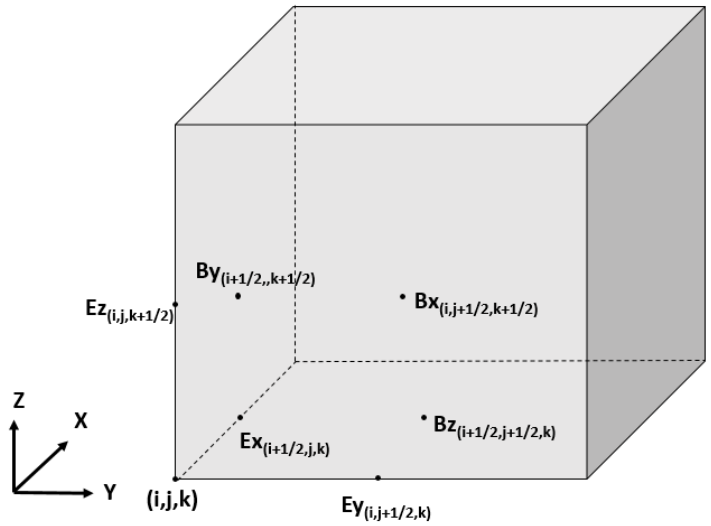

Figure 4.4: A 3D FDTD grid with field positions

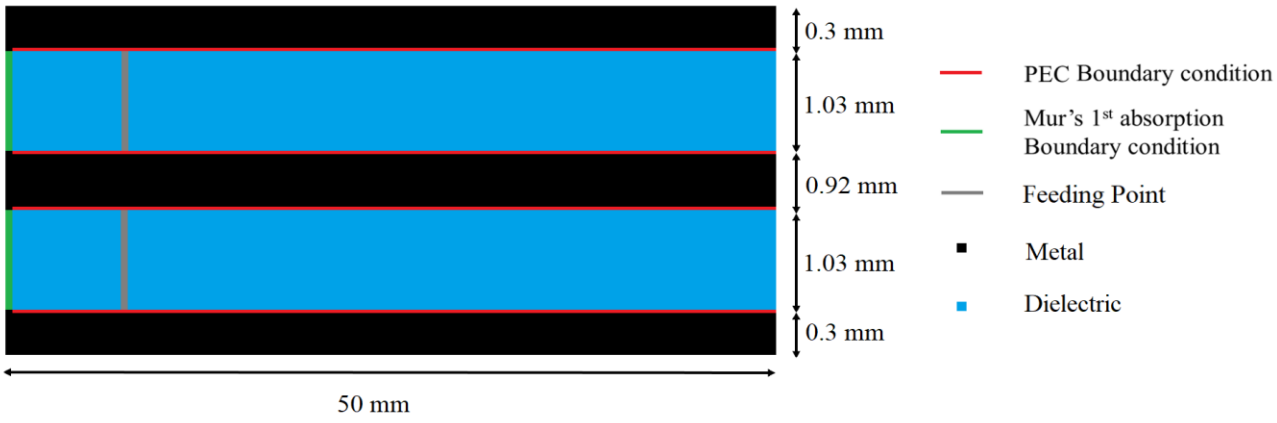

Figure. 4.5: Coaxial cable schematic with its boundary conditions

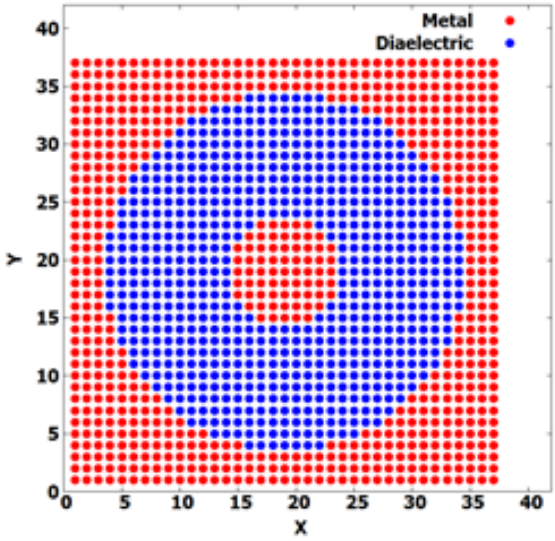

Figure. 4.6: Cross section of the cable's grid system

Mur's first order open boundary condition:

This boundary condition also known as open boundary is used when the electromagnetic waves are expected to be absorbed and not reflected back into the system. In our simulation, the base of the coaxial cable is considered to have an open boundary (Figure 4.5) where the electromagnetic waves are absorbed. This boundary for the first grids of the coaxial cable is set as:

$$E^{n}_{x(i,j,1)} = E^{n-1}_{x(i,j,2)} - C_{mur}\ (E^{n}_{x(i,j,2)} - E^{n-1}_{x(i,j,1)}) \quad \text{eq. 4.46}$$

$$E^{n}_{y(i,j,1)} = E^{n-1}_{y(i,j,2)} - C_{mur}\ (E^{n}_{y(i,j,2)} - E^{n-1}_{y(i,j,1)}) \quad \text{eq. 4.47}$$

Where C_{mur} is the constant defined as:

$$C_{mur} = \frac{v_{phase}\frac{\Delta t}{2} - \Delta z}{v_{phase}\frac{\Delta t}{2} + \Delta z} \quad \text{eq. 4.48}$$

Where v_{phase} is the speed of light in the dielectric material.

Microwave Input

The microwave input power in a coaxial cable is calculated by [67]:

$$\text{power} = \frac{2\pi}{\sqrt{\frac{\mu_0}{\varepsilon_0}}} v_{0b}^2 \ln\left(\frac{r_{outer}}{r_{inner}}\right) \quad \text{eq. 4.49}$$

where r_{outer} and r_{inner} are the outer and inner radius of the cable respectively and the v_{0b} is the voltage between the cable's inner and outer layers. In the simulation, an adjustable parameter is multiplied to this equation for adjusting the input power value. This parameter does not affect the accuracy of the simulation in any way and is just a numerical simulation method. Therefore input field values are calculated by:

$$B_\theta = v_{0b}\frac{1}{r}\frac{1}{c_D}\sin(\omega t - \emptyset) \quad \text{eq. 4.50}$$

$$E_r = v_{0b}\frac{1}{r}\sin(\omega t) \quad \text{eq. 4.51}$$

where C_D is the speed of light in the dielectric region and $\emptyset$ is the phase difference between the magnetic and electric fields. The field components E_r and B_θ should be implemented on the cables cross section (Figure 4.6) and should be divided into their xy components. In order to get the right $E \times B$ vector and the right values, therefore the following formulation is used:

$$E_{x(i,j,k)} = E_{x(i,j,k)} + E_{r(i,j)}\frac{x}{r} \quad \text{eq. 4.52}$$

$$E_{y(i,j,k)} = E_{y(i,j,k)} + E_{r(i,j)}\frac{y}{r} \quad \text{eq. 4.53}$$

$$B_{x(i,j,k)} = B_{x(i,j,k)} - B_{\theta(i,j)}\frac{y}{r} \quad \text{eq. 4.54}$$

$$B_{y(i,j,k)} = B_{y(i,j,k)} + B_{\theta(i,j)}\frac{x}{r} \quad \text{eq. 4.55}$$

Applying Equations 4.52 to 4.55 would lead to the electric and magnetic field vectors at the input positions indicated in Figures 4.7 and 4.8. The simulated waves are illustrated in Figures 4.9 through 4.14. The figures indicates results for five wave period taken at a mid-plane cross section of the cable where the y values are constant. Since the wave in this simulation is supposed to act as a TEM wave the E_z and $B_z$values are expected to be close to zero. As it can be seen in Figure 4.11 the comparative value of E_z with respect to the amplitude of E_x wave in Figure 4.9 is too insignificant (24000 times smaller) which means that it can be ignored. Same thing applies to the magnetic field values depicted in Figures 4.13 and 4.14. The B_z value is half a million times smaller than B_y which means it will not affect the accuracy of the simulation as well. Since this output data is taken at a plane in the center of the *y* axis, E_y and $B_x$values corresponding to E_θ and B_r, are also expected to be zero. However , since the simulated geometry of the cable is not a perfect cylinder we expect some imprecisions as well. According to Figures 4.10 and 4.13 since the amplitudes of E_y and B_x waves are four orders of magnitude smaller than their respective wave amplitudes, these imperfections can also be ignored as they will not cause any defects on the outcome of the simulation.

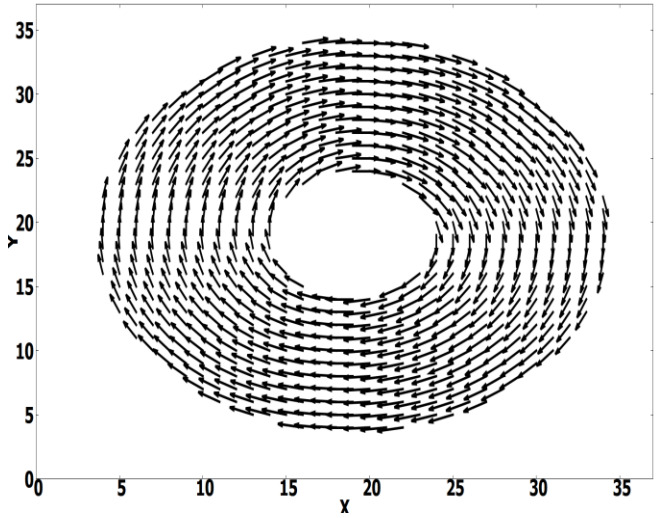

Figure. 4.7: Initial B_θ vectors at Microwave input plane

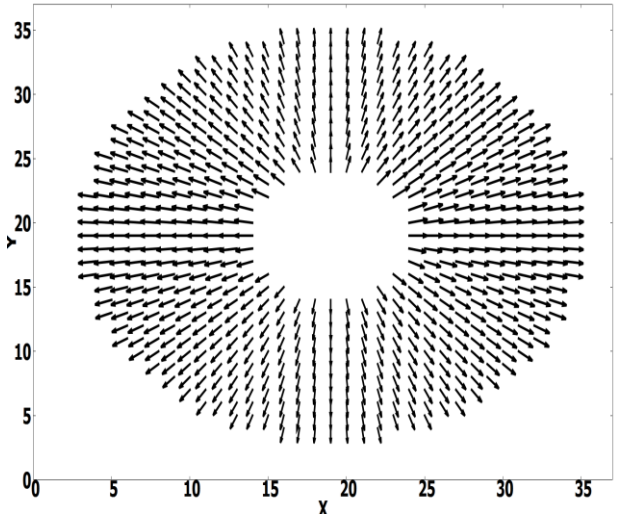

Figure. 4.8: Initial E_r vectors at Microwave input plane

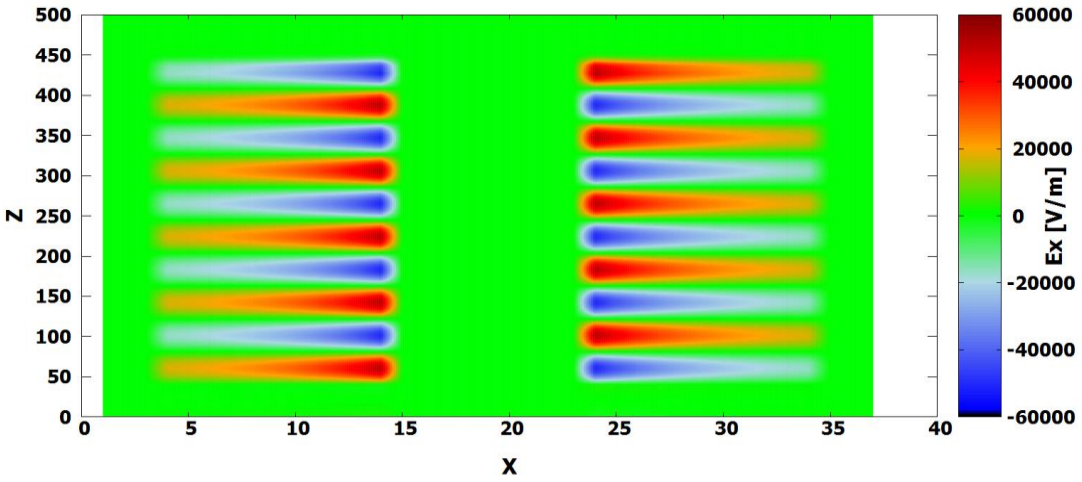

Figure. 4.9: E_x field values through the coaxial cable

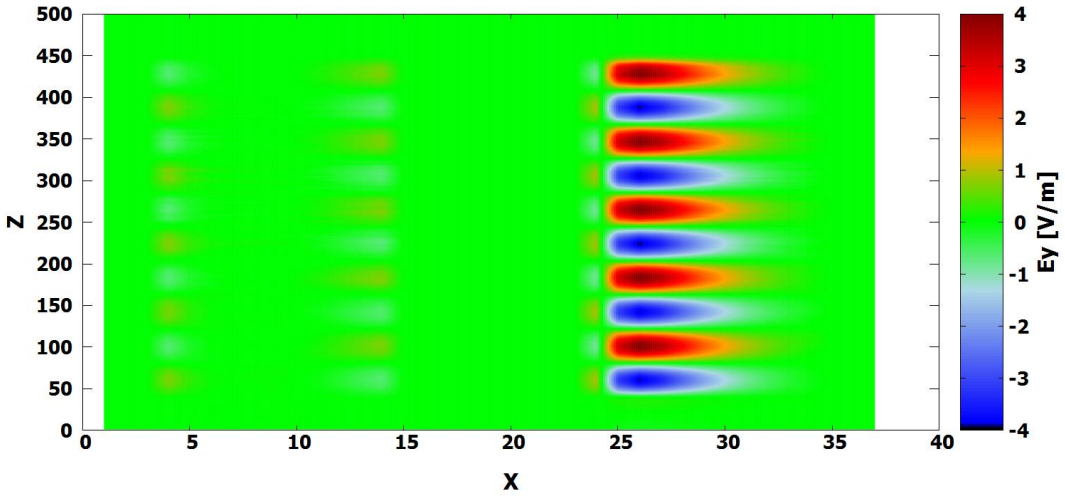

Figure. 4.10: E_y field values through the coaxial cable

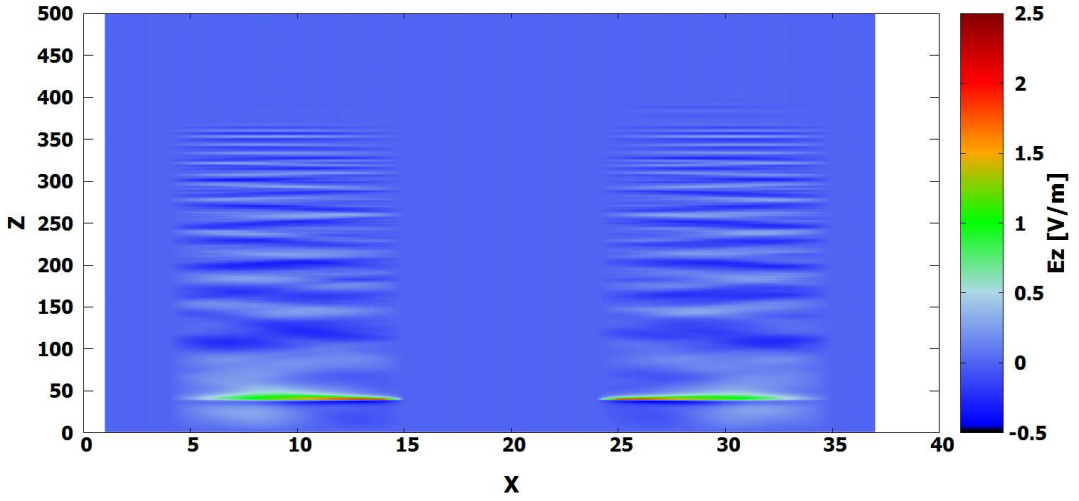

Figure. 4.11: E_z field values through the coaxial cable

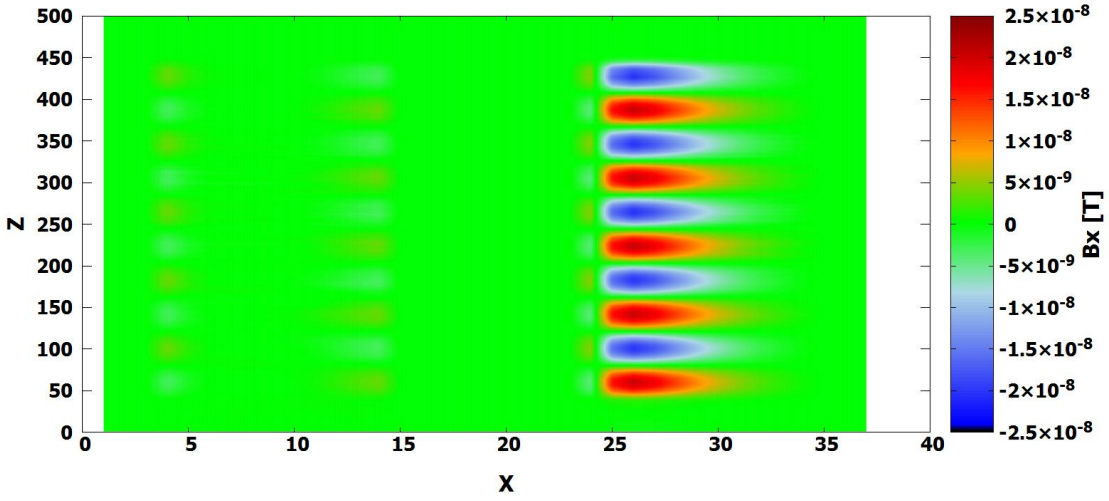

Figure. 4.12: B_x field values through the coaxial cable

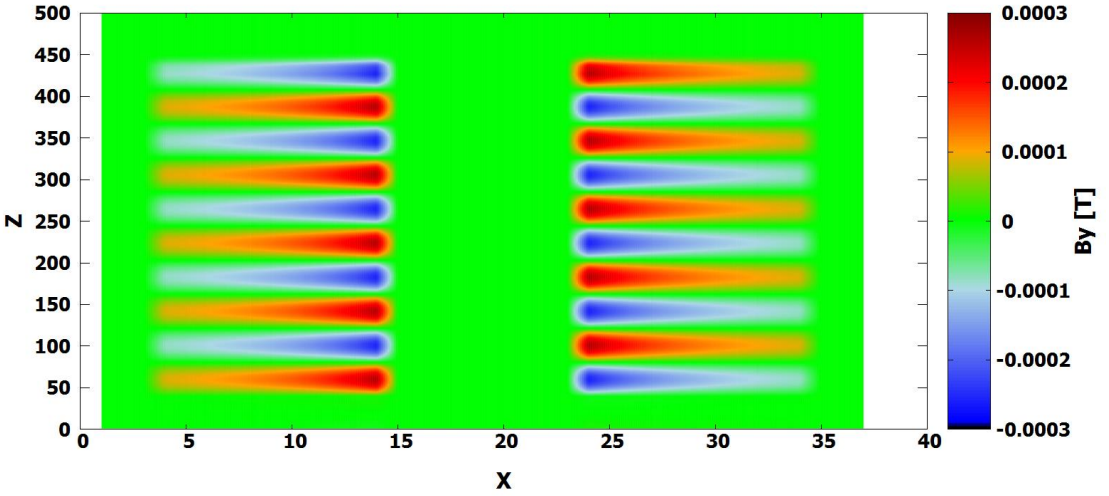

Figure. 4.13: B_y field values through the coaxial cable

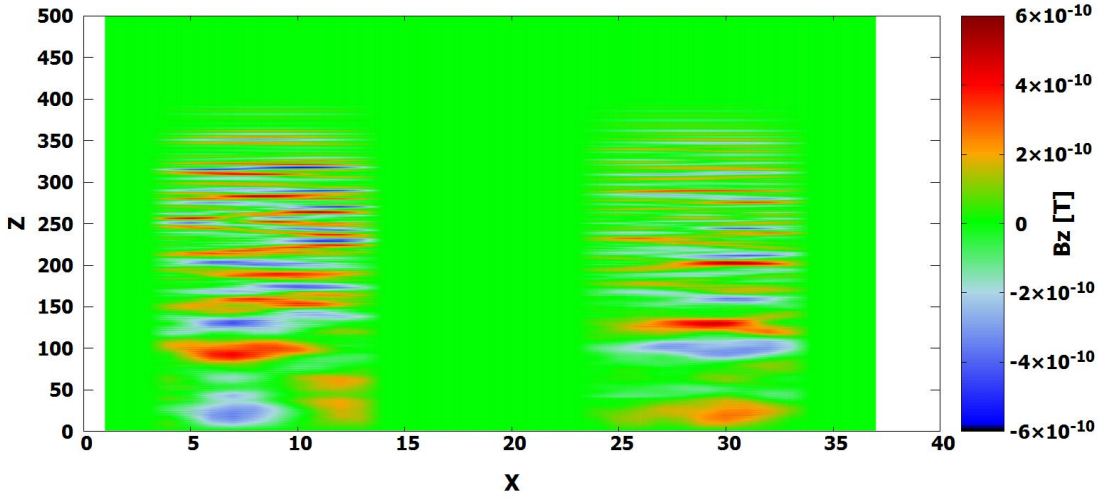

Figure. 4.14: B_z field values through the coaxial cable

Validation

In order to validate the results of the simulation, the power values are compared and inspected. To achieve that we will calculate the input power in two slices of the cable. One slightly ahead of the microwave input position (forward power) and one right before it (backward power). Equation 4.56 is used for calculating the input power.

$$\boldsymbol{P_{in}} = \frac{\mathbf{1}}{\boldsymbol{\mu_0}} \int_{\boldsymbol{A}} (\boldsymbol{E} \times \boldsymbol{B}) \cdot \boldsymbol{dA} \qquad \text{eq. 4.56}$$

By considering the input power in these two points, not only the power values can be checked but also the wave reflection can be seen as well. Since the input power was set to 10 Watts the input power fluctuations should be between 10 to minus 10 Watts as well. Furthermore we will calculate the output power which is the total power absorbed by the charged particles plus the total power of the field values at each grid point and due to conservation of energy law, the input and output power values must be identical at all times during the simulation. Since this power is the results of changes of the electromagnetic fields over time as a result of our input wave it is called the output power. The output power (field power) is calculated as follows:

$$\boldsymbol{P_{out}} = \int_{\boldsymbol{V}} [\boldsymbol{j}.\boldsymbol{E}] \boldsymbol{dV} + \frac{\boldsymbol{\partial}}{\boldsymbol{\partial t}} \int_{\boldsymbol{V}} \left[\frac{\mathbf{1}}{\mathbf{2}} \boldsymbol{\varepsilon E^2} + \frac{\mathbf{1}}{\mathbf{2}\boldsymbol{\mu}} \boldsymbol{B^2} \right] \boldsymbol{dV} \qquad \text{eq. 4.57}$$

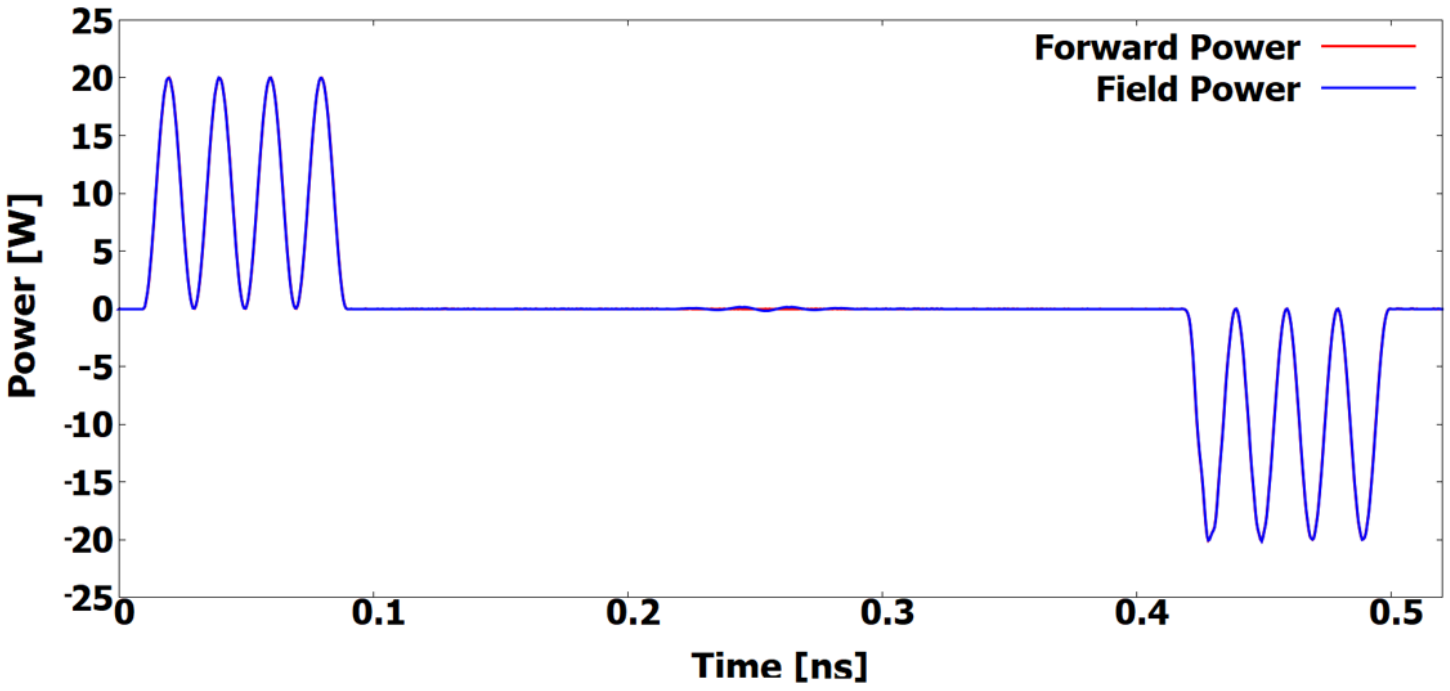

Figure. 4.15: Forward and Field power fluctuating values during simulation

Through comparing the input power at both forward and backward positions with the field power (output power) values throughout the cable, the validity of the code can be examined. In order to investigate the power values, the simulation will consider the propagation of only two waves through the cable and the power fluctuations will be studied. Figure 4.15 shows power input fluctuations at forward position plotted over output power fluctuations for the two waves. The first upward fluctuations show the incoming waves whereas the second downward variations indicates the reflected waves. It should be noted that the amplitude of these waves varies from 0 to 20 Watts. This is because in Equation 4.56 the value of $\boldsymbol{E} \times \boldsymbol{B}$ is used to calculate the input power which for similar propagation direction maintains the same sign. This also means that for the waves on the right side of the figures the power value will be opposite since the propagation direction is reversed due to reflection. It is obvious in this figure that the input and output power values are identical throughout the duration of simulation which validates the accuracy of the wave propagation.

Improvements over the previous methods

The conventional method used previously in our research group for FDTD simulation adopted had a contrasting microwave input method known as the four point method [31]. In this method instead of inputting the microwave field values on an entire plane (Figure 4.6), four symmetric points around the central conductor rod are picked and only electric field value is implemented. Also the central conductor is reduced to one grid only which reduces the accuracy of this method even further. In this method the rest of the cable is ignored and only the field values in these four points are calculated. Since we are considering the entire cable, we adjusted the four point input method for the entire input plane where the magnetic field input is also included. We compared the simulation results of this method with the previously discussed simulation using exactly the same conditions as shown in previous outlines. The simulation results of the four point method are depicted in Figures 4.16 to 4.21. A simple side by side comparison of these and Figures 4.9 to 4.14 will clarify the improvements of the currently used simulation method. The first thing that is noticeable is that the waves in four point method are propagating in both directions from the input point. This is due to the fact that in order to achieve the correct pointing vector, the electric and magnetic field values of an entire plane should be considered and not just electric field values. Furthermore, by comparing the E_z and B_z graphs it is clear that the amplitude for the E_z and B_z waves in the four point method are larger than their counter parts in the plane method. This large value will result in further obvious inaccuracies illustrated in these figures. Further field ratio comparisons (simulation error) of the both methods are discussed in Table 4.1. Keep in mind that smaller field ratios are an indication of a more accurate simulation. Another advantage of the plane method can be seen that in Figures 4.16 through 4.21 the waves are not symmetrical across the cable's cross section. This asymmetry would be resolved if the E_z and B_z values were manually set to zero. Another evident imprecision is in the E_y and B_x values which are corresponding to $\boldsymbol{E_\theta}$ and $\boldsymbol{B_r}$, that are supposed to be at least close to zero. It is clear in Figures 4.17 and 4.19 that the amplitude value of these two waves is considerably large in contrast to the new method. This large value is also caused by the E_z and B_z field values since manually setting them to zero will also resolve this issue as well. And finally the amplitude in the E_x and B_y graphs which are

corresponding to $\boldsymbol{E_r}$ and $\boldsymbol{B_\theta}$, is half of what we expect in comparison to the new method. This is due to the fact that in four point method only the electric field are introduced and therefore the $\boldsymbol{E} \times \boldsymbol{B}$ vector is incorrect. This means that the wave in the conventional method propagates in both directions which leads to half the power being directed in the wrong course. This results in only half the power being propagated in the right direction. These inaccuracies does not occur in the plane method which leads to a more accurate microwave simulation.

Table. 4.1: Field ratios (simulation error) evaluation for different input methods

Ratios / Methods	$\frac{E_\theta}{E_r}$	$\frac{B_r}{B_\theta}$	$\frac{E_z}{E_r}$	$\frac{B_z}{B_\theta}$
Plane	0.00006	0.00083	0.00004	0.000002
4-point	0.0667	0.0667	0.00067	0.000267

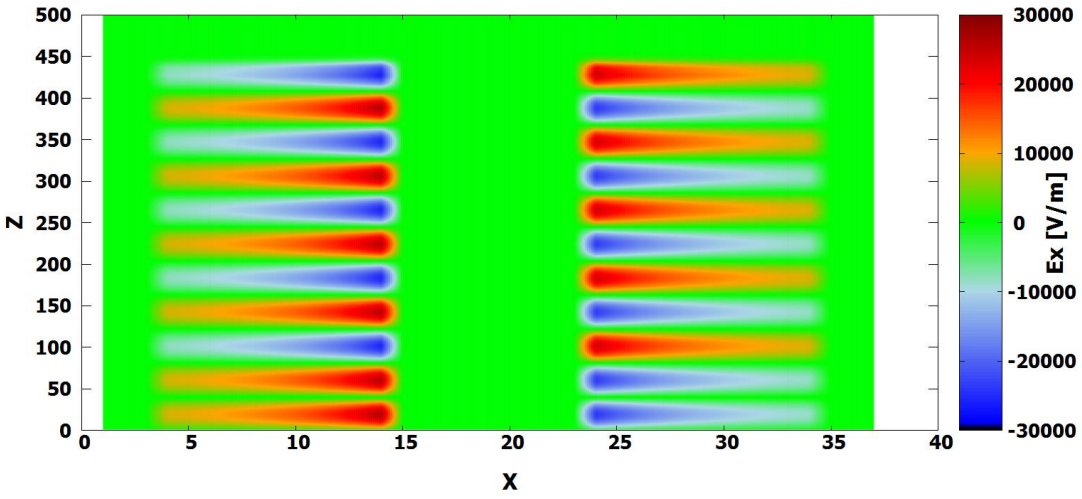

Figure. 4.16: E_x field values through the coaxial cable in four point method

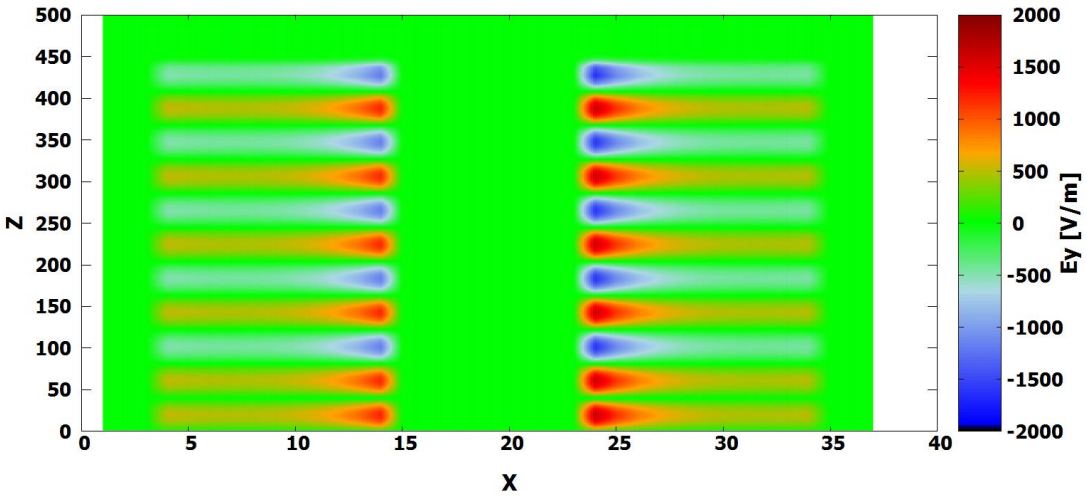

Figure. 4.17: E_y field values through the coaxial cable in four point method

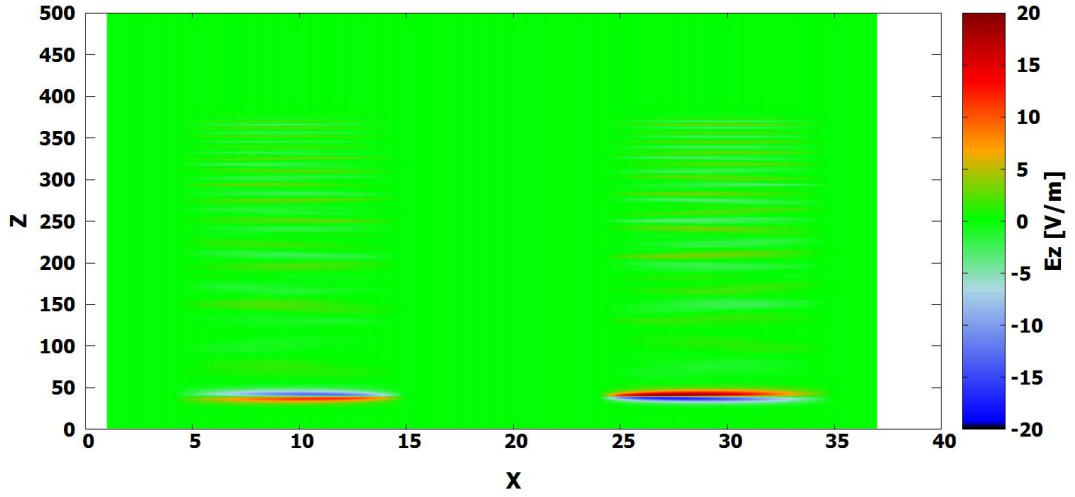

Figure. 4.18: E_z field values through the coaxial cable in four point method

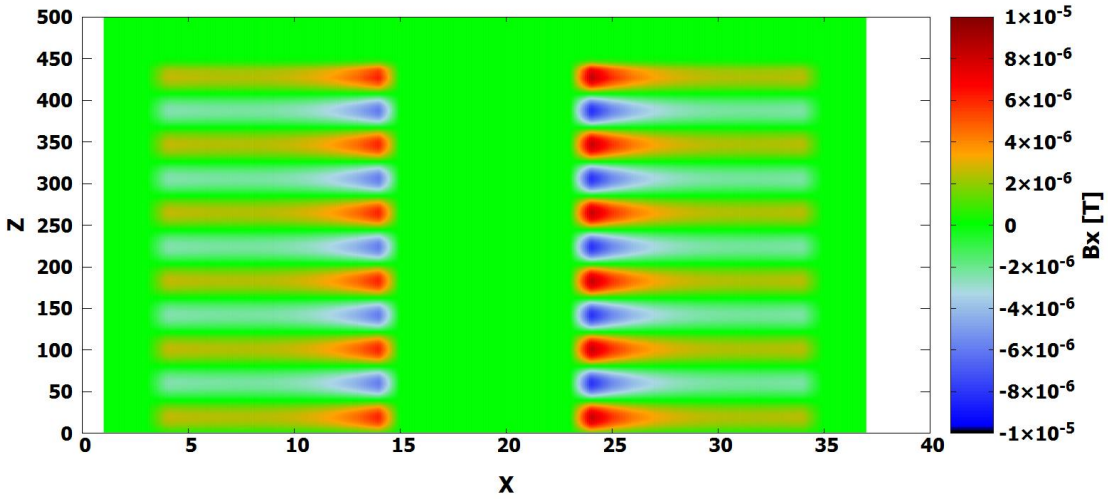

Figure. 4.19: B_x field values through the coaxial cable in four point method

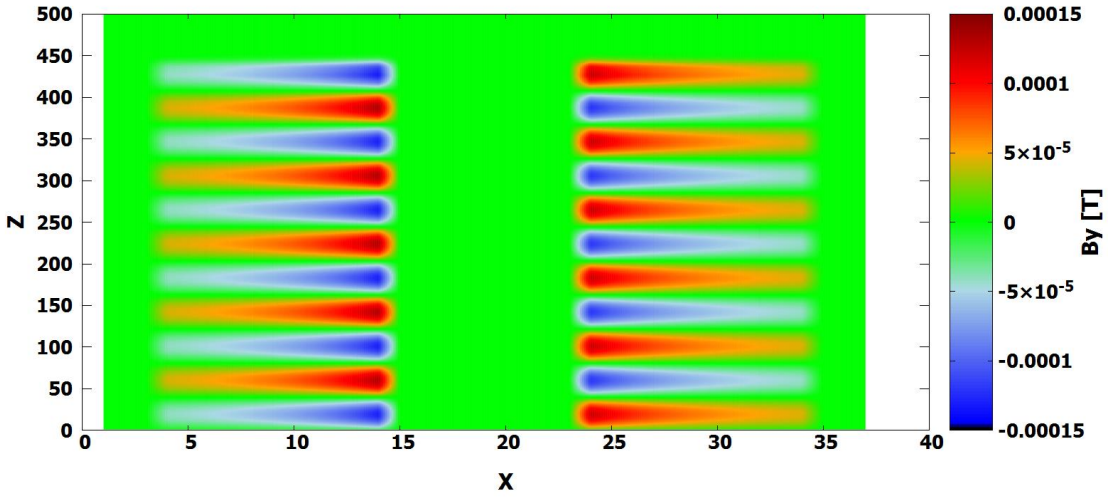

Figure. 4.20: B_y field values through the coaxial cable in four point method

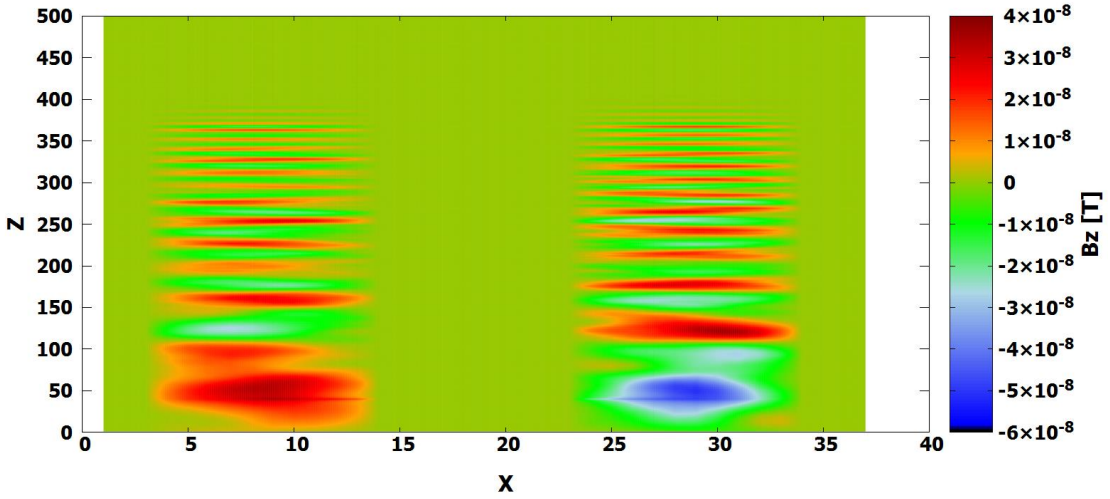

Figure. 4.21: B_z field values through the coaxial cable in four point method

4.1.4 Poisson Solver

While the coupled PIC-FDTD code deals with the propagation of electromagnetic waves as well as their impact on charged particles trajectory, collisions and overall behavior, it does not account for overall buildup of errors that occur in the code. This could affect the behavior of simulated particles as well as the accuracy of the code itself. Solving the Piosson equation for a system of particles corrects this blind spot and corrects the field values in a coupled PIC-FDTD code as well as rectifying the initial conditions of the simulation. The Piosson equation is solved using the ions and electrons densities in the simulation and the electric field is adjusted for the electron particles behavior.

The following is the super relaxation method of solving the Poisson equation for the three dimensional system of charged particles:

Considering the Poisson equation

$$\boldsymbol{\nabla . E} = \frac{\boldsymbol{\rho}}{\boldsymbol{\varepsilon_0}} = -\boldsymbol{\nabla}\emptyset^{\boldsymbol{2}} \qquad \text{eq. 4.58}$$

Where $\boldsymbol{\rho}$ is the difference between electron and ion number density, Adjusting and updating the electric field values after solving the equation would lead to:

$$\boldsymbol{E} = \acute{\boldsymbol{E}} - \boldsymbol{\nabla}\emptyset \qquad \text{eq. 4.59}$$

In a simulation setting the potential in each cell needs to be calculated and adjusted until the system reaches a steady state of $\frac{\partial \emptyset}{\partial t} = \mathbf{0}$
Therefore solving the equation would look like:

$$\frac{\emptyset_{i,j,k}^{n+1} - \emptyset_{i,j,k}^{n}}{\Delta t} = \frac{\emptyset_{i+1,j,k} - 2\emptyset_{i,j,k} + \emptyset_{i-1,j,k}}{\Delta x^2} + \frac{\emptyset_{i,j+1,k} - 2\emptyset_{i,j,k} + \emptyset_{i,j-1,k}}{\Delta y^2} + \frac{\emptyset_{i,j,k+1} - 2\emptyset_{i,j,k} + \emptyset_{i,j,k-1}}{\Delta z^2} + \frac{\rho_{i,j,k}}{\varepsilon_0} \qquad \text{eq. 4.60}$$

Utilizing the maximum Courant condition where $\Delta t = \frac{1}{6}\Delta x^2$ and $\Delta x = \Delta y = \Delta z$

$$\emptyset_{i,j,k}^{n+1} = \emptyset_{i,j,k}^{n} + \frac{1}{6}\left(\emptyset_{i+1,j,k}^{n} + \emptyset_{i-1,j,k}^{n} + \emptyset_{i,j+1,k}^{n} + \emptyset_{i,j-1,k}^{n} + \emptyset_{i,j,k+1}^{n} + \emptyset_{i,j,k-1}^{n} - 6\emptyset_{i,j,k}^{n}\right) + \frac{1}{6}\Delta x^2 \frac{\rho_{i,j,k}}{\varepsilon_0} \qquad \text{eq. 4.61}$$

Where it can be simplified in to:

$$\emptyset_{i,j,k}^{n+1} = \emptyset_{i,j,k}^{n} + a \qquad \text{eq. 4.62}$$

Where a is the calculation error. The code will iterate and solve this equation for the entire simulation system until the r value becomes close to zero. After which the electric field values for each grid can be updated to the corrected. It should be noted that in our simulation it is not practical and not necessary to solve this equation at every time step therefore in our current simulation the Poisson equation is solved at every 1000 time steps and the field values are updated for ions only.

It should be mentioned that our coupled simulation code differs slightly from a conventional PIC code. As mentioned earlier, the electrons in the simulation are impacted by the ambient magnetic field as well as the electromagnetic propagation. This leads to electrons following equation 4.1 as their equation of motion. Furthermore, the FDTD part of the simulation will handle the electrons particle movement, field calculation and weighing, collision probability calculation as well as solving the Poisson equation by importing the ion and neutral densities from the PIC segment of the simulation. In the meantime, the ions are only impacted by the ambient magnetic field, meaning that they follow equation 4.1 as well without the electric field part. As mentioned earlier the electrostatic fields are not considered for the current work. Finally the neutrals follow an equation of motion similar to that mentioned in chapter 2. With this in mind, the PIC segment of the code handles the ion and neutral interactions by receiving the collision information from the FDTD segment and updating the particles trajectory accordingly. Considering the simulation methods mentioned in this chapter the overall and simplified flowchart of the simulation is shown in Figure 4.22. It is clear that the coupling of these methods together will lead to a more comprehensive simulation of particles where each method complements the other.

4.2 Simulation Properties

Table 4.2 and 4.3 indicates the plasma and simulation parameters used for this code. The initial conditions assumed for the particles are based on our experimental data [24]. In this simulation, the neutral particles are inputted through the inlet at the designated mass flow rate. After the neutrals reach a steady state (that is when the number of neutral super particles entering the engine equals to the number of neutral super particles leaving taking a real-time of around 30 ms) then electron super particles are inputted in every simulation cell (excluding the inlet) based on the initial parameters indicated in table 4.3. In this stage the FDTD and PIC coupling begins where for every 1 PIC iteration, 50 FDTD iterations occur. This is a common theme in FDTD-PIC simulation due to the speed difference between the electron and electromagnetic wave and the heavier ion particles. The Poisson solver is also applied to the FDTD segment at every 1000 FDTD time steps while the PIC code handles the ion and neutral behavior at every 50 time steps. In this stage the simulation runs to the limit of our current supercomputer which leads to a simulation real-time of 10 ns after the neutral steady state. It should be noted that in our current simulation, ions are not included in the FDTD segment. This means that the FDTD code only recognized electron current density and not that of ions. This is due to the fact that electrons move at higher speed than heavy xenon ions that we can consider ions as relatively stationary in comparison.

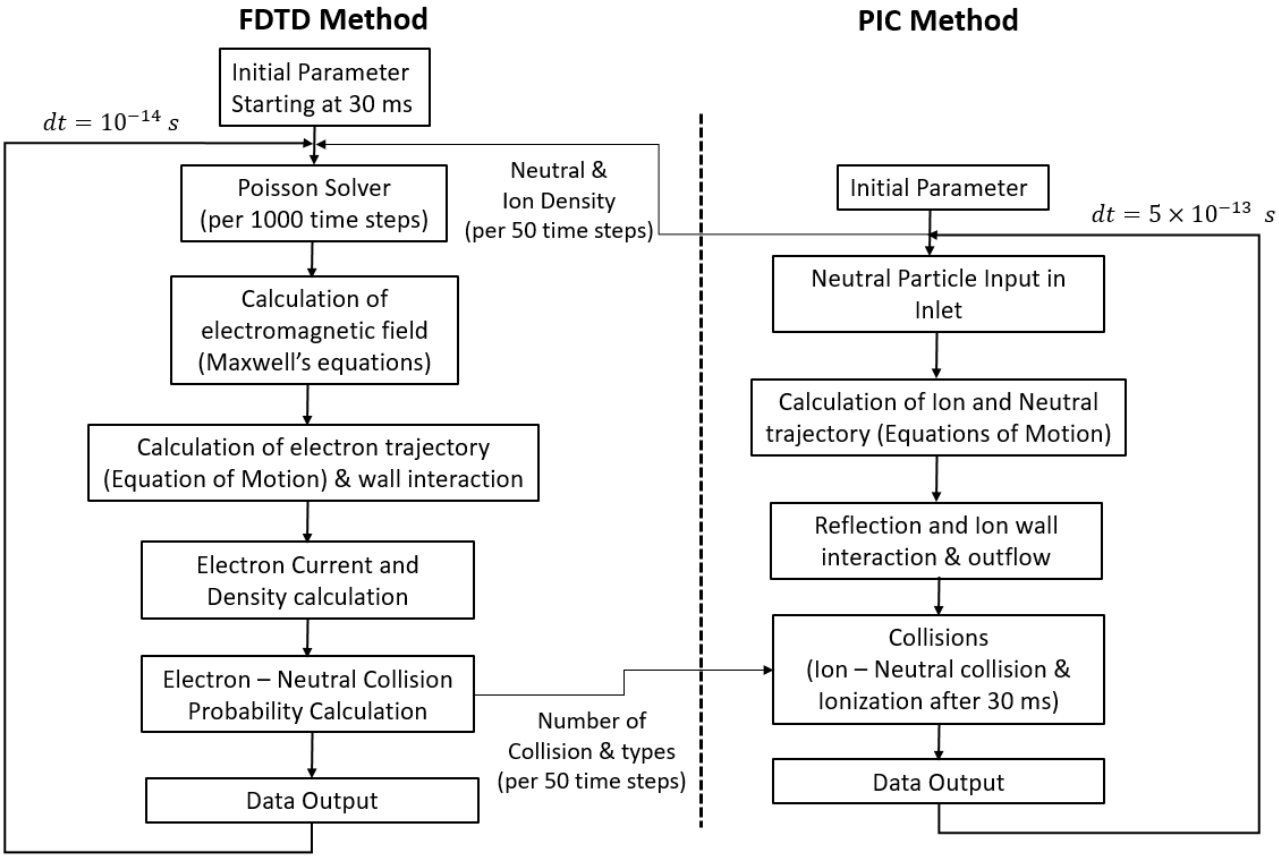

Figure. 4.22: Flowchart of the coupled FDTD-PIC

Table. 4.2: Plasma properties

Initial electron density (m^{-3})	10^{18}
Initial electron Temperature (eV)	2
Debye Length (m)	1.05×10^{-5}
Plasma Frequency (s^{-1})	8.9×10^{9}
Electron Cyclotron Frequency (s^{-1})	3.4×10^{9}
Plasma to Cyclotron Frequency ratio	2.61
Electron Larmor Radius near Antenna (m)	6.15×10^{-5}
Ion Larmor Radius near Antenna (m)	8.7×10^{-3}
Courant Condition Limit	1.9×10^{-14}

Table. 4.3: FDTD-PIC simulation properties

Propellant	Xe
Mesh size (m)	10^{-4}
Neutral Mass Flow Rate ($mg.s^{-1}$)	10^{-2}
Microwave Frequency (GHz)	2.4
Incident Power (W)	8
Number of Sm-Co Magnets	12
Electron Super Particle	5×10^{3}
Electron Super Particle per Cell	200
Neutral Super Particle	10^{6}
Ion Super Particle	10^{5}
Ion/Electron mass ratio	480
FDTD Time Step (s)	10^{-14}
PIC Time Step (s)	5×10^{-13}
Knudsen Number	1.2

It can be seen that the mesh size for this simulation is very small. Often the simulations developed in our research group use a larger mesh size within the range of 0.25 to 0.5 mm [30-31]. This is mainly due to the calculation cost of using a finer mesh. Our current work however has managed to push this limit and achieve a finer mesh size of 0.1 mm through recent improvements in our computational machines as well as utilizing several parallelization methods to reduce the calculation cost. We use a hybrid parallelization method of OpenMP-MPI (Message Passing Interface) in which both the particles and simulation space are divided into 144 independent paralleled calculating segments each in constant communication with each other.

Finally, as seen in table 4.2, the Debye length of the plasma in our simulation is much smaller than our current mesh size. This is in clear contrast to the constraint in equation 4.2. The Debye length of our plasma is 10^{-5} m which is 10 times smaller than our current mesh size. This means, in order to accurately simulate the plasma sheath, we need to have a mesh that is at least 20 times smaller than the current 0.1 mm size. As mentioned above, our current work is already pushing our super computer to its limit and therefore adopting a considerably smaller mesh size is impossible due to the limits of our current super computers. This will have implications in terms of the plasma sheath simulation accuracy. While other researchers in this field might apply an artificial sheath condition at the walls based on experimental data (often a sheath of 20 eV for Xe) [30-31], we aim to examine and elaborate the possibility of using a simulation with a less than ideal sheath voltage that matches our current calculation limits. Although the sheath voltage in the simulation will not be as accurate as we hope, the difference should not exceed 3 times and as far as a comparative study such as ours is concerned, it should lead to some preliminary results that can be improved upon in the near future.

Other simulation properties such as time step are in perfect agreement with the required constraints elaborated in the previous segments.

4.2.1 Boundary Condition

FDTD Boundary Condition:

As mentioned in section 4.1.3, the entire surfaces of the engine (apart from the dielectric) are assumed to comply with the perfect electric conductance conditions and are considered to have a closed boundary condition. The base of the dielectric region of the coaxial cable in the simulation geometry however (Figure 4.5), is assumed to have an open boundary condition following Mur`s first order open boundary. Finally, since the grid hole for this engine are incredibly small (1.2 mm φ) relative to the microwave wave length, they are assumed to be reflective as well.

PIC Boundary Condition:

While neutrals are not affected by the simulation sheath, they are scattered off from the walls of the simulations when they come in contact with it and they are removed from the simulation once they reach a grid hole. Electron particles on the other hand, will be removed from the simulation given that they reach a potential greater than simulation sheath potential when they come in contact with the simulation wall, otherwise they are also scattered off. Similar condition applies to ion particles as well, however if an ion manages to get past the sheath, they are converted into a neutral and therefore the neutral recycle phenomena will occur. This simulation will focus on this phenomena and a comparative study of the neutral recycle rate for different inlet configuration will be achieved.

4.2.2 Antenna Configuration

In order to fully analyze the impact of inlet configuration and the resultant neutral density distribution on ion loss to the walls as well as ion density, two distinct antenna shapes were chosen for our current study. As discussed in chapter 2, different inlets configurations might benefit unique antenna shaped depending on the symmetry of the antenna. With that in mind we considered an asymmetrical L shaped antenna (identical to that shown in Figure 2.3) and a symmetrical disk shaped antenna as depicted bellow.

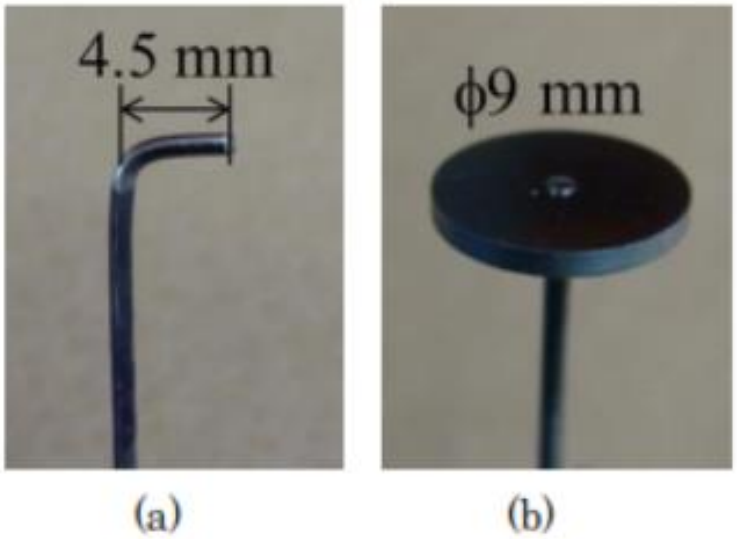

Figure. 4.23: Antennas used for this simulation, (a). L shaped antenna, (b). Disk shaped antenna

4.2.3 Inlet Configuration

In order to achieve a unique neutral particle distribution within the ion thruster, we have considered 4 different Inlet layouts to simulate which are as follows:

- **Bottom inlet:** currently used inlet position located right below the L shape of the antenna in the shape of a 2 mm square with a depth of 10 mm
- **4 small inlets:** consists of 4 small inlets distributed evenly at the bottom of the discharge chamber each in the shape of a 1 mm square with 10 mm depth.
- **4 horizontal inlets:** consists of 4 horizontal inlets at antenna height each in the shape of a 1 mm square with 10 mm depth
- **1 horizontal inlet:** consists of 1 horizontal inlet facing the L shape of the antenna in the shape of a 2 mm square with 10 mm depth

4.3 Simulation Results for an L shaped antenna

Figure 4.24 indicates the simulation geometry for the L shaped antenna engine with the conventional bottom inlet right below the antenna. While the position of the inlet is subject to change for other cases, the remainder of the simulation geometry is identical between inlet cases.

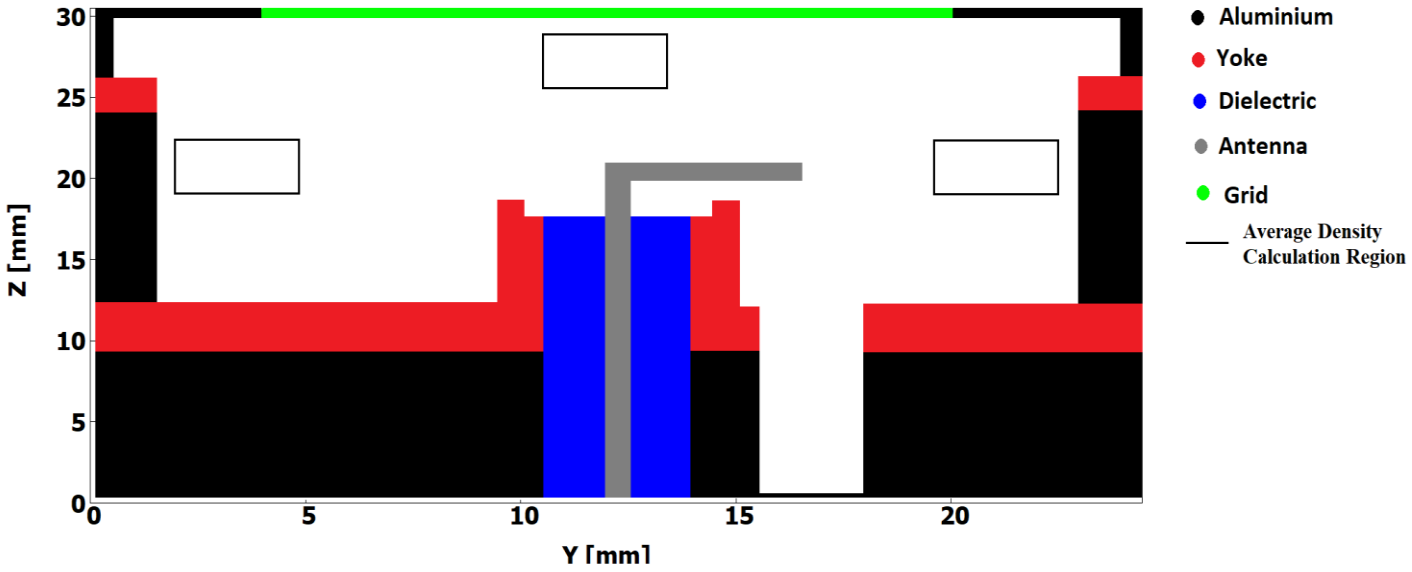

Figure. 4.24: Y-Z Cross section the L shaped antenna thruster taken at X = 12 mm (middle of the simulation geometry) for the conventional bottom inlet with selected average density calculation regions

All the simulation results are taken at the end of the simulation run at the real time of 30ms + 10 ns. Figures 4.25 through 4.28 show the neutral density distribution for each inlet case. The Y-Z plane results are taken at mid-engine (X = 12 mm) while the X-Y data is extracted from the antenna height. It is evident from the figures that the inlet configuration plays a key role in neutral density distribution since the density pattern follows the inlet position in each case. While the single bottom inlet configuration leads to a one sided distribution facing the antenna, the four bottom inlets lead to a more uniformly distribution density within the engine. Similar pattern is observed for the horizontal inlets where the single horizontal inlet leads to the highest neutral density concentration around the antenna than any other inlet case while the four horizontal inlet cases balance out the neutral density distribution throughout the discharge chamber. It should be noted that the average neutral density for the ion thruster in this simulation is significantly lower than the average neutral density obtained for the neutralizer in chapter 2 and 3. This is due to two reasons. Firstly the lower mass flowrate for the ion thruster in this simulation (0.01 $mg.s^{-1}$) in contrast to the mass flowrate of 0.049 $mg.s^{-1}$ and finally the design difference between the two devices. While the neutralizer utilizes an orifice design which will keep more particles in its discharge chamber, the ion thruster is equipped with a grid system which will allow for more particles to leave the engine hence the lower average neutral particle density in the ion thruster. Moreover the neutral density obtained here seems more uniformly distributed than the one obtained in chapter 2. This is due to fact that the density obtained for neutralizer in chapter 2 is averaged over a shorter period of time leading to a less uniform looking graph whereas the data obtained for the ion thruster here is averaged over a longer period of time. Another possibility could be the impact of electron density distribution that might lead to the lower neutral density within the ion thruster. This however is unlikely to be the case as it can be seen in Figure 3.3, where the impact of electron density and ionization on neutral density is clearly observed. In this figure, which is for a uniform electron density with a temperature of 6eV (assumed in this simulation which would lead to a higher overall ionization rate than the more realistic ionization rate obtained in chapter 4) we can still see that the ionization only changes the neutral density by 3-4% . this will not be enough to explain the lower neutral density in the ion thruster.

Figures 4.29 to 4.34 indicate the average rate of ionizing collisions that occur within the discharge chamber. Similar to the previous graphs, they are taken at the Y-Z plane in the middle of the simulation geometry since that offers an adequate view from which the ionization rate of the entire simulation region can be deduced. The ionizing collision rate is averaged over the simulation run time and normalized over space and time. It is evident that the majority of the ionizing collisions occurs around the antenna with the highest rate being at the tip of the antenna which is expected. The ionizing collision pattern almost mirrors the electron distribution pattern with the highest collision rates occurring in the high temperature regions. Figure 4.29 indicates the average ionizing collision rate for the bottom inlet configuration. In order to see the impact of inlet positioning on ionizing collisions, we should focus on the lower collision rate regions (blue regions) rather than the high collision rate region around the antenna. Of courses the antenna plays the major role in determining the electron density and ionizing collision rate consequently,

the focus of our study is the impact of neutral density distribution on ionizing collision rate as a result of inlet positioning. While the differences between the antenna side of the discharge chamber versus the non-antenna side are subtle in the low collision rate regions, the antenna side appears to lead to a higher probability of ionizing collision occurring. This could still be due to the shape and positioning of antenna and not the inlet and therefore we must compare other inlet cases. Comparing the low collision rate regions of Figure 4.29 versus Figure 4.30 shows the impact of inlet positioning clearly.

This can be seen the antenna side of the discharge chamber where in the four bottom inlets, there is a slightly lower rate of ionizing collisions occurring than in the single bottom inlets. This could be due to the fact that the single bottom inlet leads to a higher density of neutrals near the antenna side walls (Figure 4.25) which in turn increase the probably of ionizing collision. A similar pattern can be seen by comparing the two horizontal inlets in Figures 4.30 and 4.31 where the single horizontal inlet leads to a higher rate of ionizing collisions near walls of the antenna side of the discharge chamber while the four horizontal inlets leads to a more balanced collision rate between the two sides. Finally all inlets considered, the neutral density distribution only seems to alter the ionizing collision rate in the lower probability regions (i.e. near the walls and far from the antenna) rather than the regions surrounding the antenna. One explanation could be that the high ionizing collision regions have sufficient minimal neutral density to collide with and ionize while having plenty of high energy electrons. This way the small changes in the neutral density will not show a clear difference in the ionizing rate. On the other hand, the regions with fewer high energy electrons could see an increase in the probability of ionizing collisions by increasing the neutral density rate.

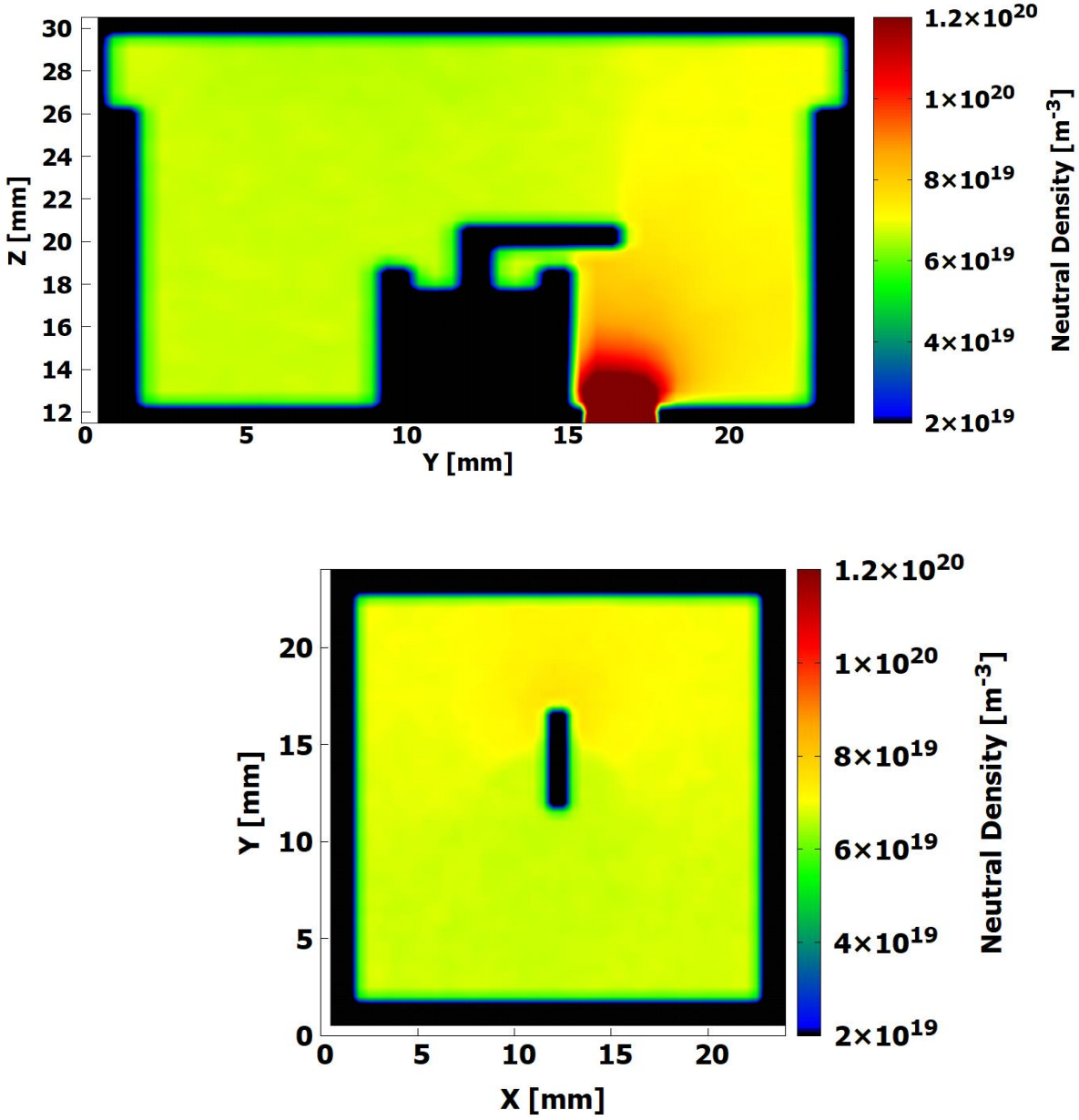

Figure. 4.25: Neutral density distribution for the bottom inlet configuration: (top) Y-Z plane and (bottom) X-Y plane.

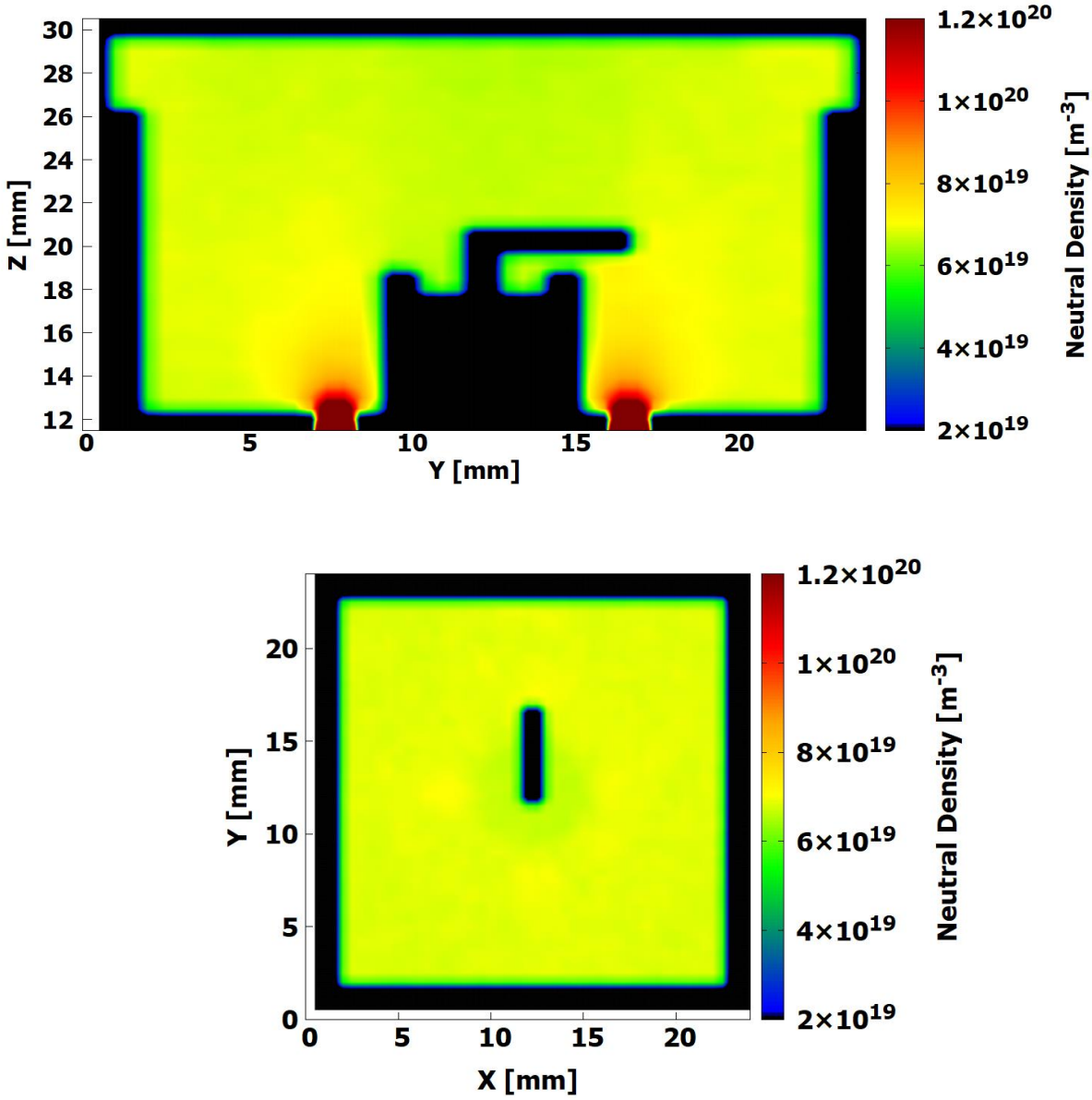

Figure. 4.26: Neutral density distribution for the four bottom inlet configuration: (top) Y-Z plane and (bottom) X-Y plane.

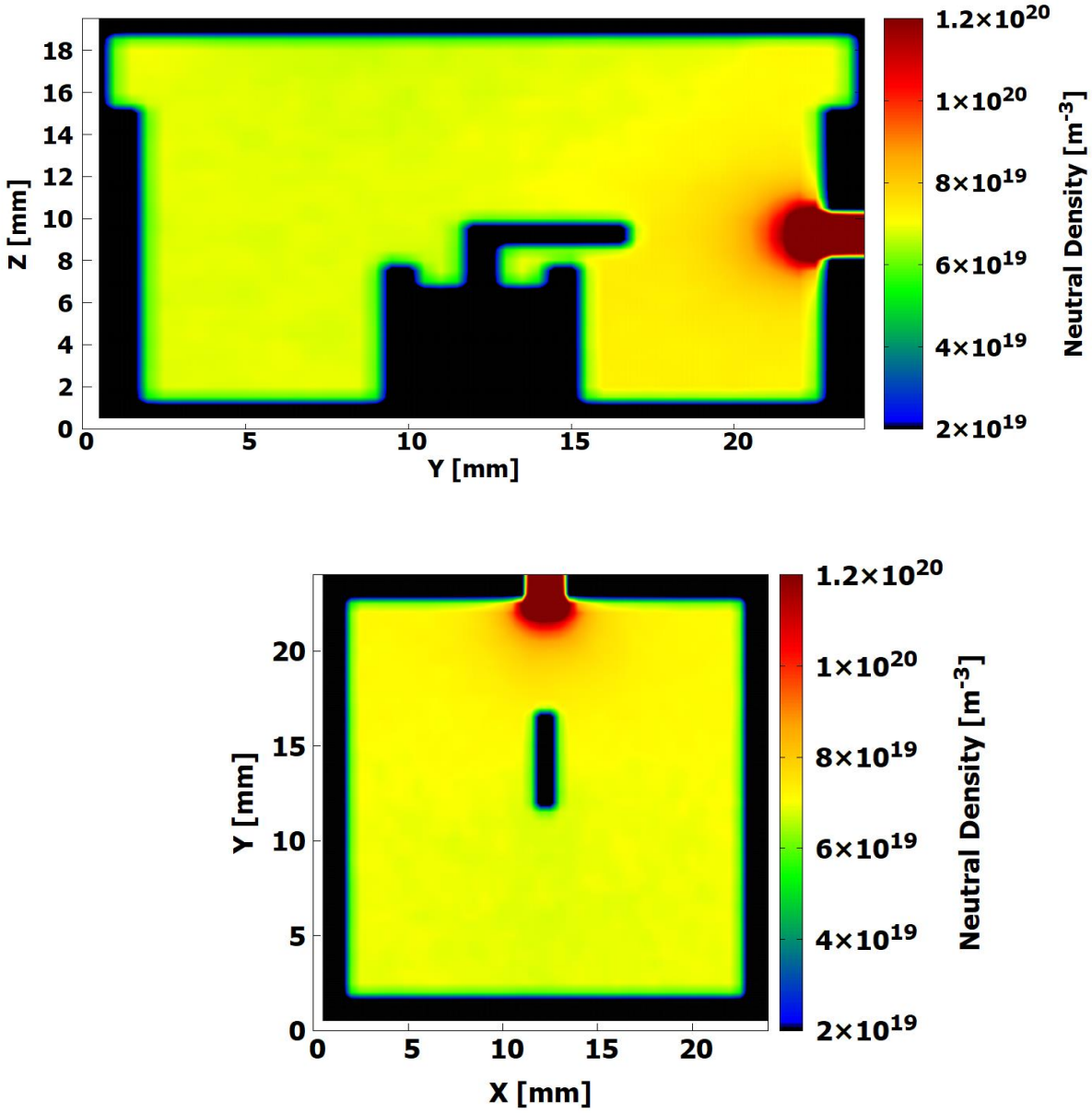

Figure. 4.27: Neutral density distribution for the horizontal inlet configuration: (top) Y-Z plane and (bottom) X-Y plane.

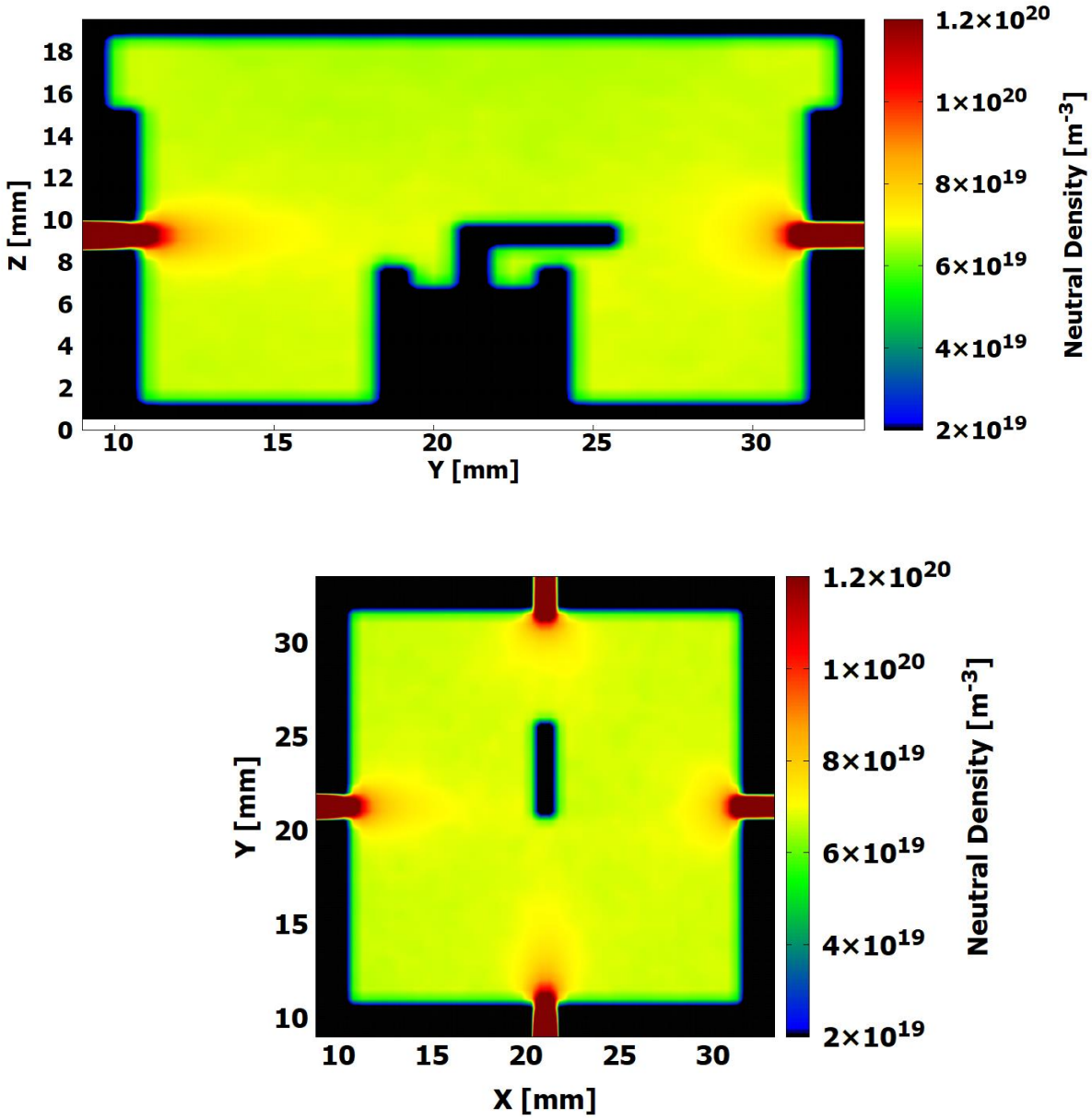

Figure. 4.28: Neutral density distribution for the four horizontal inlet configuration: (top) Y-Z plane and (bottom) X-Y plane.

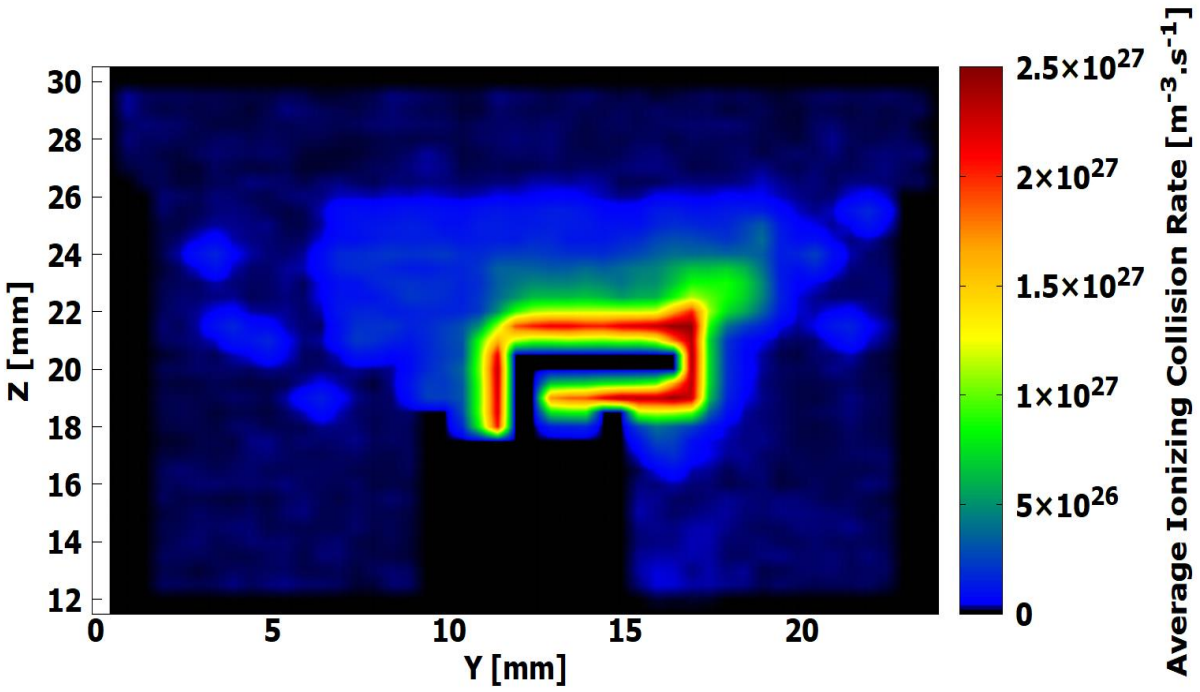

Figure. 4.29: Average Ionizing Collision Rate for the bottom inlet configuration

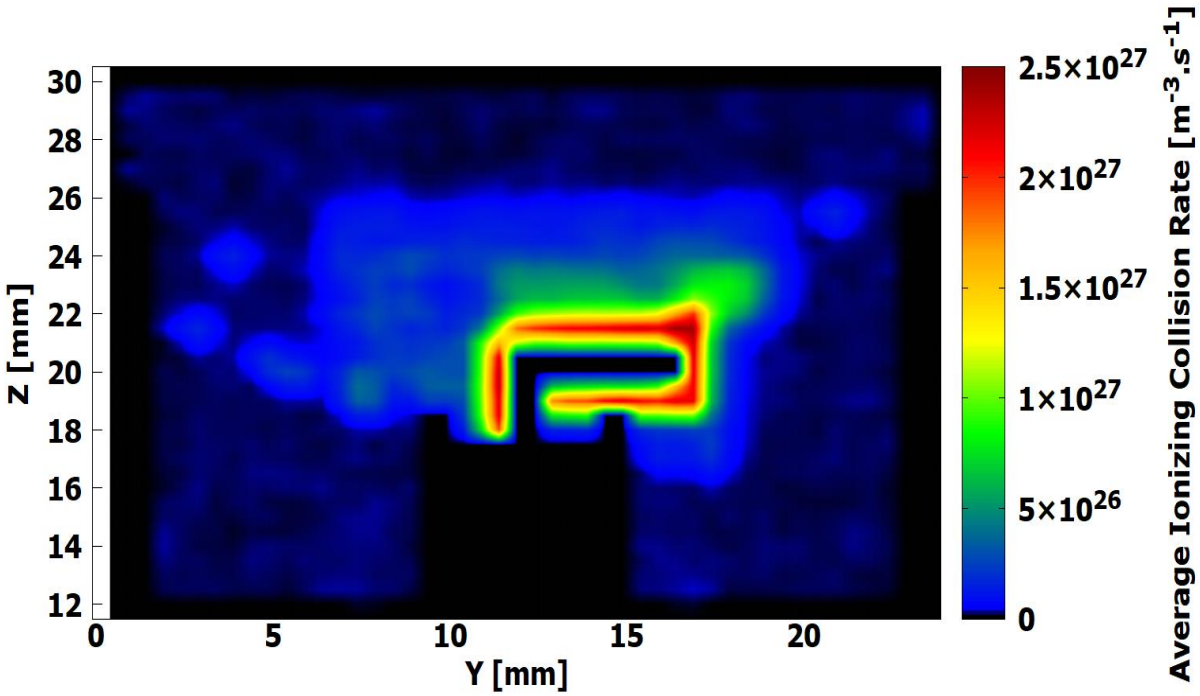

Figure. 4.30: Average Ionizing Collision Rate for the four bottom inlets configuration

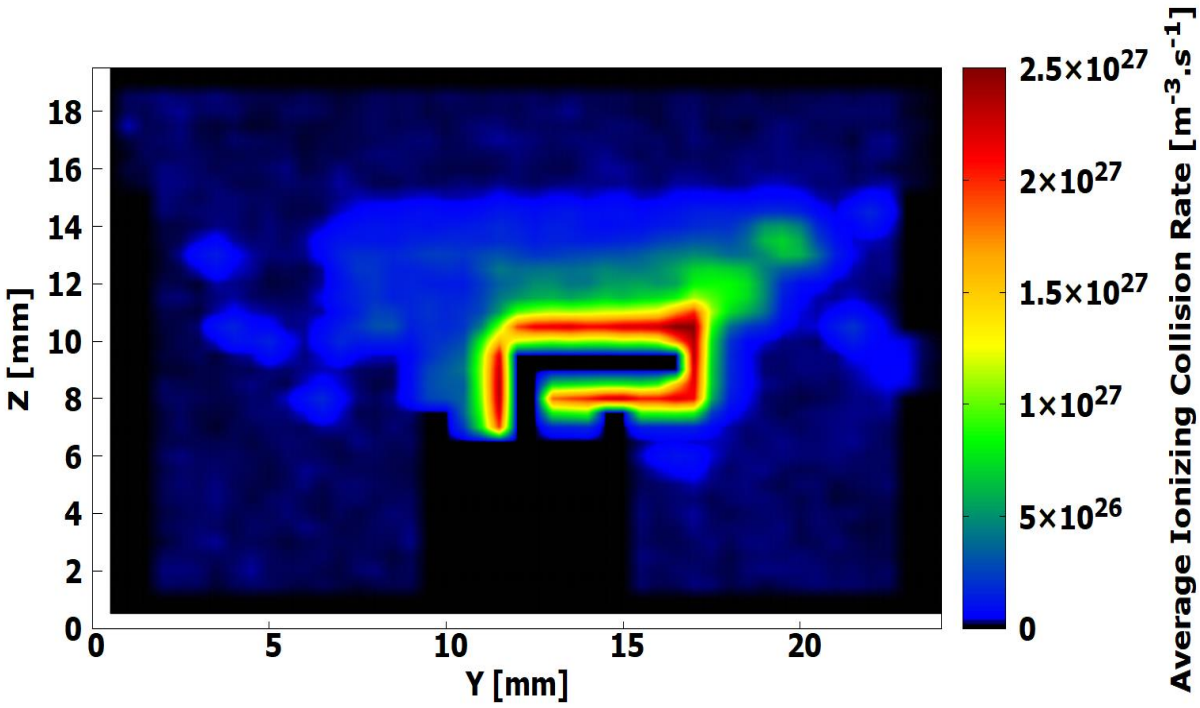

Figure. 4.31: Average Ionizing Collision Rate for the horizontal inlet configuration

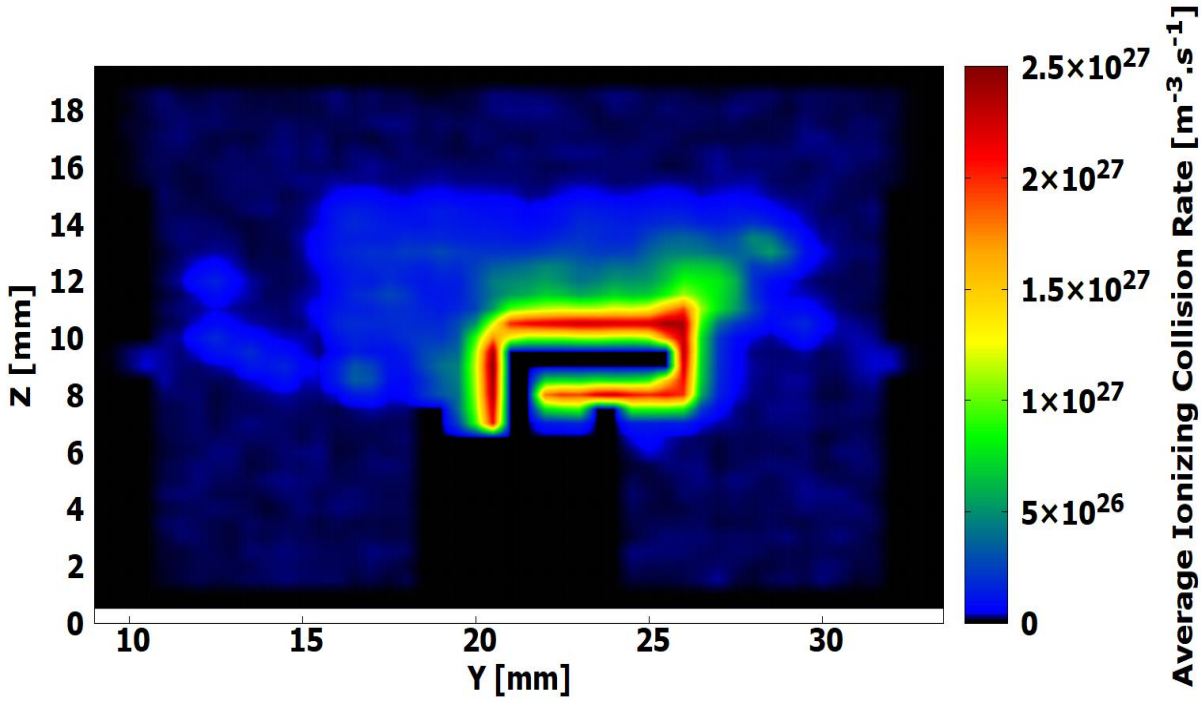

Figure. 4.32: Average Ionizing Collision Rate for the four horizontal inlet configuration

These subtle differences also make their way into the actual ion density distribution within the discharge chamber as well which is evident from Figures 4.33 to 4.36. Much like the ionizing collision rate graphs, there are subtle changes in the ion density distribution between the inlets. These subtle changes can be seen in the lower density regions away from the antenna since the regions surrounding the antenna are saturated with ion particles for all cases. Comparing the two bottom inlets, there is a slight increase in ion density in the opposite end of the antenna region in the four bottom inlet case. Although small, this is a clear change in the ion density within the discharge chamber caused by the neutral density distribution. Moreover, the single horizontal inlet shows a clear increase in the ion density distribution toward the inlet. This change is significant since it shows a clear impact of the horizontal inlet on the ion density near the antenna and a clear increase in ion density which can be seen in the Table 4.4 as well. These changes due to the inlet positioning are of significant importance since they clearly indicate the impact neutral density can have on the ion particle distribution within the discharge chamber. Specifically single horizontal inlet case where a significant shift in the ion density is observed toward the inlet. This needs to be investigated further through experimental setups which gives us an opportunity to optimize and improve the performance of miniature ion thrusters. Finally the average rate of ion loss to the walls for each inlet case is indicated in Figures 4.37 to 4.40. The differences in the neutral recycle rate for the antenna in all cases seems to be almost identical. This is expected since as seen in the previous figures, the rate of ionization and ion density around the antenna is comparable for all inlets. The main difference in the ion loss rate to the walls can be seen in the engine walls on both sides of the engine. While both the single bottom and horizontal inlets lead to a slight increase in the average rate of neutral recycle rate in inlet side of the engine wall, the four inlet configurations leads to a more uniform average rate of neutral recycle rate in the walls. This is significant since we can clearly see the impact of breaking up the gas inlets into smaller inlets in the average ion loss rate to the walls for the first time. Moreover, the antenna on average has the highest rate of ion loss than any other region of the engine. This is expected since as seen in Figures 4.33 to 4.36, the area surrounding the antenna is occupied by a high density of ions. It should be noted, although the antenna has the highest average neutral recycle rate in the engine, by considering the accumulative impact the walls are the main contributor to the neutral recycle rate overall since the walls surrounding the engine have a significantly larger surface area than the antenna. This has major implications since we aim to reduce the amount of ion loss to the walls in an ion thruster and it seems that inlet configuration can contribute to its optimization.

The results of these simulation outcomes averages for selected engine regions as shown in Figure 4.24 are listed in Table 4.4. These average density values along with the average neutral recycle rate are an effective way of assessing the changes in the overall performance of the ion thruster. It is evident from the average density values within the discharge chamber that although the inlet configuration has led to some interesting and significant changes in the average ionization collision rate and ion density near the antenna, the average ion density in the discharge chamber remains similar for all inlet cases. This is an interesting finding which implicates that the changes to the particles behavior caused by the inlet configuration appears to be local and does not seem to alter the overall ion density in the discharge chamber. This needs to be investigated further with experimental data to arrive at a definitive conclusion. Finally, in order to validate and ensure the accuracy of the simulation, the forward and field power fluctuation values during the simulation over the entire system are depicted in Figure 4.41 for the single bottom inlet case.

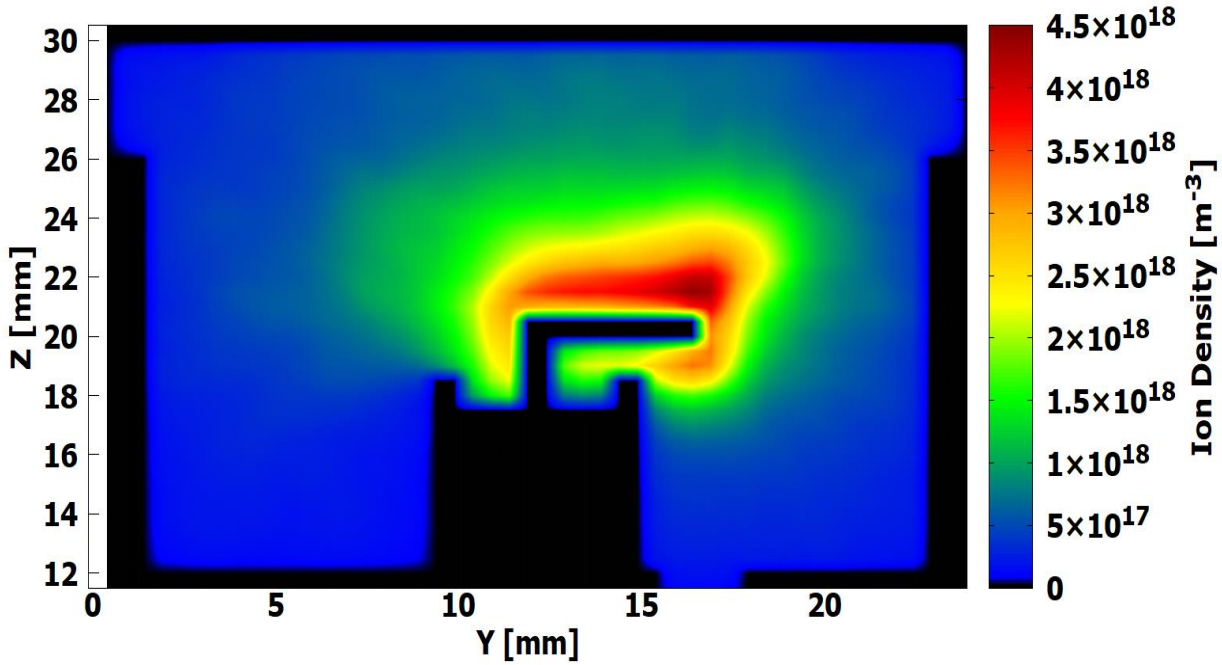

Figure. 4.33: Average Ion Density in the bottom inlet configuration

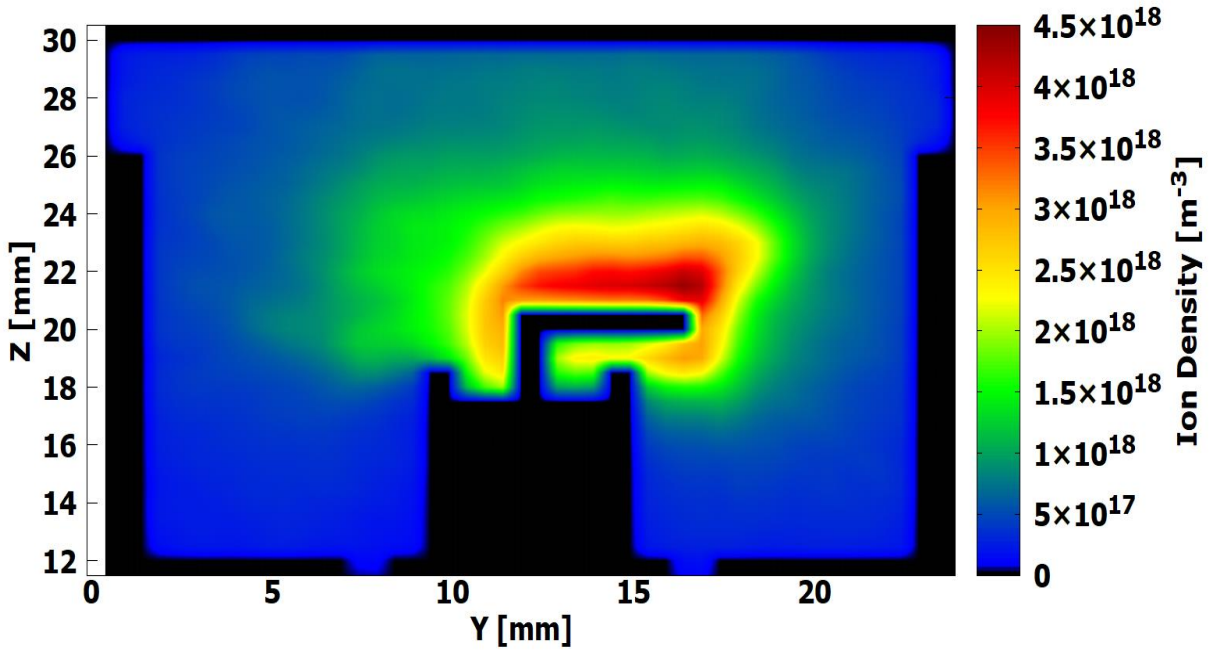

Figure. 4.34: Average Ion Density in the four bottom inlet configuration

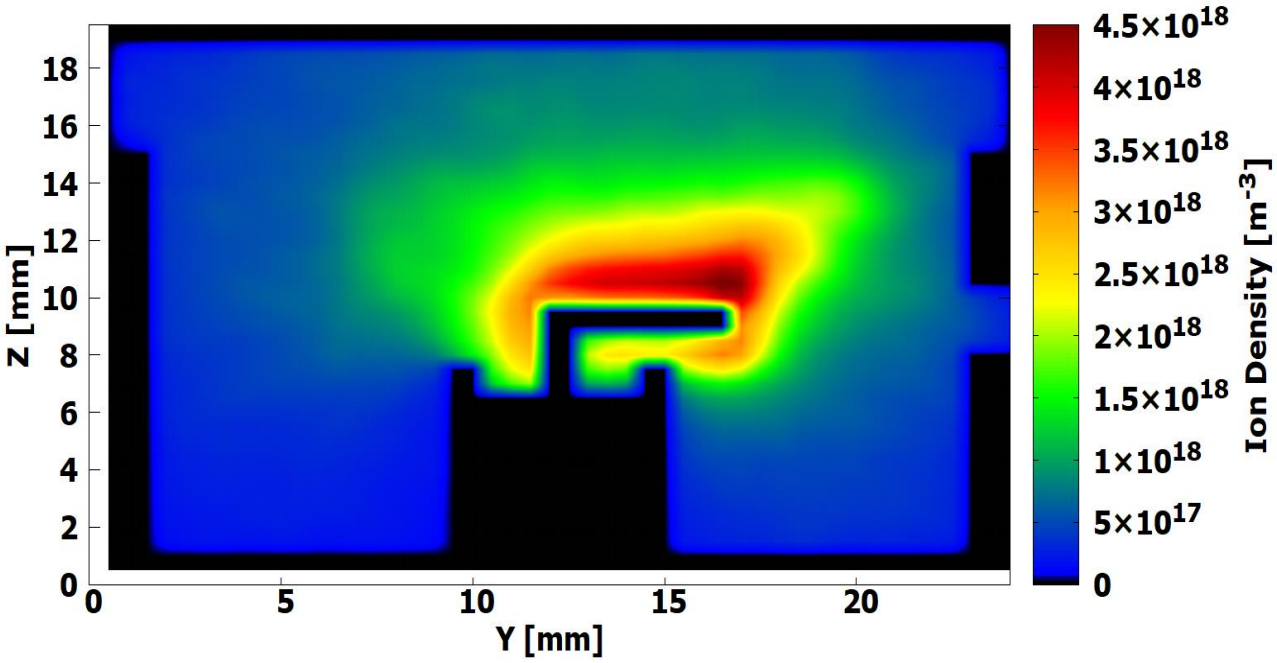

Figure. 4.35: Average Ion Density in the horizontal inlet configuration

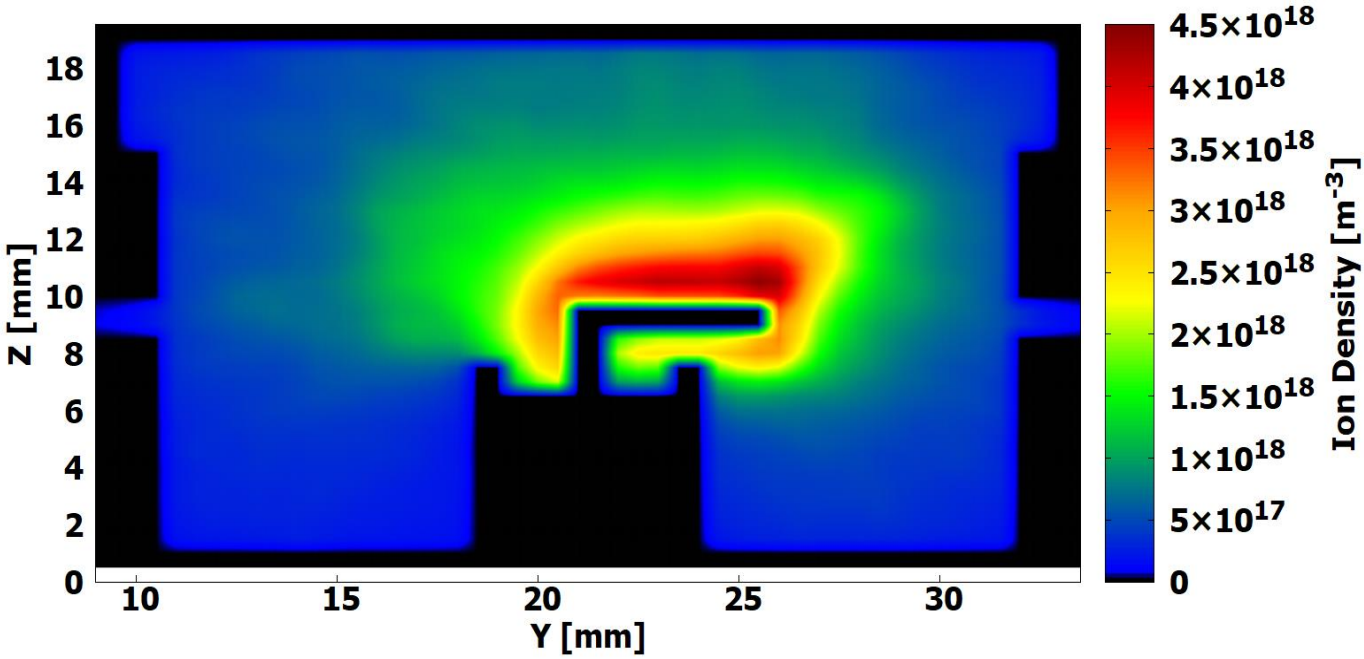

Figure. 4.36: Average Ion Density in the four horizontal inlet configuration

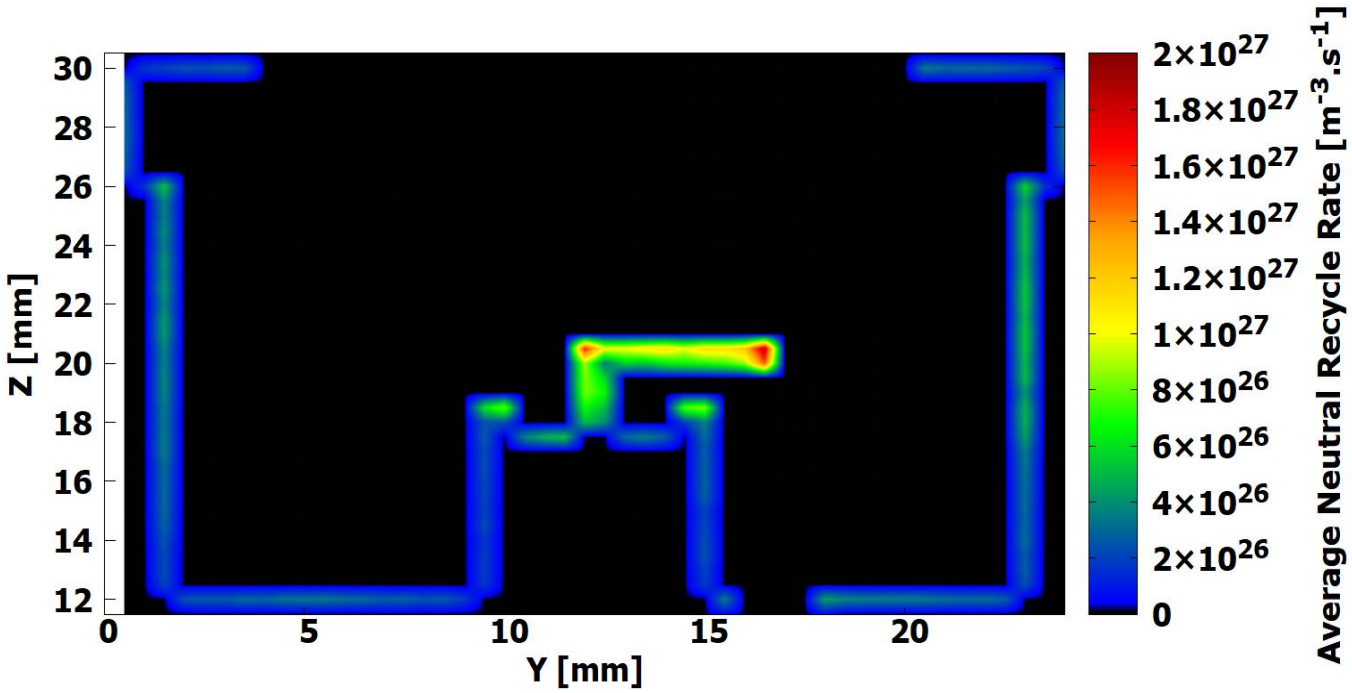

Figure. 4.37: Average Neutral Recycle Rate in the bottom inlet configuration

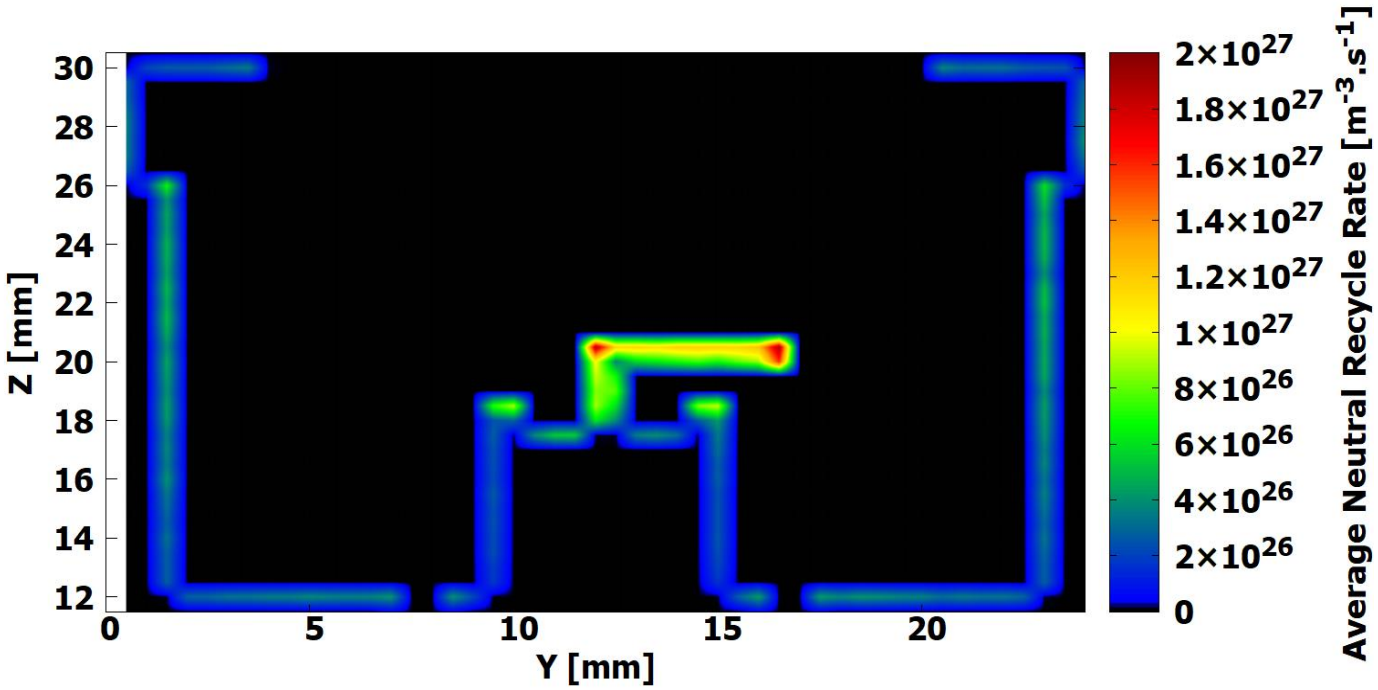

Figure. 4.38: Average Neutral Recycle Rate in the four bottom inlet configuration

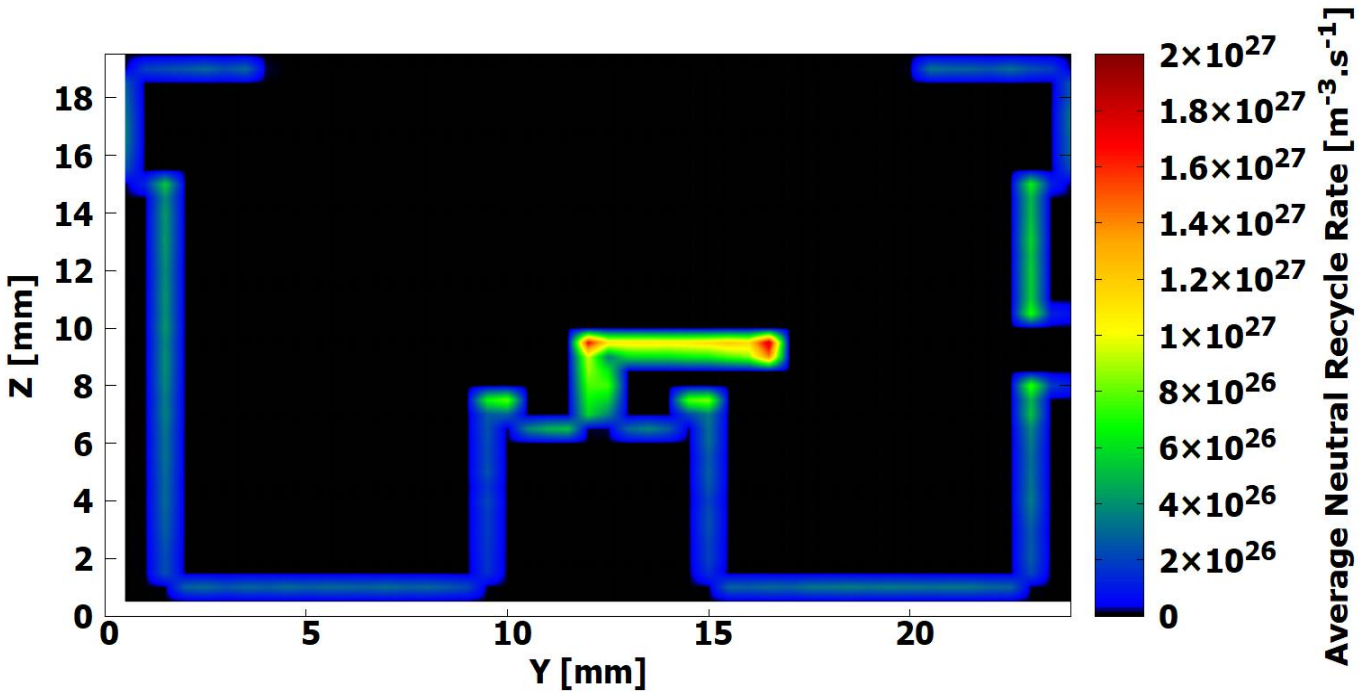

Figure. 4.39: Average Neutral Recycle Rate in the horizontal inlet configuration

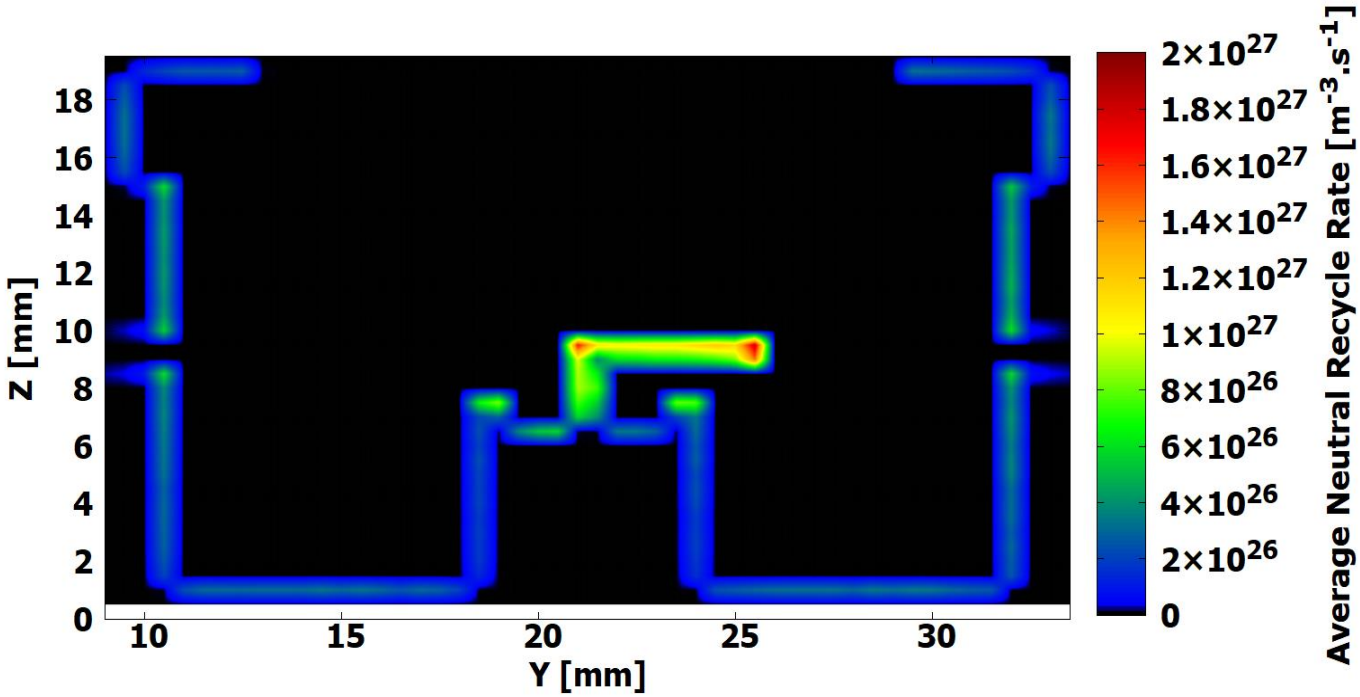

Figure. 4.40: Average Neutral Recycle Rate in the four horizontal inlet configuration

And to ensure plasma neutrality the absolute difference between electron and ion densities averaged over 5 ns is depicted in Figure 4.42 for the single bottom inlet case as well. These figures can be used to analyze the validity of the simulation since as it can be seen in Figure 4.41, the law of conservation of power is upheld during the simulation.

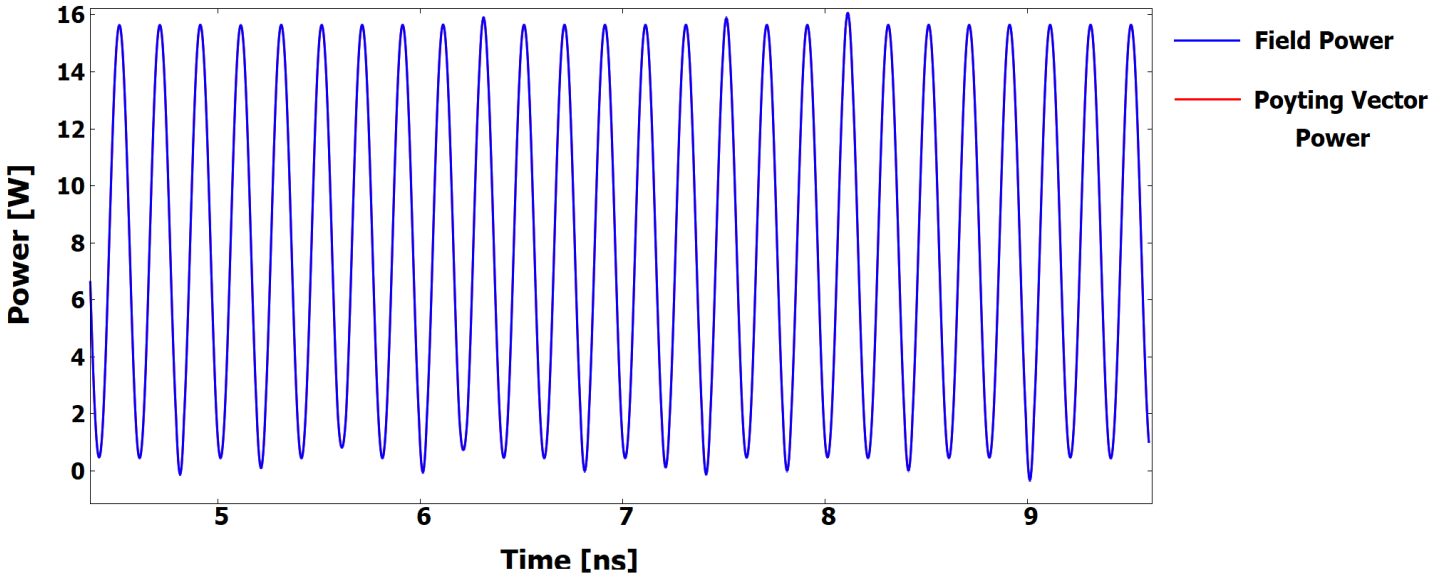

Figure. 4.41: Forward and Field power fluctuating values during simulation

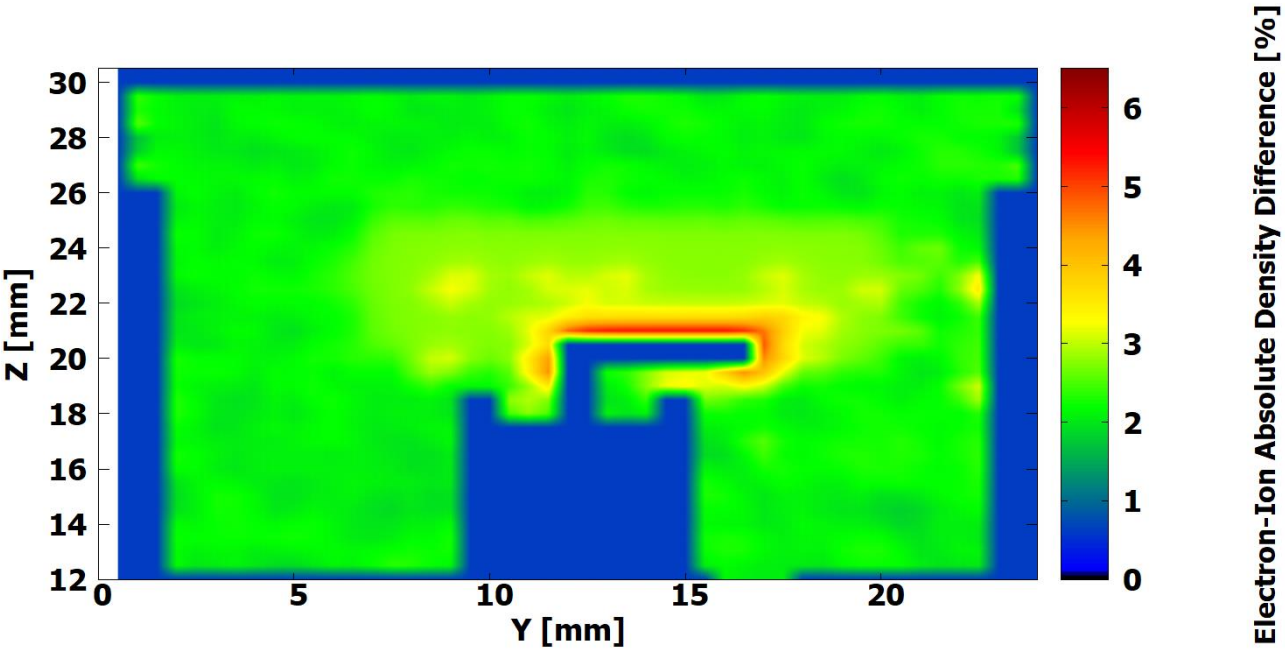

Figure. 4.42: Absolute difference between electron and ion densities averaged over 5 ns

Table. 4.4: Average density (m^{-3}) and recycle rate ($m^{-3}.s^{-1}$) for the L shaped antenna simulation

Inlet Layout	Single bottom inlet	Four bottom inlets	Single horizontal inlet	Four horizontal inlet
Neutral density in discharge chamber	6.43×10^{19}	6.53×10^{19}	6.49×10^{19}	6.42×10^{19}
Ion density in discharge chamber	1.04×10^{18}	1.08×10^{18}	1.11×10^{18}	1.06×10^{18}
Neutral density near the antenna wall	8.13×10^{19}	7.84×10^{19}	9.31×10^{19}	8.12×10^{19}
Ion density near the antenna wall	1.11×10^{18}	1.12×10^{18}	1.17×10^{18}	1.12×10^{18}
Neutral density near the opposite wall	6.36×10^{19}	7.81×10^{19}	6.41×10^{19}	8.13×10^{19}
Ion density near the opposite wall	1.15×10^{18}	1.07×10^{18}	1.87×10^{18}	1.14×10^{18}
Neutral Recycle rate at the antenna wall	5.81×10^{26}	5.14×10^{26}	6.01×10^{26}	5.10×10^{26}
Neutral Recycle rate at the opposite wall	4.98×10^{26}	5.08×10^{26}	4.96×10^{26}	5.11×10^{26}

4.4 Simulation Results for a Disk shaped antenna

Figure 4.43 indicates the simulation geometry for the disk shaped antenna engine with the conventional bottom inlet.

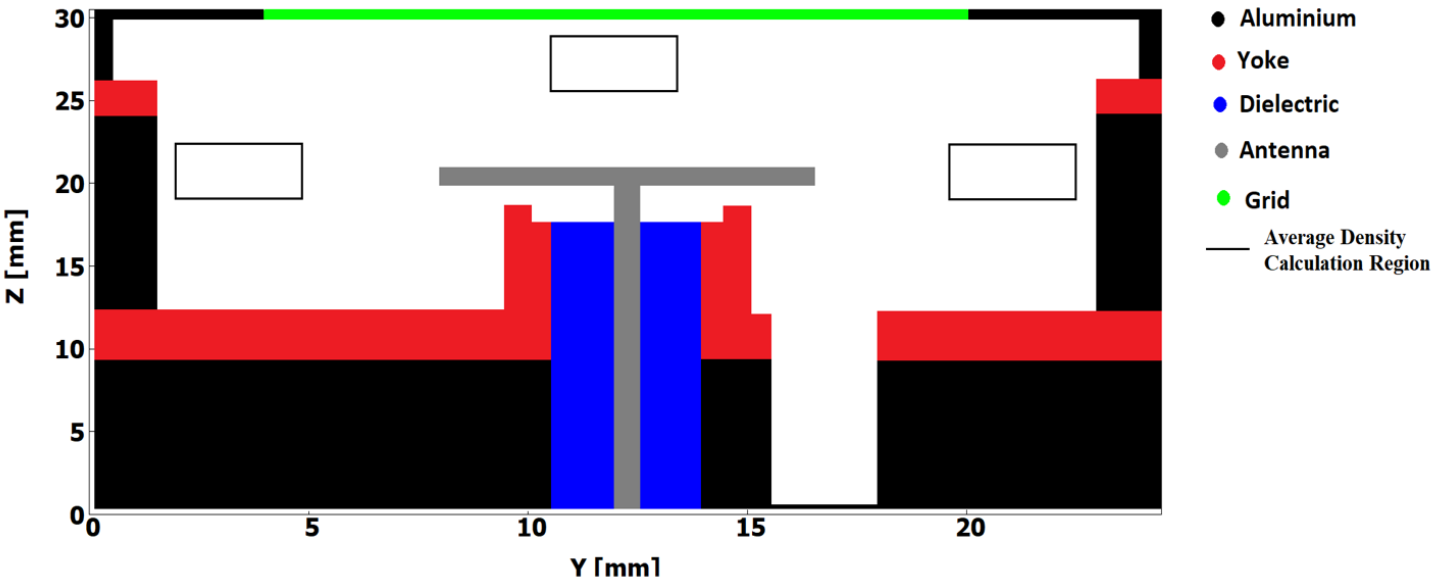

Figure. 4.43: Y-Z Cross section of the Disk shaped antenna thruster taken at X = 12 mm (middle of the simulation geometry) for the conventional bottom inlet with selected average density calculation regions

All the simulation results are taken at the end of the simulation run at the real time of 30ms + 10 ns. Figures 4.44 through 4.47 show the neutral density distribution for each inlet case. The Y-Z plane results are taken at mid-engine (X = 12 mm) while the X-Y data is extracted from the antenna height. Much like the L shaped results, the inlet configuration also alters the neutral density distribution in each case. Similarly to the L shaped antenna, the single bottom and horizontal inlets lead to a non-uniform distribution facing the inlet while the four inlets result in a more uniformly distribution density within the engine.

On the other hand, Figures 4.48 to 4.51 indicate the average rate of ionizing collisions that occur within the discharge chamber. In this case, clearly the majority of the ionizing collisions occurs around and under the antenna with the highest rate being beneath the antenna which is expected. Figure 4.48 indicates the average ionizing collision rate for the bottom inlet configuration. It is clear that the area beneath and near the tip of the disk results in the highest rates of ionizing collisions. However, this ionizing pattern appears to be uniform. This is further evident in Figure 4.48 for the four bottom inlets were the ionizing pattern in the vicinity of the antenna is interestingly uniform as well. On the other hand, considering the ionizing pattern further away from the antenna indicates a small rate of increase for the single bottom inlet facing the inlet. This is further evident in Figure 4.52 where the ion density is increased in the side of the inlet as well. For the four bottom inlets however, the density and the ionization pattern seems to follow a uniform layout. A similar pattern can be seen by comparing the two horizontal inlets in Figures 4.50 and 4.51 where the single horizontal inlet leads to a higher rate of ionizing collisions closer to the walls of the antenna side of the discharge chamber even more clearly than the single bottom inlet case. The four horizontal inlets case however was the surprising result with it having a clear increase in the rate of ionizing collisions near the antenna in contrast to other inlet cases. Although it has a more balanced collision rate between the two sides, there is a clear increase in the ionization rate surrounding the antenna for the four horizontal inlet case. This is an interesting outcome since it was hypothesized that a more uniform distribution of neutrals would benefit a symmetrical antenna like the disk shaped antenna in our previous works. The current results confirms this hypothesis and opens rooms for a possible improvement for the disk shaped antenna configurations.

Considering all the inlets, the neutral density distribution only seems to alter the ionizing collision rate in the lower probability regions slightly as seen in the L shaped simulations as well. However the four horizontal inlets lead to an increase in the ionization rate in the vicinity of the antenna which needs to be investigated further. The small changes in the lower ionizing rate regions can also be seen in the ion density distribution within the discharge chamber as well which is evident from Figures 4.52 to 4.55. Much like the ionizing collision rate graphs, there are subtle changes in the ion density distribution between the inlets. As discussed earlier with comparing the two bottom inlets, there was a slight increase in the rate of ionizing collisions for the single bottom inlet case. This increase can also be seen in the ion density distribution which is more evident. Moreover, the single horizontal inlet shows a clear increase in the ion density distribution toward the inlet. This change is similar to the result observed in the L shaped antenna simulation where the horizontal inlet led to an increase in the ion density in its vicinity. Although the effect seen for the disk shaped antenna is smaller, it still persists adding weight to the idea that horizontal inlet configuration might be beneficial for miniature ion thrusters. The interesting result comes from the four horizontal inlet case where as seen from Figure 4.51, there was a clear increase in the rate of ionizing collisions occurring surrounding the antenna.

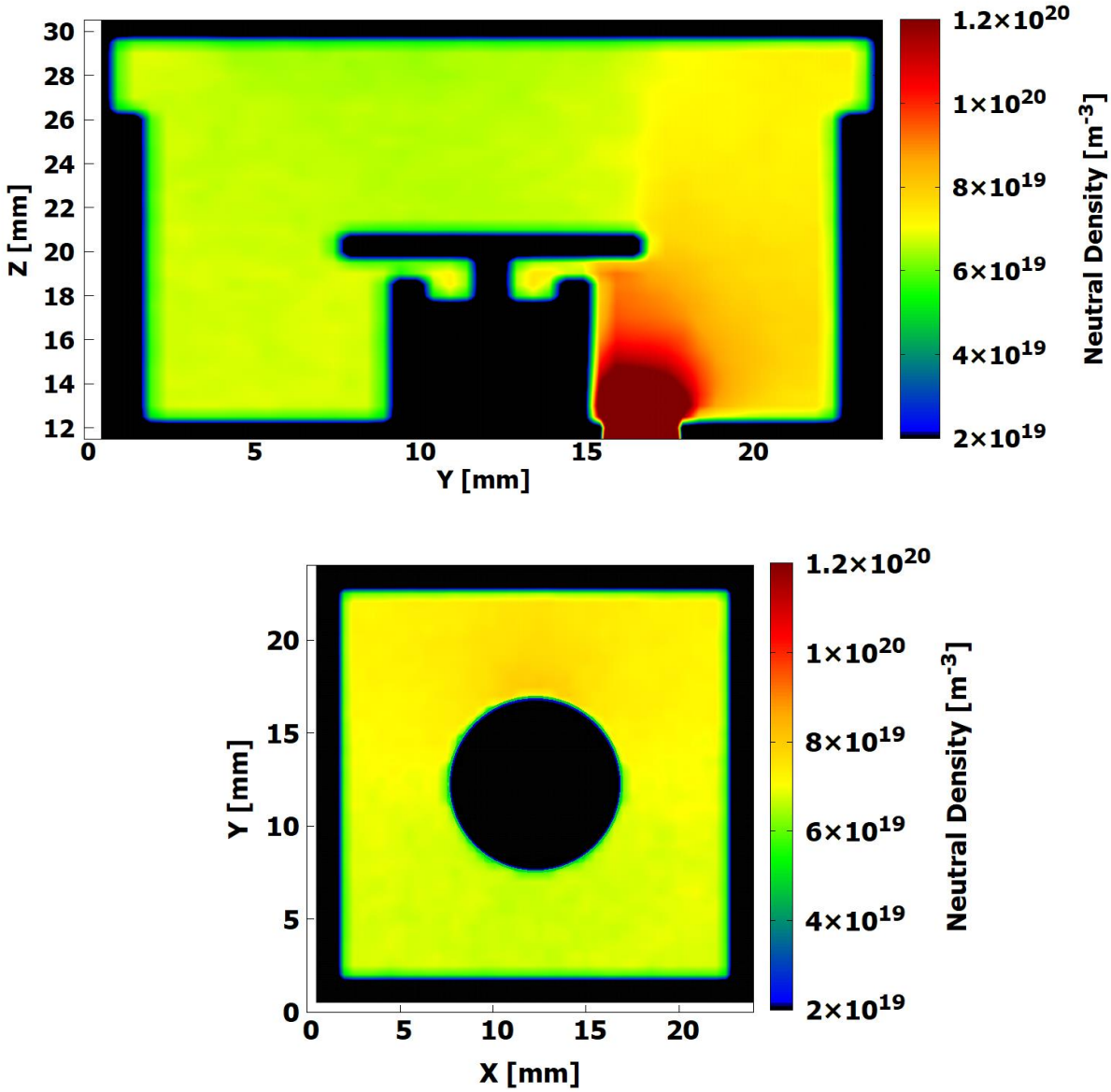

Figure. 4.44: Neutral density distribution for the bottom inlet configuration: (top) Y-Z plane and (bottom) X-Y plane.

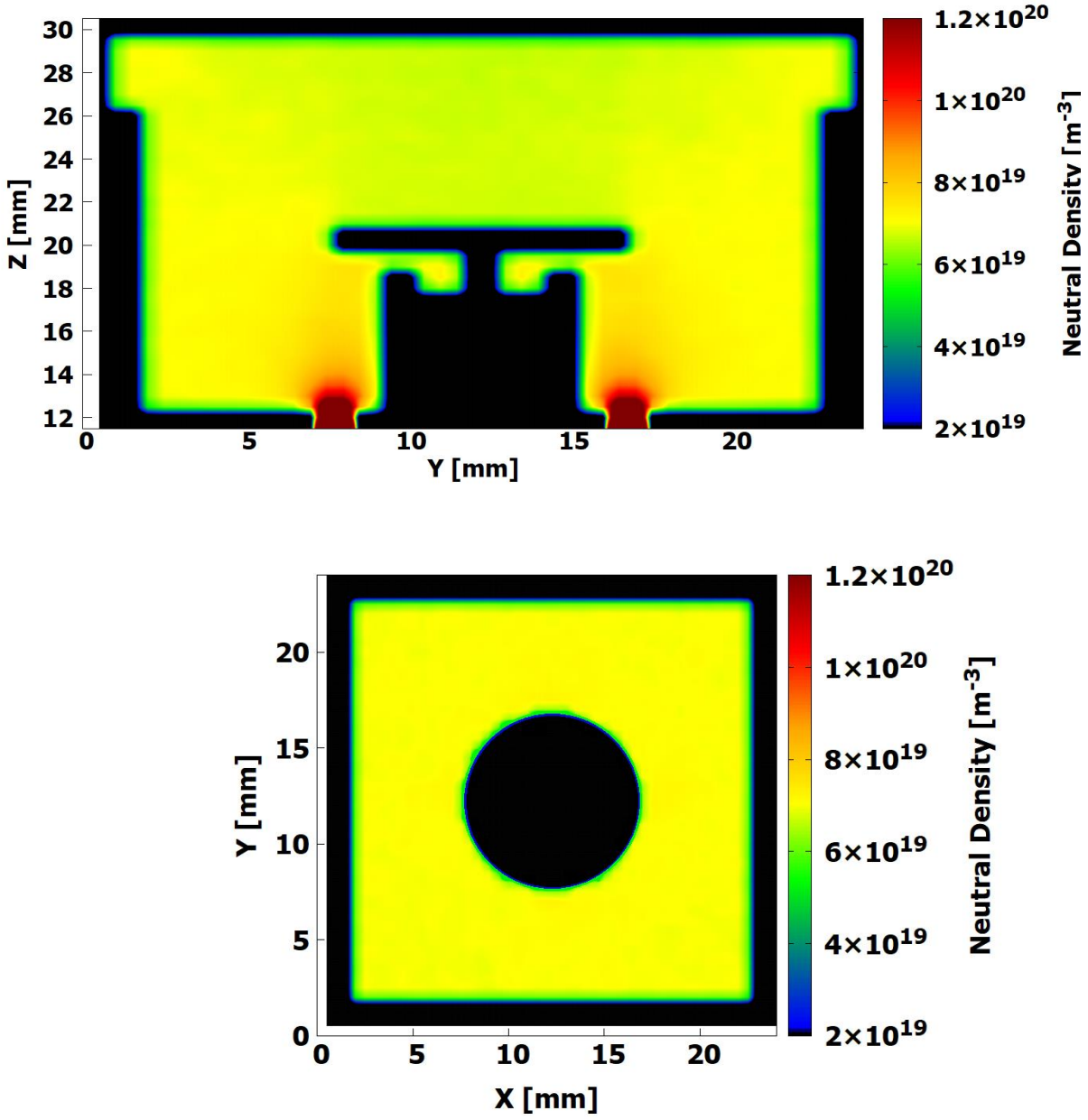

Figure. 4.45: Neutral density distribution for the four bottom inlet configuration: (top) Y-Z plane and (bottom) X-Y plane.

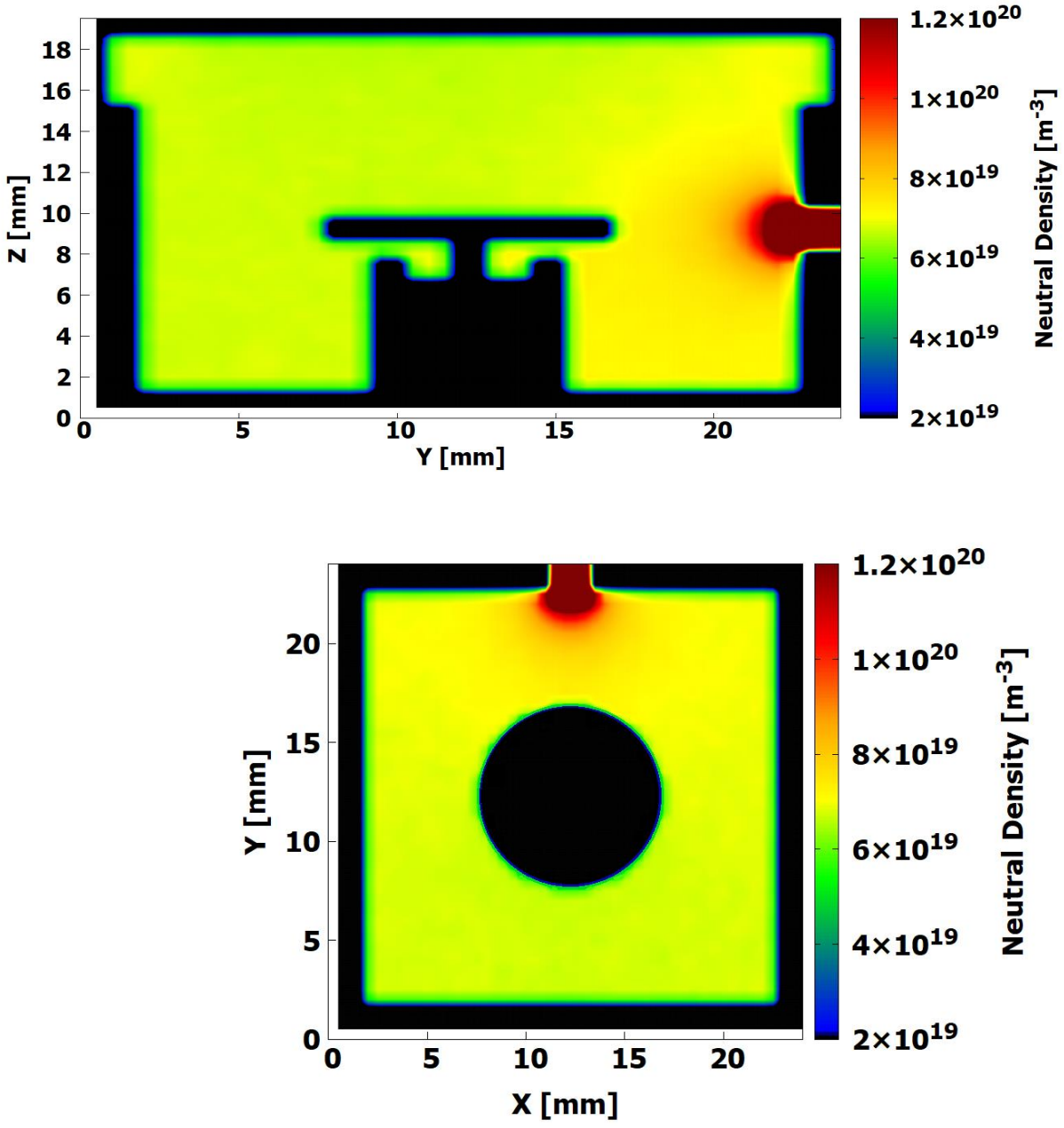

Figure. 4.46: Neutral density distribution for the horizontal inlet configuration: (top) Y-Z plane and (bottom) X-Y plane.

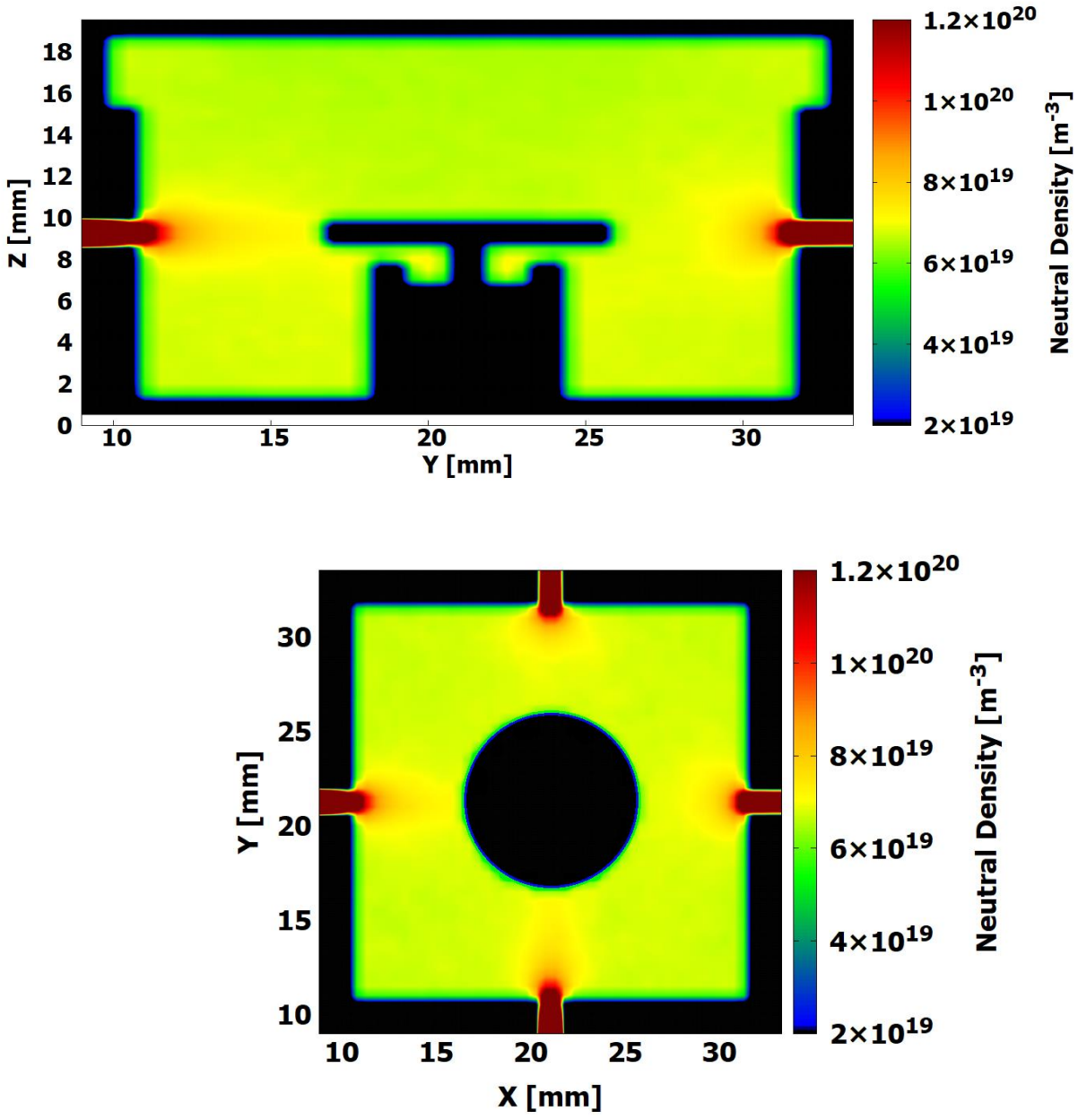

Figure. 4.47: Neutral density distribution for the four horizontal inlet configuration: (top) Y-Z plane and (bottom) X-Y plane.

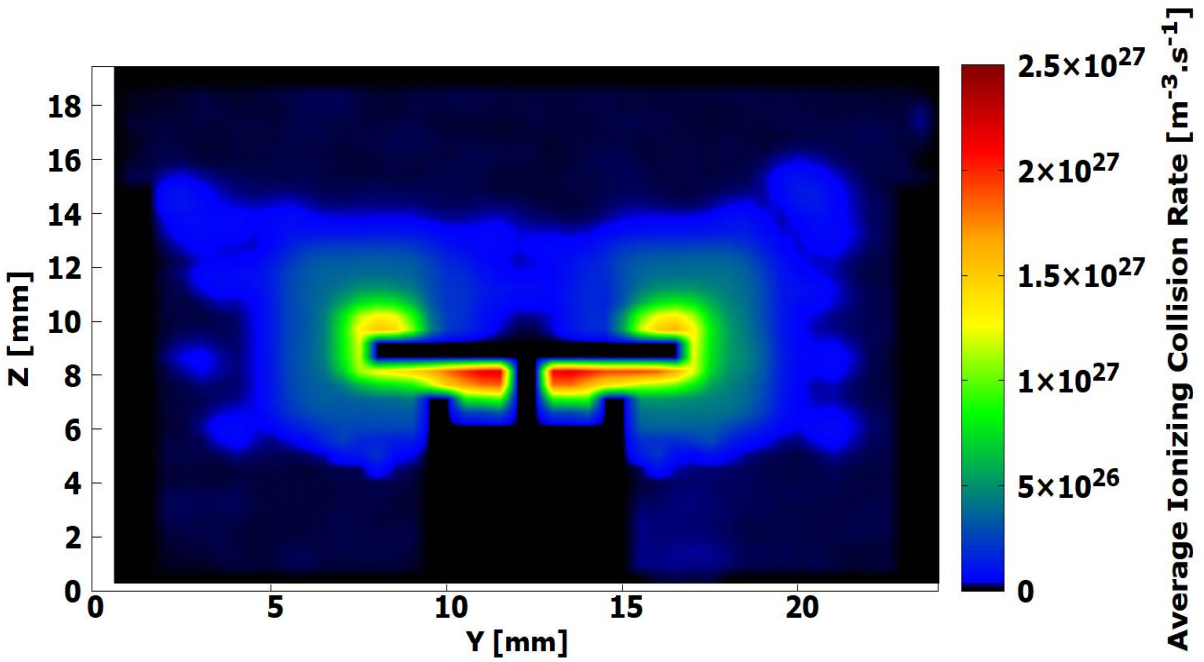

Figure. 4.48: Average Ionizing Collision Rate for the bottom inlet configuration

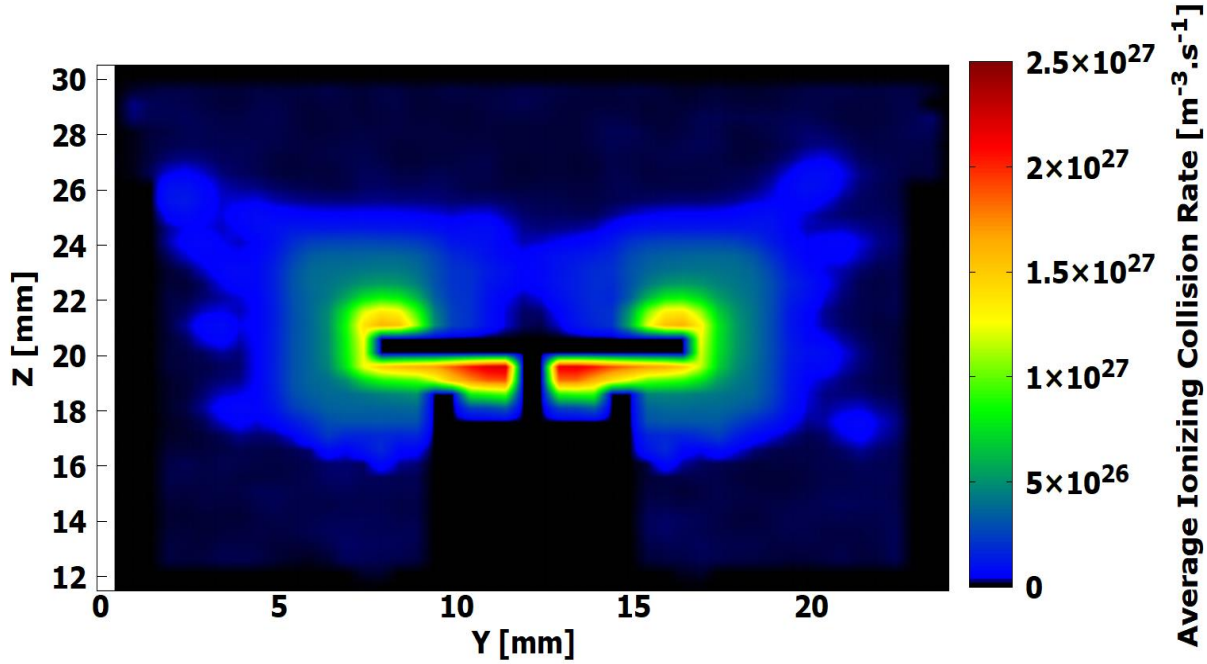

Figure. 4.49: Average Ionizing Collision Rate for the four bottom inlets configuration

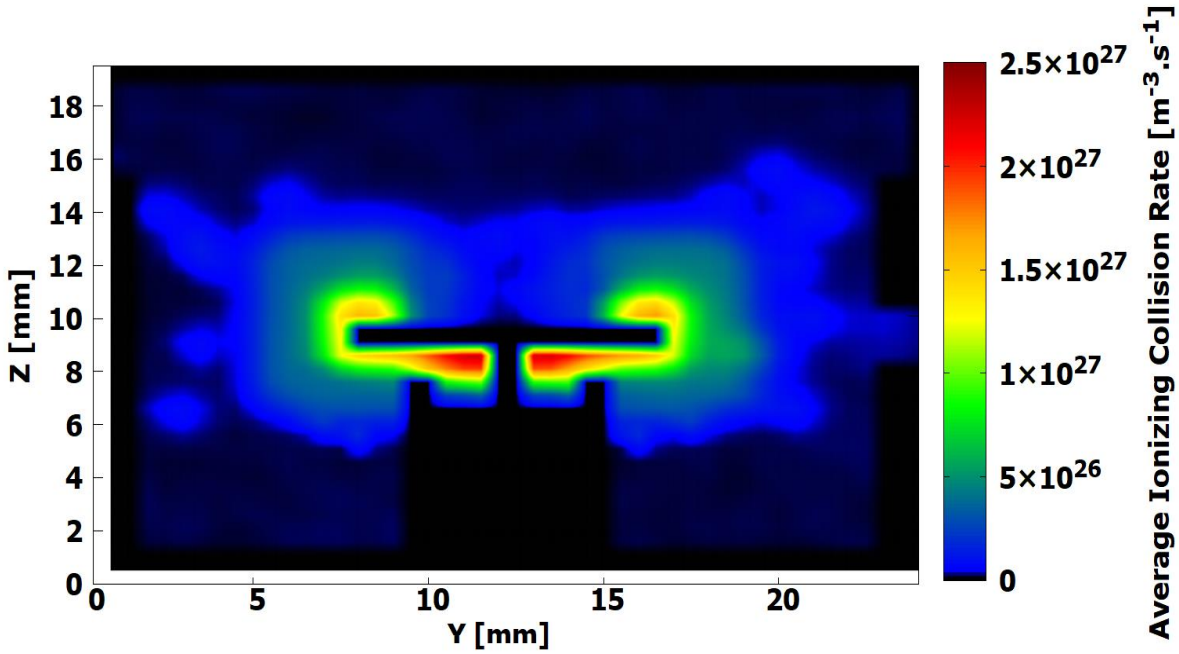

Figure. 4.50: Average Ionizing Collision Rate for the horizontal inlet configuration

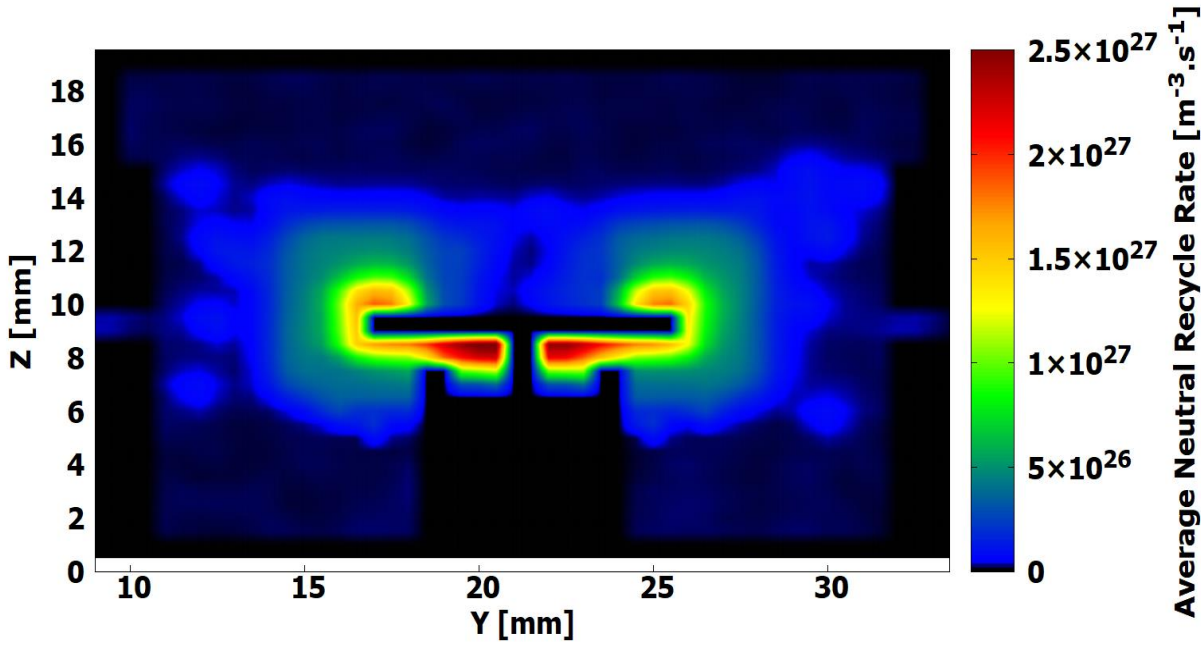

Figure. 4.51: Average Ionizing Collision Rate for the four horizontal inlet configuration

This increase in the ionizing collision however does not seem to translate into significant increase in the ion density in comparison to other inlet cases. This can be explained by the neutral recycle phenomenon since the increase in the ionization rate was mainly beneath the disk shaped antenna where the generated ions are in an enclosed space making it more likely for them to collide with the surrounding walls and returning as a neutral. This further showcases the importance of the neutral recycling phenomena in the discharge chamber which is not as well studied.

Lastly the average rate of ion loss to the walls for each inlet case is indicated in Figures 4.56 to 4.59. The differences in the neutral recycle rate for the antenna in all cases seems to be insignificant. However as mentioned earlier this is not the case for the four horizontal inlet configuration which has an increased rate of neutral recycle rate in the vicinity of the antenna. In a similar fashion to the L shaped antenna results, the main difference in the ion loss rate to the walls can be seen in the engine walls on both sides of the engine. The four inlets led to a more similar rate of neutral recycle event on both sides of the walls while the single inlets led to a more non identical increase in the rate of ion loss near the wall in the vicinity of the inlet. Also identical to the L shaped antenna result, the disk antenna on average has the highest rate of ion loss than any other region of the engine. Finally, the results of these simulation outcomes averages for selected engine regions as shown in Figure 4.43 are listed in Table 4.5. It is clear from the average density values within the discharge chamber that the inlet configuration has not significantly altered the average ion density in the discharge chamber. This further amplifies the results that the changes caused by the inlet cases are limited to the vicinity of the inlet and does not seem to propagate far into the engine. Finally it should be noted that aside from the theoretical validation of our simulation depicted in Figures 4.41 and 4.42, the neutral and electron information derived from our simulation is in agreement with previously obtained experimental values and simulations conducted in this field [71-73].

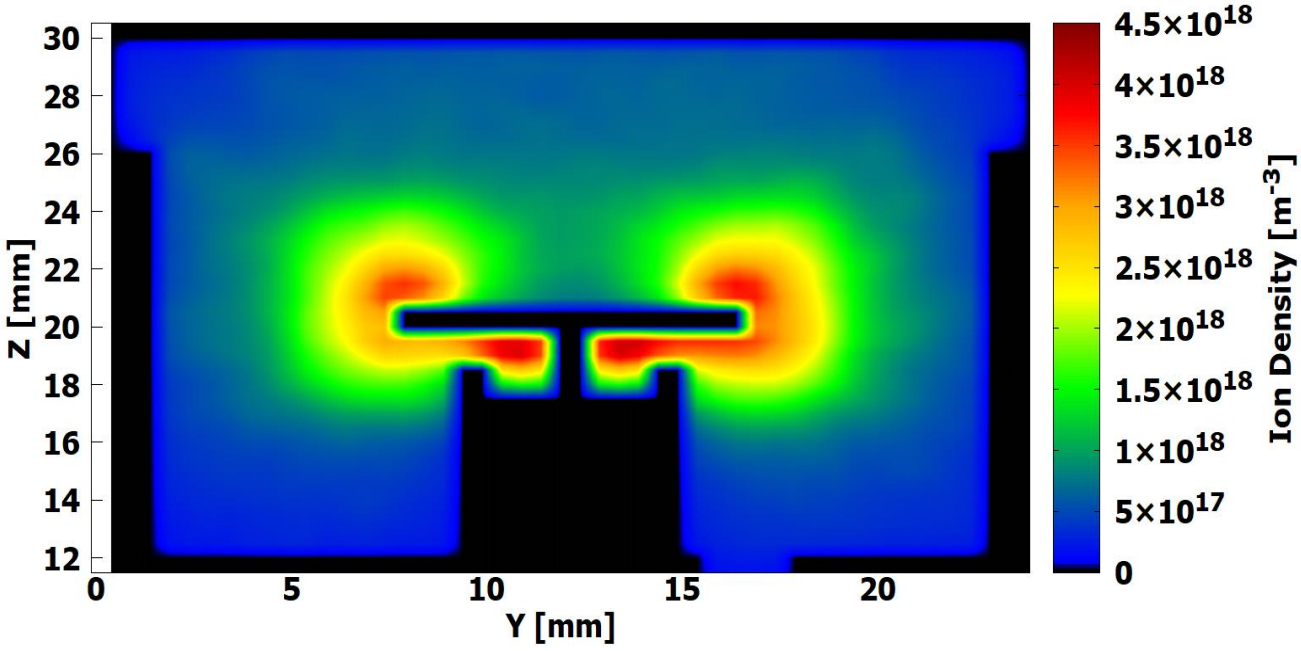

Figure. 4.52: Average Ion Density in the bottom inlet configuration

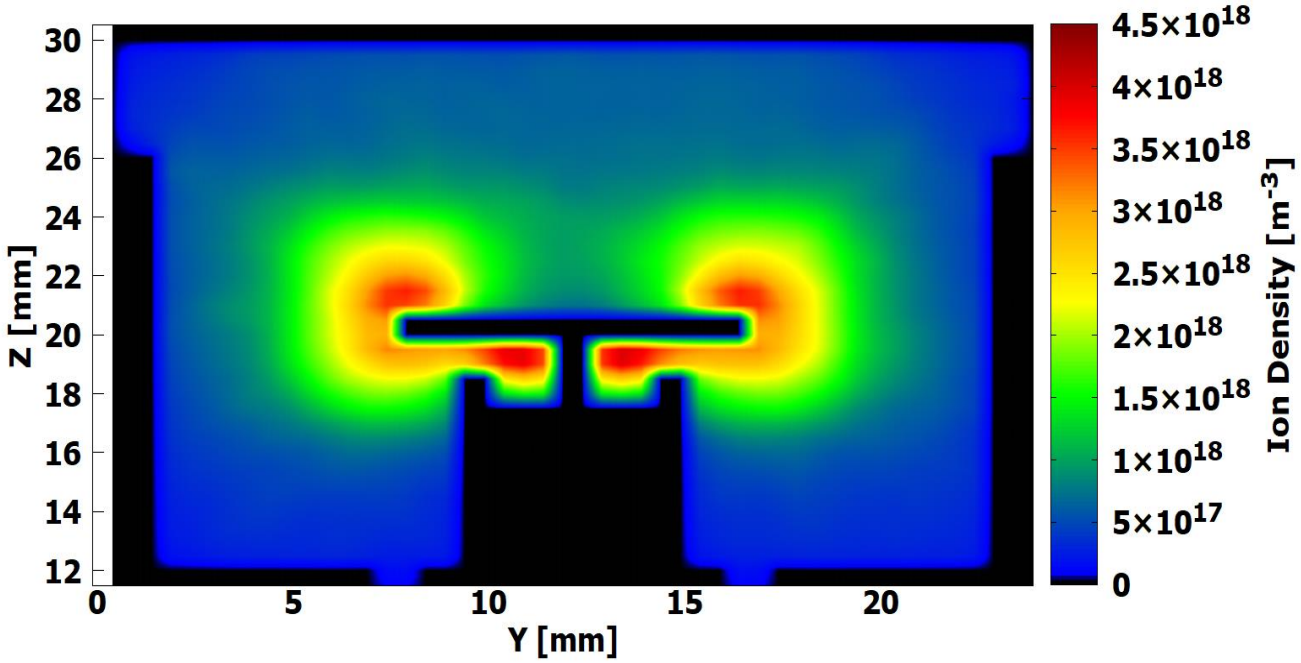

Figure. 4.53: Average Ion Density in the four bottom inlet configuration

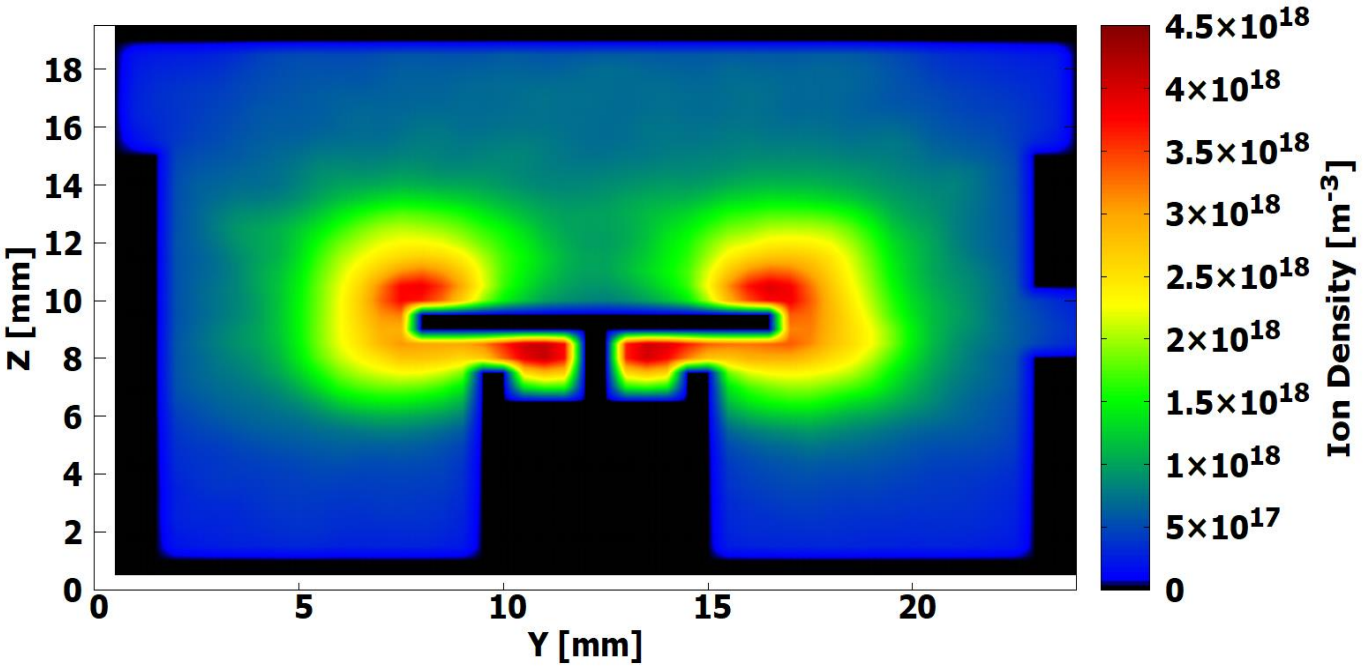

Figure. 4.54: Average Ion Density in the horizontal inlet configuration

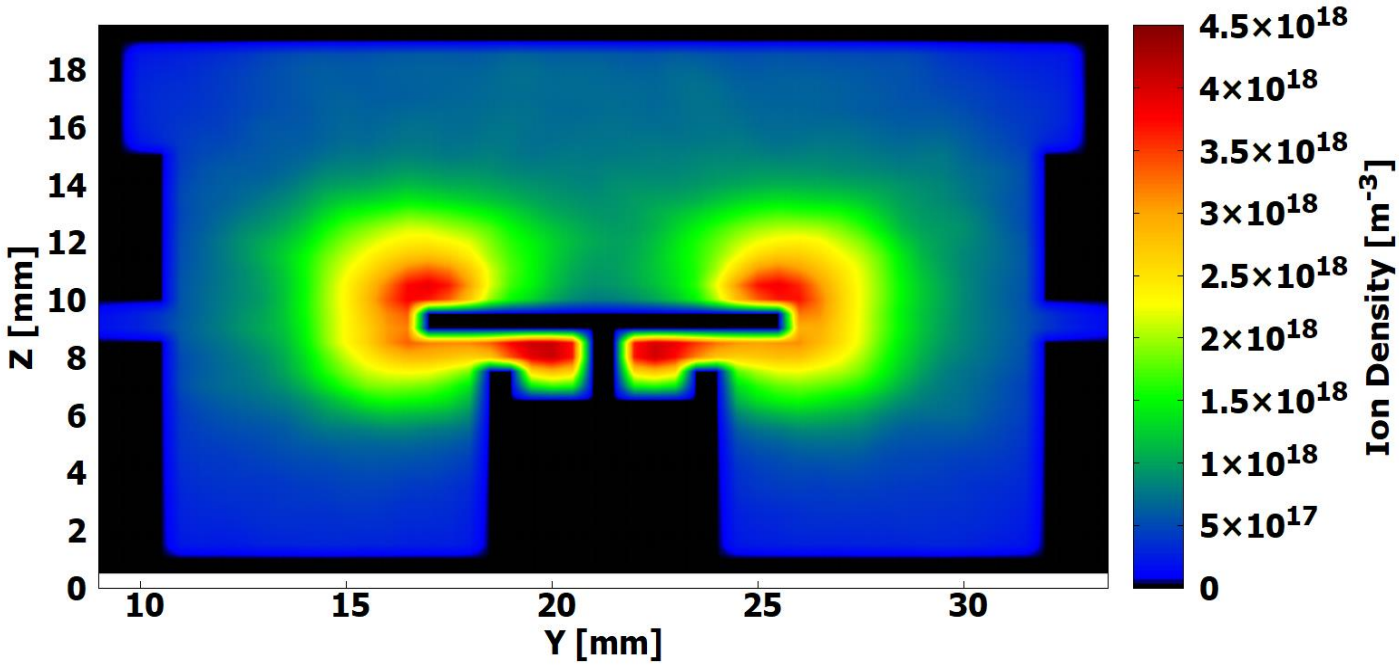

Figure. 4.55: Average Ion Density in the four horizontal inlet configuration

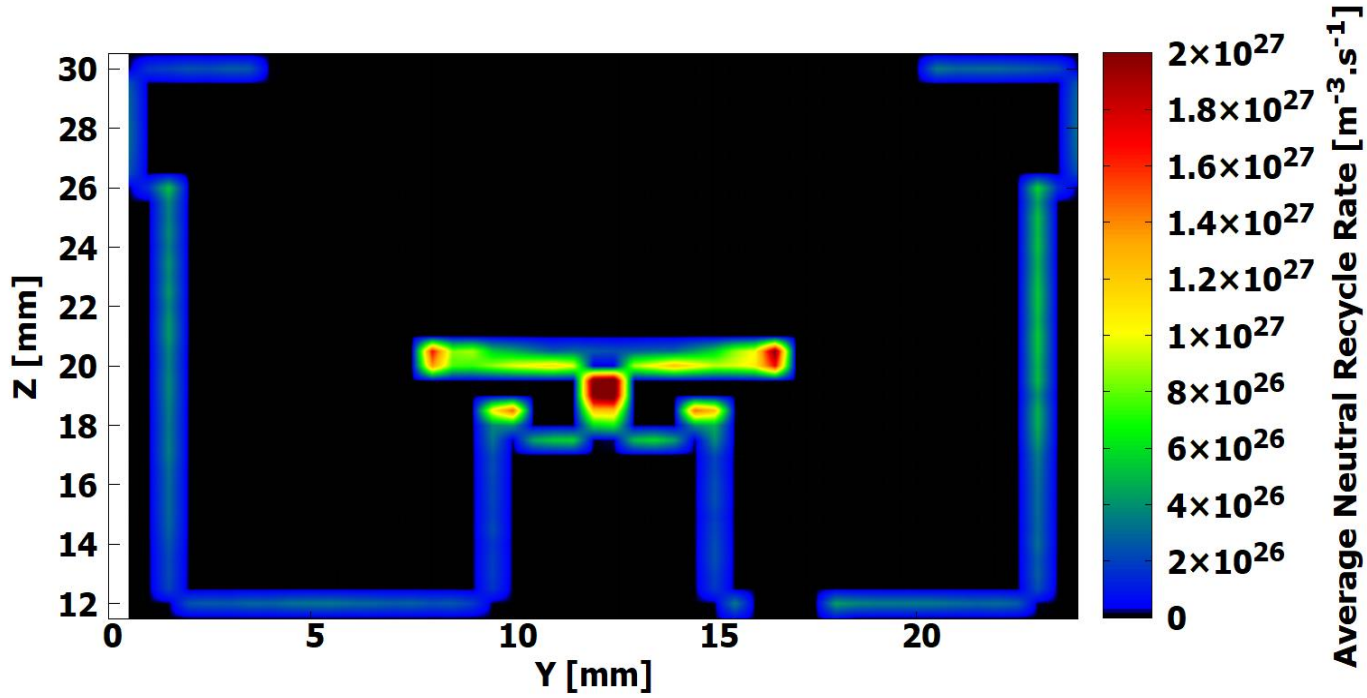

Figure. 4.56: Average Neutral Recycle Rate in the bottom inlet configuration

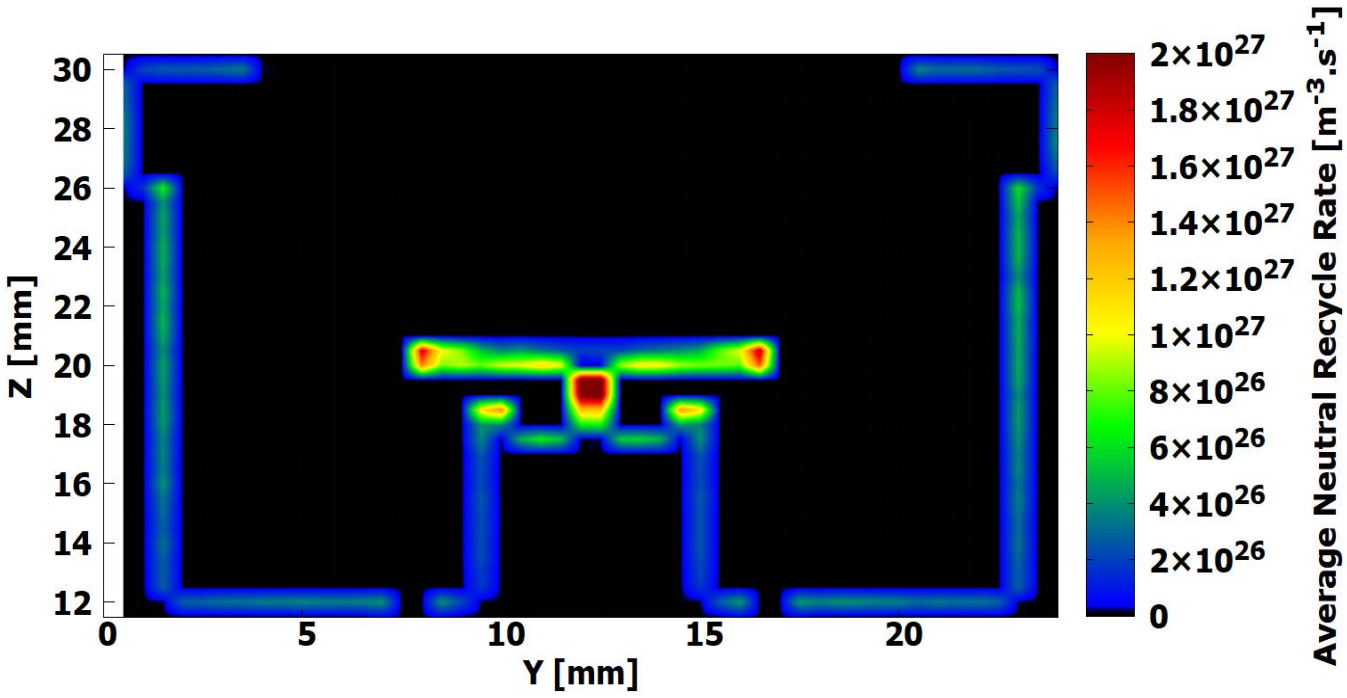

Figure. 4.57: Average Neutral Recycle Rate in the four bottom inlet configuration

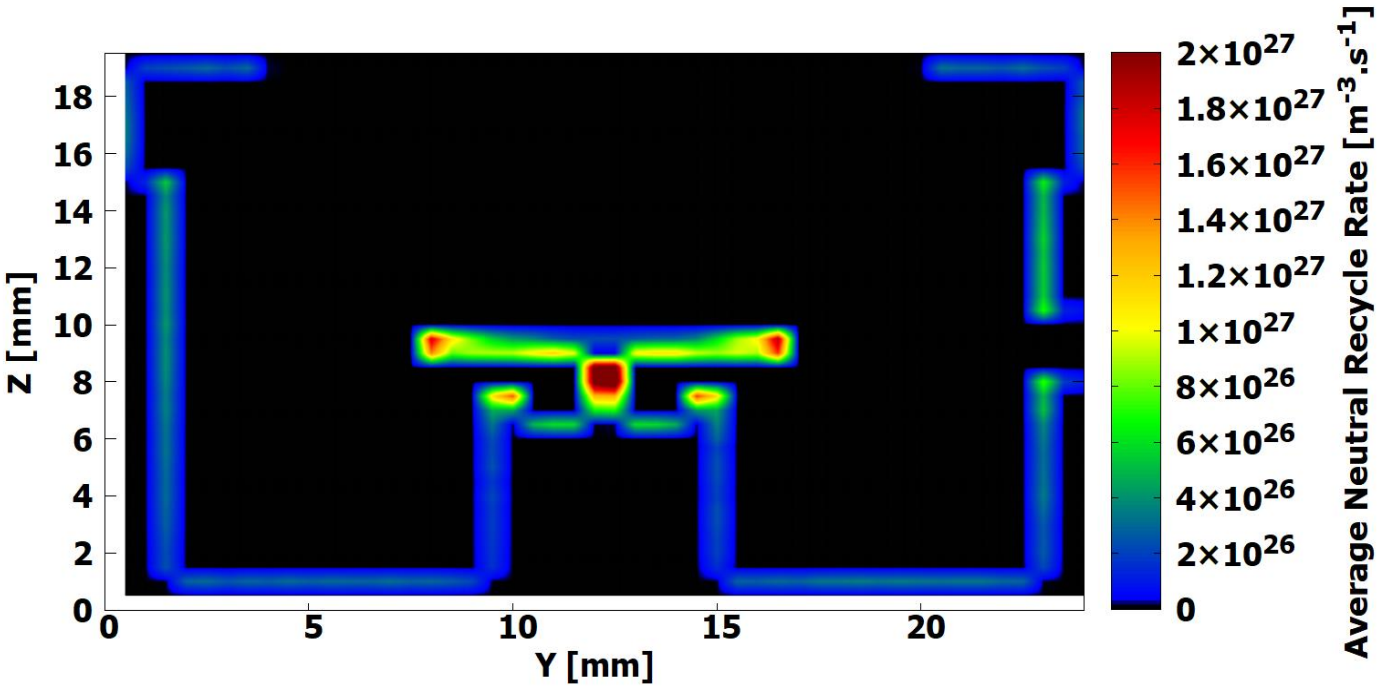

Figure. 4.58: Average Neutral Recycle Rate in the horizontal inlet configuration

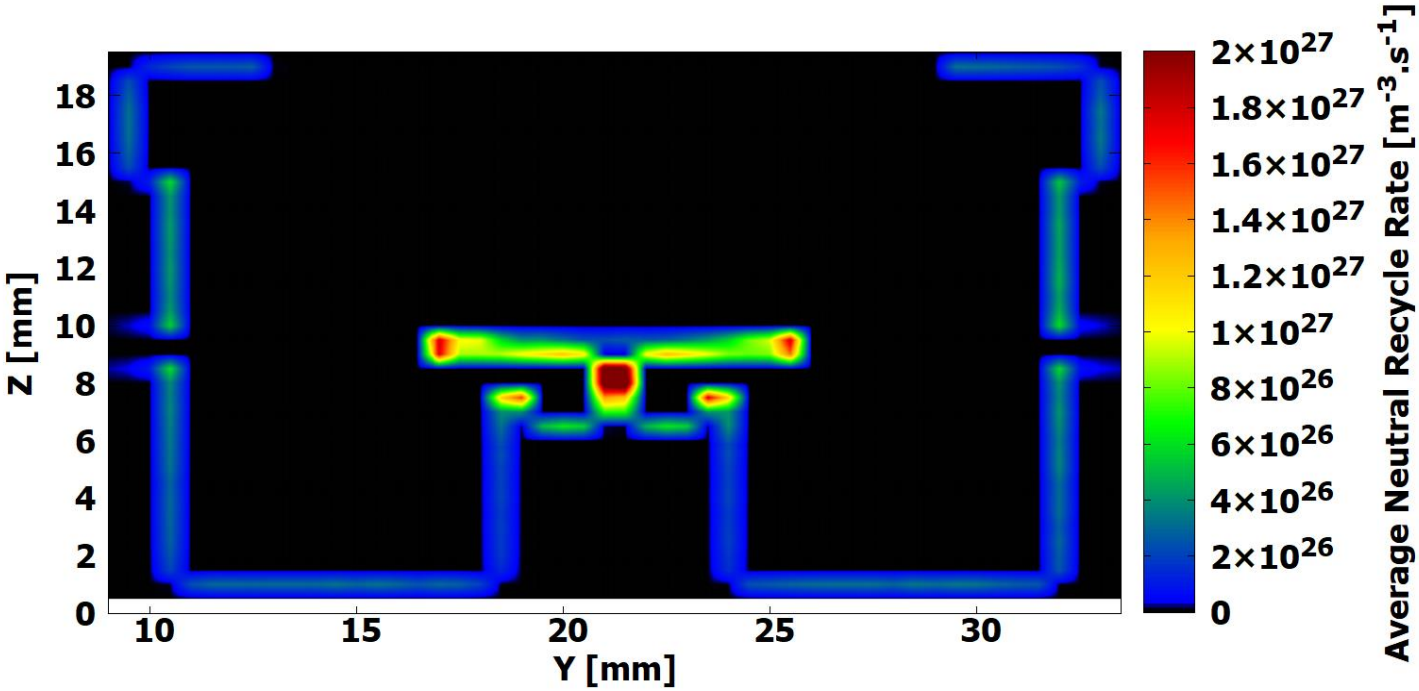

Figure. 4.59: Average Neutral Recycle Rate in the four horizontal inlet configuration

Table. 4.5: Average density (m^{-3}) and recycle rate ($m^{-3}.s^{-1}$) for the Disk shaped antenna simulation

Inlet Layout	Single bottom inlet	Four bottom inlets	Single horizontal inlet	Four horizontal inlet
Neutral density in discharge chamber	6.41×10^{19}	6.51×10^{19}	6.53×10^{19}	6.40×10^{19}
Ion density in discharge chamber	1.05×10^{18}	1.07×10^{18}	1.13×10^{18}	1.04×10^{18}
Neutral density near the antenna wall	8.15×10^{19}	7.83×10^{19}	9.34×10^{19}	8.09×10^{19}
Ion density near the antenna wall	1.12×10^{18}	1.14×10^{18}	1.19×10^{18}	1.09×10^{18}
Neutral density near the opposite wall	6.38×10^{19}	7.79×10^{19}	6.42×10^{19}	8.11×10^{19}
Ion density near the opposite wall	1.13×10^{18}	1.09×10^{18}	1.85×10^{18}	1.15×10^{18}
Neutral Recycle rate at the antenna wall	5.82×10^{26}	5.12×10^{26}	6.03×10^{26}	5.08×10^{26}
Neutral Recycle rate at the opposite wall	4.97×10^{26}	5.09×10^{26}	4.95×10^{26}	5.10×10^{26}

5

Conclusion

Our research focuses on the simulation of plasma particles within a miniature ion thruster and neutralizer. It is well known that the electron density distribution and microwave plasma coupling plays a major role in determining the performance of a miniature thruster. However, the impact of neutral density distribution and neural recycle rate within the thruster is not well studied. Since the neutral density can easily be influenced and altered with simple changes made to the gas inlet configuration, we developed the hypothesis that altering the gas inlet configuration within a neutralizer and ion thruster would lead to significant changes to the natural density distribution and consequently possible changes to the ionization pattern, ion density and neutral recycle rate. With that in mind we aimed to develop an all-inclusive 3D FDTD-PIC simulation of plasma inside the discharge chamber where all particles (ions, electrons and neutrals) are treated as active particles. At first we developed a neutrals only 3D PIC code to evaluate the impact of neutrals density distribution inside a neutralizer to test the assumption that inlet configuration can alter the neutral density significantly. This simulation resulted in a clear observation of the changes within the discharge chamber in neutral density distribution with regards to the inlet changes.

Next we developed a simplified ion-neutral code where the effects of electromagnetic field was ignored, to analyze the neutral recycle impact within a neutralizer and test the assumption that the inlet configuration has the potential to alter the neutral recycle rate pattern within the discharge chamber as a result of gas inlet configuration. Although this simulation had limited scope in terms of accuracy (the electromagnetic field being ignored) it showed the potential to alter the ion loss pattern by adjusting the gas inlet configuration. With this result we worked on developing a full 3D FDTD-PIC simulation of a miniature ion thruster with a Poisson solver to fully analyze the impact of gas inlet configuration of neutral and ion density and neutral recycle rate within the discharge chamber. We incorporated a very fine mesh size of 0.1 mm and decided to not include an artificial sheath potential as a first step in developing a more realistic simulations. Although our current code cannot simulate the plasma sheath as accurately as we hope due to the large mesh size, due to our current hardware limitations we hope this code would be a stepping stone in the near future were advancements in hardware technology will allow for a simulation with a much smaller mesh size to enable sheath simulation. With that limitation in mind we set to analyze the ion-neutral behavior for two candidate antennas (L shaped and Disk shaped) as well as four candidate inlet configurators.

The simulation results indicated a clear shift in ion and neutral densities towards the gas inlet especially in the single horizontal inlet configurations for both antenna shapes. However the impact for the L shaped antenna was more prominent. On the other hand, the four horizontal inlet configuration led to a significantly higher rate of ionization in the vicinity of the disk shaped antenna which was then counteracted by neutral recycle impact. Moreover, the simulation of the neutral recycle rate showed a clear pattern towards the position of the gas inlet where the single inlets experienced and increased rate of ion loss in the walls closer to the inlets. Despite these changes, the average ion and neutral densities in the discharge chamber remained largely unchanged leading to the conclusion that the changes in the ionization pattern and ion density are mainly local and may not translate into larger meaningful outcomes for the engine performance. Despite this, we recommend further research into the possibility of the single horizontal inlet configuration for the L shaped antenna and the four horizontal inlets configuration for the disk shaped antenna as an alternative. Further experiments are recommended to assess the impact of these recommendations for the proposed engines.

References

[1]. Futron Corporation, “Space transportation costs: trends in price per pound to orbit 1990-200,” Tech. Rep., 2002.

[2]. R. J. Cybulski, D. M. Shellhammer, R. R. Lovell, E. Domino, and J. T. Kotnik, “Results from SERT I ion rocket flight test,” National Aeronautics and Space Administration Glenn Research Center (formerly Lewis Research Center), Tech. Rep., 1965.

[3]. R. Killinger, H. Bassner, G. Kienlein, and J. Müller, “Electric propulsion system for ARTEMIS,” in The 26th International Electric Propulsion Conference, Kitakyushu, Japan, 1999.

[4]. J. R. Brophy, M. A. Etters, J. Gates, C. E. Garner, M. Klatte, C. J. Lo, M. G. Marcucci, S. Mikes, M. Mizukami, B. Nakazono, and G. Pixler, “The Dawn ion propulsion system- getting to launch,” in The 30th International Electric Propulsion Conference, Florence, Italy, 2007.

[5]. K. Kuriki, Y. Arakawa, “Introduction to Electric Propulsion Rocket”, the University of Tokyo Press, 2003

[6]. M. Shintani , “Numerical Analysis of Microwave Discharge Type Compact Ion Engine”, Masters Thesis (in Japanese). Kyushu University Fukuoka, Japan, 2010.

[7]. R. G. John, “Physics of Electric Propulsion ", 1968, 2-23.

[8]. S. Hosoda and H. Kuninaka, “The homeward journey of asteroid explorer ”Hayabusa” powered by the ion engines,” *Journal of Plasma and Fusion Research*, Vol. 86 (No.5), pp. 282–292, 2010.

[9]. S. S. H. Kuninaka, “Development of microwave discharge ion thruster for asteroid sample return mission,” 32nd AIAA/ASME/SAE/ASEE Joint Propulsion Conference and Exhibit, Vol. AIAA-1996-2979, 1996

[10]. M. Kato, S. Takayama, K. Yoshihara, and H. Hashimoto, Congress paper IAC-05.B5.01, 2005

[11]. H. Sahara, S. Nakasuka, and C. Kobayashi, AIAA paper 2005-3956, 2005

[12]. J. Muller, C. Marrese, J. Polk, E. Yang, A. Green, V. White, D. Bame, I. Chadraborty and S. Vargo, *Acta Astronomica* , Vol 52 , 2003 , pp 881-895

[13]. P. J. Wilbur, V. K. Rawlin, and J. R. Beattie, *Journal of propulsion and power* , Vol 14 , 1998 , pp 708-715

[14]. Micci, M. M. and Ketsdever, A. D.: Micropropulsion for Small Spacecraft, American Institute of Aeronautics and Astronautics, Washington, D.C., 2000
[15]. N. Yamamoto, H. Katahara, H. Masui, H. Ijiri, and H. Nakashima, AJCPP2005-22093, 2005
[16]. M. Hirakawa and M. Nakakita, Simulation of Electron Cyclotron Resonance in a Microwave Discharge Ion Thruster, *Journal of Japan Society for Aeronautical and Space Sciences* .Vol.**47**, pp.267-271, 1999 (in Japanese)

[17]. T.Kanagawa, N.Yamamoto, Y. Kajimura and H. Nakashima, " Numerical Simulation of Internal Plasma in a Miniature Microwave Discharge Ion Thruster" IEPC-2007-190

[18]. N.Yamamoto, H. Kataharada, T. Chikaoka, H. Masui, and H.Nakashima,IEPC-2005-036, 2005.

[19]. H. Masui, T. Tanoue, H. Nakashima and I. Funaki, 24th International Symposium on Space Technology and Science, paper ISTS 2004-b-11, 2004.

[20]. Y. Takao, H. Masui, T. Miyamoto, H. Kataharada, H. Ijiri and H. Nakashima, *Vacuum*, Vol.73, pp.449-454 , 2004.

[21]. T. Ezaki, N. Yamamoto, T. Tsuru, Y. Kotani, H. Nakashima, N. Yamazaki, K. Tomita and K. Uchino, *Japan Society for Aeronautical and Space Sciences*, Vol.8, No 27, pp 55-59, 2010.

[22]. H. Masui, Y. Tashiro, N. Yamamoto, H. Nakashima and I. Funaki, *Japan Society for Aeronautical and Space Sciences,* Vol.49, No. 164 , pp 87-93 , 2006.

[23]. Y. Takao, H. Koizumi, K. Eriguchi, K. Komurasaki, and K. Ono, "Three-dimensional Particle in Cell Simulation of Miniature Plasma Source for a Microwave Discharge Ion Thruster" , *Plasma Source Sci. Technol,* Vol.23, pp 64004-64015 ,2012.

[24]. M. Tsuru , Performance Optimization of Miniature Microwave Discharge Neutralizer, Master's Thesis. Kyushu University, Fukuoka, Japan, 2008, (in Japanese).

[25]. M. Hirakawa, and Y. Arakawa, Plasma Particle Simulation in Cusped Ion Thrusters. 1993, IEPC-93-242.

[26]. D. M. Goebel, R. E. Wirz, and I. Katz, Analytical Ion Thruster Discharge Performance Model. AIAA paper 4486. 42nd AIAA/ASME/SAE/ASEE Joint Propulsion Conference and Exhibit, Sacramento, CA 2006.

[27]. Y. Takao, H. Koizumi, K. Komurasaki, K. Eriguchi and K. Ono, *Plasma Sources Science and Technology,* Vol **23**, No 6, pp.1-6 , 2014.

[28]. G. M. Sandonato, J. J. Barroso, and A. Montes, Magnetic Confinement Studies for Performance Enhancement of a 5-cm Ion Thruster. *IEEE Transactions on Plasma Science* 24, 6, , pp.1319–1329, 1996.

[29]. A. Yousefian, N. Yamamoto, proceedings, 62nd Space Science and Technology Conference (UKAREN), not peer reviewed, Kurume City, Fukuoka 24-26 Oct, 2018.

[30]. H. Masui , Numerical analysis of microwave discharge type plasma propulsion plasma source, Doctoral Thesis. Kyushu University, Fukuoka, Japan, 2005, (in Japanese).

[31]. K. Ushio , Study on microwave discharge type small plasma thruster, Doctoral Thesis. Kyushu University, Fukuoka, Japan, 2018, (in Japanese).

[32]. Mahalingam, S. and Menart, J., "Computational Model Tracking Primary Electrons, Secondary Electrons and Ions in the Discharge Chamber of an Ion Engine," AIAA Paper No. 2005-4253, 2005.

[33]. Mahalingam, S. and Menart, J., "Computational Study of Primary Electron Confinement by Magnetic Fields in the Discharge Chamber of an Ion Engine," Journal of Propulsion and Power, Vol. 23, pp. 69-72, 2007.

[34]. Mahalingam, S., Choi, Y., Loverich, J., Stoltz, P.H., Jonell, M., and Menart, J., "Dynamic Electric Field Calculations Using a Fully Kinetic Ion Thruster Discharge Chamber Model," AIAA Paper 2010-6944, 2010.

[35]. Stueber, T., "Ion Thruster Discharge Chamber Simulation in Three Dimensions," AIAA Paper No. 2005- 3688, 2005.

[36]. Stueber, T., "Discharge Chamber Primary Electron Modeling Activities in 3-Dimensions," AIAA Paper No. 2004-4105, 2004.

[37]. Boeuf, J.P. and Garrigues, L., "Low Frequency Oscillations in a Stationary Plasma Thruster," Journal of A pplied Physics, Vol. 84, pp. 3541-3554 , 1998.

[38]. C. K. Birdsall , Particle in Cell Charged-Particle Simulations plus Monte-Carlo collisions with Neutral Atoms, PIC-MCC, *IEEE Transactions On Plasma Science*, Vol 19 , pp 65-85 , 1991

[39]. I. D. Boyd, D. B. Vangilder, X. Liu , " Monte Carlo Simulation of Neutral Xenon Flows Of Electric Propulsion Devices" IEPC-97-020

[40]. D. Heifetz, D. Post , M. Petravic , J Weisheit and G. Bateman , A Monte-Carlo Model of Neutral-Particle Transport in Diverted Plasmas , *Journal of Computational Physics* , No 46 , pp 309-327 , 1982

[41]. D. J. Economou, T. J. Bartel, R. S. Wise, and D. P. Lymberopoulos , Two Dimensional DSMC of Reactive Neutral and Ion Flow in High Density Plasma Reactor , *IEEE Transactions On*

Plasma Science, Vol 23 , No 4 , pp 581-590 , 1995

[42]. R. K. Porteous and D. B. Graves , Modeling and Simulation of Magnetically Confined Low Pressure Plasma in two Dimensions , *IEEE Transactions On Plasma Science*, Vol 19 , pp 204-213 , 1991

[43]. C. K. Birdsall , Particle in Cell Charged-Particle Simulations plus Monte-Carlo collisions with Neutral Atoms, PIC-MCC, *IEEE Transactions On Plasma Science*, Vol 19 , pp 65-85 , 1991

[44]. Y. Sentoku , K. Mima , Y. Kishimoto , M. Honda , Effects of Relativistic Binary Collison's on PIC Simulations of Laser Plasmas , *Journal of Physical Society of Japan* , Vol 67 , No 12 , pp 4048-4088 , 1998.

[45]. T. Takizuka and H. Abe , A Binary Collision Model for Plasma Simulation with a Particle Code , *Journal of Computational Physics* , Vol 25 , pp 205-219 , 1977

[46]. H. Okuda , C. K. Birdsall and A. B. Langdon , Methods in Computational Physics, Vol 9, p 241 , Academic Press , New York , 1970

[47]. D. Y. Oh and D. E. Hastings , Computational Modeling of Expanding Plumes in Space Using a PIC-DSMC Algorithm , IEPC-97-179 , 1997

[48]. Vacuum Handbook New Edition ,ULVAC, pp 40-47 , 2002 (in Japanese).

[49]. Komurasaki, K. and Arakawa, Y., "Two-Dimensional Numerical Model of Plasma Flow in a Hall Thruster," Journal of Propulsion and Power, Vol. 11, pp. 1317-1323, 1995.

[50]. Fife, J.M., Martinez-Sanchez, M., and Szabo, J., "A Numerical Study of Low-Frequency Oscillations in Simulation of Electric Propulsion Thrusters Hall Thrusters," AIAA Paper No. 97-3052, 1997

[51]. Hagelaar, G.J.M., Bareilles, J., Garrigues, L., and Boeuf, J.P., "Two-Dimensional Model of a Stationary Plasma Thruster," Journal of A pplied Physics, Vol. 91, pp. 5592-5598 , 2002.

[52]. Garrigues, L., Hagelaar, G.J.M., Bareilles, J., Boniface, C., and Boeuf, J.P., "Model Study of the Influence of the Magnetic Field Configuration on the Performance and Lifetime of a Hall Thruster," Physics of Plasmas, Vol. 10, pp. 4886-4892, 2003.

[53]. Bareilles, J., Hagelaar, G.J.M., Garrigues, L., Boniface, C., Boeuf, J.P., and Gascon, N., "Critical Assessment of a Two-Dimensional Hybrid Hall Thruster Model: Comparisons With Experiments," Physics of Plasmas, Vol. 11, pp. 3035-3046, 2004.

[54]. Boniface, C., Hagelaar, G.J.M., Garrigues, L., Boeuf, J.P., and Prioul, A., "Modeling of Double Stage Hall Effect Thruster," IEEE Transactions on Plasma Science, Vol. 33, pp. 522-523 , 2005.

[55]. A. Yousefian, N. Yamamoto, "Neutral Density and Recycle Analysis in a Miniature Neutralizer Utilizing Particle In Cell Simulation with Respect to Inlet Configuration", Frontier of Applied Plasma Technology, peer reviewed, Vol. 13, No. 1, pp 7-12 , 2020

[56]. K. Kubota , H. Watanabe , N. Yamamoto , H. Nakashima , T. Miyasaka , I. Funaki , "Numerical Simulation of Microwave Neutralizer Including Ion's Kinetic Effects", *American Institute of Aeronautics and Astronautics* , 3831, 2014

[57]. K. Kubota , H. Watanabe , N. Yamamoto , H. Nakashima , T. Miyasaka , I. Funaki , "Three-dimensional Hybrid-PIC Analysis on Electron Extraction of a Microwave Neutralizer", *Journal Of The Japan Society For Aeronautical And Space Sciences* , Vol. 63, No. 5, pp 1997-203 , 2015

[58]. V. Vahedi, M. Surendra, "A Monte Carlo collision model for the particle-in-cell method: applications to argon and oxygen discharges", *Computer Physics Communications*, Vol 87 pp 179-198, 1995

[59]. K. Minami , "Computer Analysis Series 7 Numerical Simulation Using Atomic and Molecular Models" , *The Japan Society of Mechanical Engineers*, Corona Publishing , 1996 (in Japanese).

[60]. R. W. Hockney, and J. W. Eastwood, Computer Simulation using Particles, Taylor & Francis Group, New York, 1988.

[61]. M. Hayashi, Bibliography of Electron and Photon Cross Sections with Atoms and Molecules Published in the 20th Century - Xenon , National Institute for Fusion Science database , NIFS-DATA-079, 2003

[62]. M. Kusuda, Y. Sasagawa, N. Yamamoto and H. Nakashima, "Numerical Simulation Analysis of Microwave Discharge Neutralizer Internal Physics" Proceedings of Space Transportation Symposium-011, Institute of Space and Astronautical Science, Japan Aerospace Exploration Agency , Sagamihara, Kanagawa Japan , 2013 (in Japanese).

[63]. M. Kusuda, Y. Sasagawa, N. Yamamoto and H. Nakashima, "Two-Dimensional Numerical Analysis of a Miniature Microwave Discharge Neutralizer" , *Japan Society for Aeronautical and Space Sciences-S026*, 2011 (in Japanese).

[64]. H. Koizumi and H. Kuninaka , "Miniature Microwave Discharge Ion Thruster Driven by 1 Watt Microwave Power" *Journal of Propulsion & Power,* Vol 26, pp601-604, 2010.

[65]. H. Masui, U. Tashiro, N. Yamamoto, H. Nakashima, I. Funaki, "Analysis of Electron and Microwave Behaviour in Microwave Discharge Neutralizer" *Transactions Of The Japan Society For Aeronautical And Space Sciences, Aerospace Technology Japan* Vol 49,pp 87-93, 2005.

[66]. K. Kubota, H. Watanabe, N. Yamamoto, H. Nakashima, T. Miyasaka, I. Funkai, "Three Dimensional Hybrid-PIC Analysis on Electron Extraction of a Microwave Neutralizer" *Proceedings of the Japan Aeronautics and Space Administration* Vol 63, issue 5 , pp197-203, 2015.

[67]. M. Nakashima, *Microwave Engineering – Foundations and Principles,* Morikita Electrical Engineering Series 3, pp 67-69, 1995.

[68]. H. Kousaka, K. Ono, "Numerical Analysis of the Electromagnetic Fields in a Microwave Plasma Source Excited by Azimuthally Surface Waves" Japan Journal of Physics. Vol 41, pp 2199-2206, 2002.

[69]. K. Yee, "Numerical Solution of Initial Boundary Value Problems Involving Maxwell's Equations in Isotropic Media" *IEEE Trans,* Vol 14 , pp 802-307 ,1966.

[70]. F.Chen. Francis, in Introduction to Plasma Physics and Controlled Fusion, 2nd ed. *by Plenum Publishing Corporation,* 1974 .

[71]. K. Sugita , Microwave frequency dependence of small microwave discharge type ion thruster , Master's Thesis. Kyushu University, Fukuoka, Japan, 2011, (in Japanese).

[72]. N. Yamamoto, K. Tomita, N. Yamasaki, T. Tsuru, T. Ezaki, Y. Kotani, K. Uchino, H. Nakashima, "Measurements of electron density and temperature in a miniature microwave discharge ion thruster using laser Thomson scattering technique", *Plasma Sources Science and Technology.* Vol 19, No 4, 2010.

[73]. Y. Nakayama, K. Narisawa, "Neutral Density Measurement of Ion Thruster with Differential Pressure Gauge", *Transactions Of The Japan Society For Aeronautical And Space Sciences.* Vol 12, No 29, pp 73-78 , 2014.